ABSTRACT

Title of dissertation: MOLECULAR BASIS OF THE KINEMATICS OF THE KINESIN STEP

Zhechun Zhang, Doctor of Philosophy, 2012

Directed by: Professor Devarajan Thirumalai
Biophysics Program
Institute for Physical Science and Technology,
Department of Chemistry and Biochemistry

Kinesin is an ATP-dependent cellular transporter that ferries cargos towards the plus-end of a microtubule. Despite significant advances in experiments, which have provided deep insights into the motility of kinesin, the molecular events that occur in a single step have not been fully resolved. In order to provide these details, this thesis develops a structure of the complex between kinesin and microtubule, and devises new simulation methods to probe the stepping kinetics over a wide range of conditions. Hundreds of molecular movies of kinesin walking on the microtubule are generated using coarse-grained simulation methods. Analysis of these movies shows that there are three major stages in the stepping kinetics of kinesin. In addition, an allosteric network within kinesin, responsible for controlling nucleotide release, is identified using μs all-atom simulations. These simulations are used to answer two important questions.

First, does kinesin move by a "power stroke" or by diffusion? During a single step, the trailing head of the kinesin detaches from the microtubule, passes the

microtubule-bound leading head, and attaches to the target binding site 16 nm away. The target binding site, however, is one of eight accessible binding sites on the microtubule. Is it possible that the "power stroke" (a large conformational change) in the leading head, pulls the trailing head into the neighborhood of the target binding site? This remained unclear because the fraction of the 16 nm step associated with the power stroke and diffusion had never been quantified.

Second, how does the microtubule accelerate ADP release from kinesin, which is a key step in completing a single step? The ADP binding site of kinesin is more than 1.5 nm away from the microtubule binding surface. Therefore, the microtubule must affect the ADP binding site through an allosteric mechanism. However, the structural basis for transmitting signals through the underlying allosteric network was previously unknown.

Analysis of hundreds of kinesin steps generated using coarse-grained simulations showed that the power stroke associated with the docking of the neck linker to the leading head, is responsible for only 4 nm of the 16 nm step, and the remaining 12 nm is covered by diffusion. However, the power stroke in the leading head constrains the diffusion of the trailing head, decreases the probability of side steps, and therefore biases the trailing head, to the target binding site. Additional all-atom simulations of the ADP-kinesin-microtubule complex, revealed a surprisingly simple allosteric network within kinesin that explains the acceleration of ADP release upon microtubule binding. The allosteric network also explains two additional experimental observations on ADP release from kinesin.

MOLECULAR BASIS OF THE KINEMATICS OF THE KINESIN STEP

by

Zhechun Zhang

Dissertation submitted to the Faculty of the Graduate School of the
University of Maryland, College Park in partial fulfillment
of the requirements for the degree of
Doctor of Philosophy
2012

Advisory Committee:
Professor Devarajan Thirumalai, Chair/Advisor
Professor Michael E. Fisher
Professor David Fushman
Professor George H. Lorimer
Professor John D. Weeks

Preface

This dissertation presents two computer simulations related to the molecule kinesin, a cellular transporter that functions like a truck inside cells. The goal is to address two important questions concerning kinesin, that are extremely difficult to answer using current experimental techniques alone.

Chapter 1 is mainly a chronicle of kinesin research, both experimental and theoretical, beginning with the discovery of kinesin in 1985. The chapter ends with a few outstanding questions that inspired this dissertation.

Chapter 2 contains a preparatory analysis of the kinematics of the kinesin step. In particular, two important energy scales that determine the stepping dynamics of the kinesin, are identified.

Chapter 3 answers the first question explicitly. Does kinesin move via a power stroke or by diffusion? Also, the coarse-grained simulation method developed in Chapter 2 is improved and tested, by comparing simulation results to two independent experiments.

Chapter 4 provides an answer to the second question, using all-atom simulations. How does the microtubule accelerate ADP release from the kinesin? A surprisingly simple allosteric network is discovered. The allosteric network links the microtubule binding surface and the ADP binding pocket of the kinesin. Besides, the same allosteric network also explains the effect of strain and of mutation on ADP release from kinesin.

Chapter 5 starts with a summary of the new knowledge gained by these two simulations. The summary is followed by conclusions that apply beyond kinesin.

This chapter ends with a few thoughts on potential future directions.

Appendices A to C provide detailed simulation methods and supplemental data. Procedures for constructing a kinesin-microtubule complex containing three microtubule protofilaments, two kinesin motor heads, a coiled coil, and a cargo, are described in Appendix A. Appendix B includes (1) the coarse-grained method for simulating kinesin steps on a microtubule, and (2) supplemental figures from the coarse-grained simulations. Appendix C provides details of the all-atom simulations of the ADP-kinesin-microtubule complex.

Dedication

To My Wife and Parents

Shoot for the moon. Even if you miss, you will land among the stars ...

(Unknown)

Acknowledgements

First, I would like to thank my advisor Professor Dave Thirumalai. Here are a few things I would have learned from him, if one day I become a mentor myself. Dave granted me the freedom to follow my own curiosity and develop my own project. However, he would make sure that whatever project I developed, the end product would be of the highest quality. Therefore, he would scrutinize every detail of the project. For each manuscript, he would demand meaningful questions, proper methods, clean results and fluid presentations. Because of that, I became desperate sometimes. However in retrospect, I appreciate every piece of his advice. Dave is not only strict, but nurturing. When the projects went well, he sponsored me to the best conferences. When our manuscript got rejected, Dave claimed the responsibility and took the blame. If I spent little less time on research, even just for a week, he would immediately sense it and urge me to "start working again". In short, I feel very fortunate to work with Dave.

I am also very thankful to other members of my thesis committee. Professor Lorimer offered me a research assistantship six years ago, which got me into the biophysics PhD program. Later on, after I switched to a different group, he still followed my academic progress, invited me to his house for dinner, gave me tickets to concerts, and wrote recommendation letters for me. Professor Fisher, being the most senior faculty in the program and perhaps in the university, is extremely friendly to young graduate students. I had many fun conversations with him and also received much helpful advice, as his teaching assistant and a newcomer to molecular motors. I will always remember that Professor Fisher once started the conversation with: "If

you were my son, I would...". Last, I want to thank Professor Weeks and Professor Fushman, for squeezing a precious afternoon from their busy schedules, to attend my defense and comment on my thesis.

I am grateful to my scientific colleagues. First and foremost, previous and current members of the Dave's group (Shaon Chakraborty, Jie Chen, Margaret S. Cheung, Samuel Cho, Natasha Denesyuk, Ruxandra Dima, Michael Hinczewski, Changbong Hyeon, Hongsuk Kang, Alex Kudlay, Jong-Chin Lin, Zhenxing Liu, Greg Morrison, Toan M. Ngo, Edward O'Brien, David L. Pincus, Govardhan Reddy, Himadri Samanta, Biyun Shi, Riina Tehver, Subramanian Vaitheeswaran, Wenjun Zheng, and Pavel Zhuravlev). I will remember them not only as scientists who taught me basic techniques, helped me sharpen my arguments, and commented on my practice talks. But friends who went to weekly group lunch, had heated debates, played volleyball games, and shared the ride along the scenic California Route 1 with me. Second, I want to thank many researchers in the field of molecular motors, who I talked to at conferences or seminars (Steve Block, Andrew Carter, Robert Cross, Yale Goldman, Susan Gilbert, David Hackney, Jonathon Howard, Kazuhiro Oiwa, Sarah Rice, Matthias Rief, Steven Rosenfeld, Charles Sindelar, James Spudich, Toshio Yanagida, and Ahmet Yildiz). It was their collective work, that attracted me into this vibrant field and kept me motivated during the course of my PhD. Their encouragement and criticisms helped me improve existing projects and design new projects. Last, I also want to thank the PNAS reviewers who rejected my first paper. I suffered. But I also learned a lot. The rejection made me a sharper scientist and a more mature person.

Certainly I would not be able to complete this thesis, without the love and support from my wife Xue Fei and my parents. Xue has been an inspiration for me, since I first met her in high school. In the past eleven years, her love and care were always present, as I went through surgeries, applied for graduate school, submitted and resubmitted papers, and prepared for interviews. As a structural biologist herself, she also helped me revise many of my talks. I must also thank my parents, whom both sacrificed a lot to nurture me from a newborn to a young man. Even today, ten years after I left their nest for college, they would still support me by all means and be concerned about me as if I were a ten-years-old.

During my PhD study, I was supported by grants from National Science Foundation (CHE09-14033) and Pittsburgh Supercomputing Center (PSCA10030P), and the Ann G. Wylie Fellowship from the University of Maryland.

At the end, for everything mentioned here, I give thanks to God.

Table of Contents

List of Figures

List of Abbreviations

α	alpha
β	beta
ADP	Adenosine diphosphate
AMPPNP	Adenylyl-imidodiphosphate
APO	no nucleotide
ATP	Adenosine triphosphate
CG	coarse-grained
FIONA	fluorescence imaging at one-nanometer accuracy
GDP	guanosine diphosphate
GEF	guanine exchange factor
HI	hydrodynamic interactions
IBS	initial binding site
LH	leading head
MT	microtubule
NL	neck linker
RMSD	root mean square deviation
SBS	side binding site
TBS	target binding site
TH	trailing head

Chapter 1

Introduction

1.1 Overview

How do muscles in our body contract and generate force? How do organisms containing only a single cell move towards nutrients or other targets? How do nerve cells in our brain transport signaling molecules from the cell body to the nerve terminal $\sim$ 1 meter away? Studies of these interesting phenomena involving the generation of force and movement, led to the discovery of a class of molecular motors including myosin, dynein, and kinesin.

Some of the early theories of muscle contraction can be dated back to the time of Aristotle, who proposed that the movements of animals are caused by something like puppet strings [1]. Our current understanding of muscle contraction is in part due to imaging of muscle tissue using electron microscopy [2]. It was revealed in the 1960s that a large number of myosin molecules crosslink and slide different filaments in the muscle, and thereby cause contraction. Later studies showed that myosin can also transport cellular cargos such as membrane-bound organelles along actin filaments within the cells [3, 4]. Thus, these studies on myosin demonstrated how forces and movements observed at the macroscopic scale are generated by microscopic motors.

Another such microscopic motor discovered in the 1960s is dynein [5], which

plays a critical role in the motility of sperm and single-cell organisms. Dynein generates a beating pattern in the axoneme [6, 7]-a key component of the tail of sperm, and allows sperm to swim toward the egg for fertilization. Dynein was first purified in 1965 from the axoneme of the cilia of the single-cell organism, *Tetrahymena pyriformis* [5]. Besides generating beating motion in the axoneme, dynein was later found to be a microtubule-based cellular transporter [8]. However, dynein is not the only cellular transporter that moves on microtubules.

1.2 Discovery of kinesin: A brief history

The cellular transporter kinesin was discovered in 1985, after a series of studies [9–11] aiming to understand the molecular basis of fast organelle transport along the axon. Organelles, containing for example neuronal signaling molecules, are transported by more than a meter in some animals, between the cell body of a neuron and its nerve terminal [12]. The speed of fast organelles transport can be up to several microns per second in mammals [13].

Four important findings paved the way for the landmark paper [14] in August 1985, which not only reported the purification protocol and the molecular weight of the cellular transporter, but gave it the name kinesin. The first finding is that organelles are transported along microtubule filaments [9]. Other types of filaments, such as actin filaments, were ruled out using video-enhanced optical microscopy, *Cryo*-electron microscopy, and immunofluorescence [9]. Second, organelle transport requires ATP, indicating that the corresponding transporter hydrolyzes ATP to

move to the cargo along microtubules [11]. Third, different organelles move at the same speed, suggesting that a single type of transporter is involved in fast organelle transport [10]. Finally, the transporter binds stably to the microtubule in the presence of AMPPNP (adenylyl imidodiphosphate, a nonhydrolyzable ATP analog) [15]. This finding ruled out dynein, the only other known microtubule-based transporter at that time, as a potential candidate, because dynein detaches from microtubule upon AMPPNP binding.

In the paper published in August 1985 [14], Vale *et.al.* purified the mysterious cellular transporter from giant squid, measured its molecular weight, compared it to known transporters, and proposed a new name: "kinesin". They purified the kinesin by first co-sedimenting the transporter with the microtubule, based on its high affinity with the microtubule in the presence of AMPPNP. Second, by adding ATP, kinesin is released and then detached from the microtubule. Next, the authors measured the molecular weight using gel filtration columns. It was found that kinesin has an apparent molecular weight of 600 kilodaltons and contains 110-120 and 60-70 kilodalton polypeptides. Both the unique molecular weight and the unusually strong affinity to the microtubule in the presence of AMPPNP, suggest that kinesin is a novel class of molecules, distinct from myosin and dynein.

Almost simultaneously (September 5th 1985), Brady reported the discovery of kinesin in a different species [16]. While Vale *et.al.* purified kinesin from squid and bovine, Brady extracted kinesin from the brains of 2-7-day-old chicks. Interestingly, Brady wrote at the end of his letter [16] that (quoting): "During the preparation of this manuscript, I learned that, based on our earlier work with AMP-PNP, Vale

et.al. have used AMP-PNP to enrich for a similar sized protein from a soluble fraction of squid optic lobe that promotes motility in their assay". This is a fair statement, as Vale *et.al.* wrote in the abstract of their paper (August 1985) [14] that "the purification of the translocator protein depends primarily on its unusual property of forming a high affinity complex with microtubules in the presence of nonhydrolyzable ATP analog, adenylyl imidodiphosphate". Therefore, although Vale and Sheetz are usually credited with the discovery of kinesin, it is likely that other people such as Brady also played a critical role in the discovery of the usual transporter.

On December 5th 1985, kinesin was purified from a third species: sea urchin [17]. Unlike previous studies which looked at the role of kinesin in fast organelle transport, the study by Mcintosh and colleagues focused on the role of kinesin in cell division. Besides purifying the protein and measuring its molecular weight, the authors also examined the spatial distribution of kinesin in dividing sea urchin embryos. It was found that during cell division kinesin colocalizes with spindle fibers, which pulls sister chromatids towards the opposite ends of the cell. This result suggested that kinesin participates in force generation during cell division.

1.3 Important experimental findings on kinesin since 1985

The discovery of kinesin in 1985 attracted a wave of excellent biochemists, biophysicists, and structural biologists into the field. In the following twenty years, these scientists collectively generated a significant amount of knowledge about ki-

nesin, such as the mechanochemical cycle, the speed and force, and the crystal structure. Interestingly, the kinesin community also witnessed the first applications of many ground-breaking single molecule techniques, such as the optical tweezer and the FIONA (fluorescence imaging at one-nanometer accuracy), to probe biological systems. Here eleven studies will be described to highlight some of the interesting features of kinesin, and to emphasize the diversity of experimental techniques used to study this motor.

1.3.1 November 1986: Measuring the ATPase activity of kinesin

It was known that ATP is required for kinesin to transport organelles along microtubules. However, it was unclear the rate at which kinesin consumed ATP, what was the rate-determining process during the ATP turnover cycle, and how did the rate of ATP turnover depend on the microtubule. Kuznetsov, Gelfand, and Hackney [18,19] determined that microtubules increase the rate of ATP turnover by kinesin from ~ 0.009 sec^{-1} mol^{-1} ([ATP]/[Kinesin] = 7.4) to 9 sec^{-1} mol^{-1}([ATP] = 8.3 μM, [microtubule] = 8.3 μM). Also, in the absence of microtubules the rate-determining process in ATP turnover is ADP release, which can be accelerated by several orders of magnitude upon addition of microtubules [19]. These results collectively revealed the important role of microtubules in the function of kinesin, and showed that they are not merely passive polar tracks.

1.3.2 March 1989: Electron micrographs of kinesin

In early 1989, two independent groups reported the first electron microscopy images of kinesin [20,21]. These images showed that kinesin consists of two globular heads attached to a fibrous stalk, which terminates in a feathered or fan-shaped tail (Fig. 1.1). In addition, by using monoclonal antibodies it was shown that these two globular heads belonged to two chains of kinesin arranged in parallel. The globular head located at the N-terminal of the chain, exhibits nucleotide-dependent interactions with the microtubule. The tail at the C-terminal end of the chain, in contrast, interacts with organelles. Thus, besides the overall structure of kinesin, the mechanochemical head and the cargo binding site of kinesin were identified for the first time in these electron micrographs.

1.3.3 November 1990: Tracking the motion of a single kinesin

Two back-to-back letters tracking single kinesin motions *in vivo* and *in vitro*, appeared in the same issue of Nature in 1990. In the first study [22], Ashkin *et al.* tracked the motion of mitochondria transported by kinesin, in a living giant amoeba, using optical tweezers. In the second letter [23], Block *et al.* also used optical tweezers; but they traced the microscopic silica beads attached to kinesin in an *in vitro* system. While Ashkin *et al.* performed a proof-of-principal experiment using optical tweezer to probe *in vivo* systems, Block went a step further to measure the processivity of kinesin. The processivity is the run length a single kinesin motor covers on the microtubule before it detaches from the track. It was found that a sin-

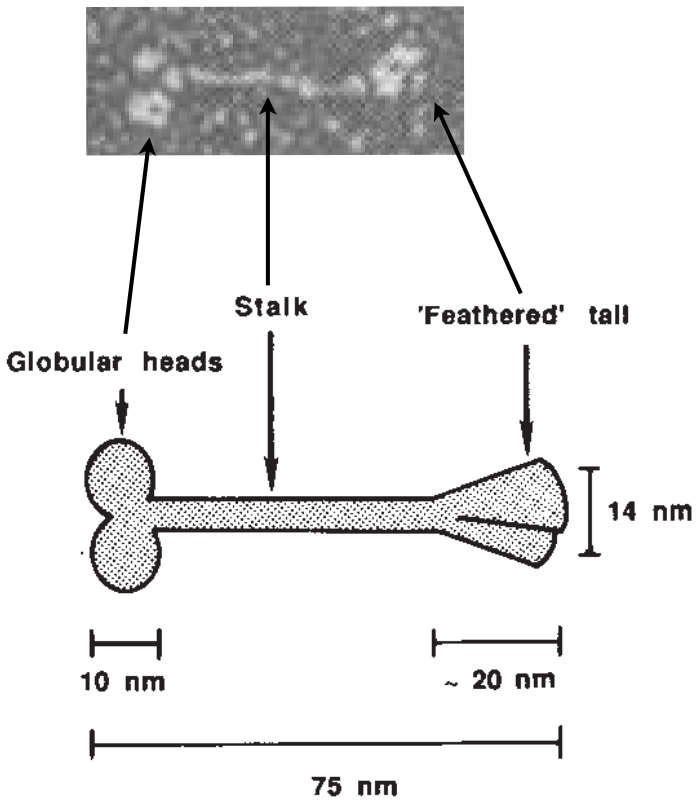

Figure 1.1: An electron micrograph of kinesin

The upper (lower) panel shows an electron micrograph (a cartoon presentation) of kinesin (adapted from [20]).

gle kinesin can move processively for 1-2 μm before detaching from the microtubule. These two studies marked the beginning of studying kinesin using single-molecule optical tweezer techniques.

1.3.4 June 1993: Kinesin follows the microtubules protofilament axis

It was known at that time that kinesin moves on the microtubule, but whether kinesin moves parallel to the microtubules protofilament axis remained unclear. Given that a microtubule contains multiple (usually 13) protofilaments (Fig. 1.2a), it is possible that kinesin could move sideways from one protofilament to another. The Howard group at the University of Washington, tested this hypothesis using a microtubule gliding assay [24]. If kinesin follows the microtubules protofilament axis, microtubules that contain 13 protofilaments, would not rotate with its long axis as it glides across a kinesin-coated surface. This is because each of the 13 protofilament follows a straight line, and does not twist (Fig. 1.2b). Indeed, no rotation was observed in the gliding assay for microtubules containing 13 protofilaments. In general, the rotational pitches of microtubule in the gliding assay matched the supertwist pitches of protofilaments of the microtubule, indicating that kinesin follows the microtubules protofilament axis (Fig. 1.2b).

1.3.5 October 1993: Discrete 8-nm steps of kinesin

Another question concerning the movement of kinesin on a microtubule is whether kinesin takes regular steps, and if so what is the step size. The Block group

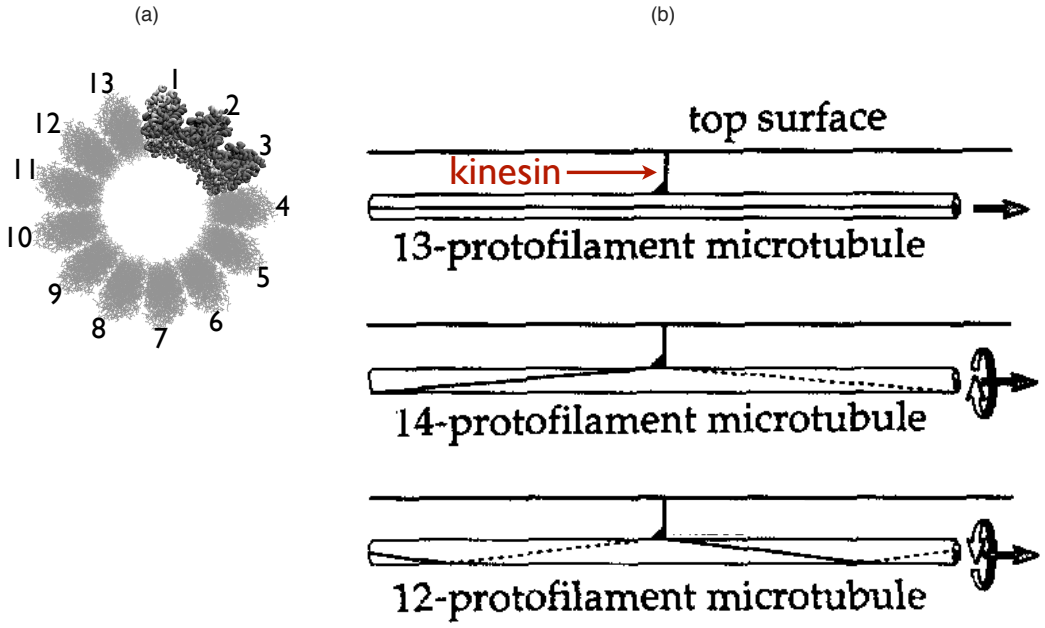

Figure 1.2: Kinesin follows the microtubule's protofilament axis

(a) A sectional view of a microtubule containing 13 protofilaments (the structural model of the microtubule is provided by the Downing lab from the Lawrence Berkeley national laboratory). (b) The experimental set up of the microtubule gliding assay (adapted from [24]). One end (the cargo binding domain) of kinesin is attached to the (top) surface, and the other end (the motor heads) of kinesin walks on the microtubule. The protofilament axis, which kinesin follows, is indicated for the 13-protofilament, 14-protofilament, and 12-protofilament microtubule.

used optical tweezers with sufficient spatial and temporal resolution (Fig. 1.3) to answer this crucial question [25]. They found that kinesin moves with close to 8-nm steps (8.2 nm). This step size is consistent with the distance between adjacent α/β-tubulins (the elemental component of microtubules) along a single protofilament. Thus, kinesin takes hundreds of steps along the microtubule before detaching, which established that it is a highly processive motor.

1.3.6 June 1994: Force and velocity of kinesin

After determining the step size of kinesin, the Block group measured the force and velocity of kinesin using optical tweezers [27]. It was found that at saturating ATP concentration (2 mM ATP) kinesin moves at $\sim$ 800 nm/sec under no external force. The velocity decreases linearly with resistive force, and kinesin stalls at an external force of $\sim$ (6-7) pN.

1.3.7 July 1994: The two heads of kinesin are coordinated

It was established in 1989 that kinesin contains two globular mechanochemical motor heads, which bind to the microtubule and hydrolyze ATP. However, does kinesin coordinate the chemical state of its two motor heads while walking on the microtubule? Hackney provided the first piece of experimental evidence supporting that hypothesis [28]. He found that when kinesin binds to the microtubule, only one motor head releases the bound ADP. The second head cannot release ADP, until the first head accepts a new ATP molecule. This result suggested that kinesin does

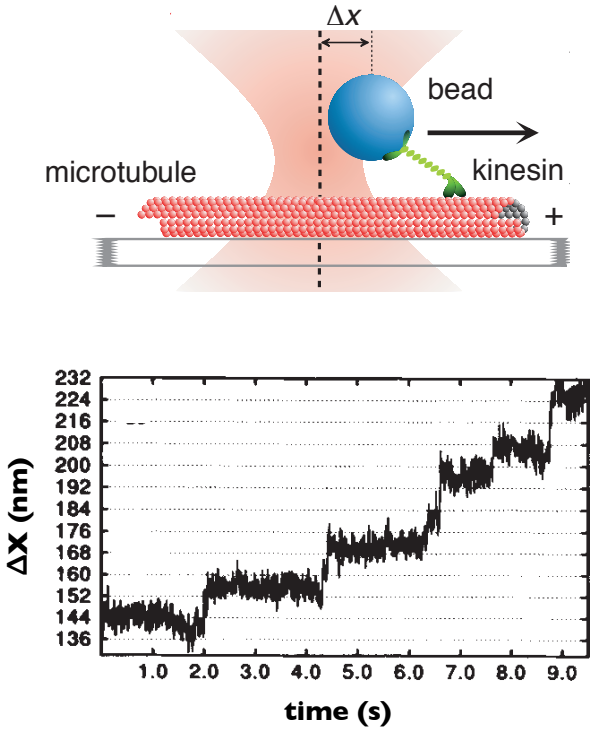

Figure 1.3: Tracking the motion of kinesin with an optical tweezer

The upper panel shows a typical set up of an optical tweezer experiment (adapted from "Visscher, Block, and coworkers" [26]). The low panel is an actual record of the movement of the bead (in blue in the upper panel) attached to a kinesin motor (adapted from "Svoboda, Block, and coworkers" [25]).

coordinate the chemical state of the two motor heads, to keep the ATP turnover cycle of the two heads out-of-phase.

1.3.8 April 1996: Crystal structure of kinesin

Although the electron micrographs published in 1989 revealed the overall structure of the entire kinesin molecule at $\sim$ 5 nm resolution, the detailed structure of the mechanochemical motor head at atomic resolution remained unknown. Such a high resolution structure of the motor head is critical for our understanding of, for example, the coupling between ATP hydrolysis and 8 nm step. In early 1996, the Vale group reported the first crystal structure of kinesin's motor domain at 1.8 A resolution (Fig. 1.4) [29]. This structure showed an ATP binding pocket composed of a P-loop, switch-I and switch-II (labeled in Fig. 1.4), similar to other molecular motors such as myosin. The authors also proposed that the neck region is likely to be responsible for force generation in kinesin, based on structural and sequence comparison between kinesin and myosin.

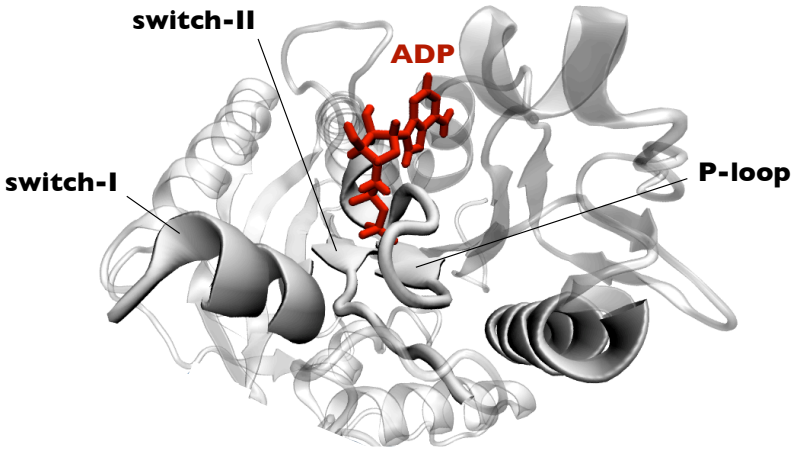

Figure 1.4: A crystal structure of the kinesin motor head

A crystal structure of the kinesin motor head in cartoon representation (Protein Data Bank ID: 1MKJ).

1.3.9 February 1999: Kinesin with a single head can move processively

In 1999, the consensus was that the processive movement of kinesin requires two mechanochemical motor heads. One head stays bound to the microtubule, while the other head takes the step. Therefore, it was surprising that Okada and Hirokawa reported that single-headed kinesin can also walk processively [30]. Kif1a, the single-headed kinesin investigated in [30], is somewhat different from the conventional kinesin identified in 1985 in terms of amino acid sequence. Moreover, the movement of Kif1a is more stochastic than the step-wise movement of conventional kinesin; further, the average speed of Kif1a is $\sim$ 140 nm/s compared with $\sim$ 800 nm/s of conventional kinesin. Nevertheless, the observation that the single-headed Kif1a can move processively for more than 1 μm was surprising, and supported a biased Brownian ratchet hypothesis [31, 32] for Kif1a motility.

1.3.10 December 1999: Large conformational change in the neck linker region: the "power stroke" of kinesin

Besides the Brownian ratchet hypothesis, the power stroke hypothesis [2, 33, 34], well understood in the context of myosin, was also a candidate that could explain the directional movement of kinesin along the microtubule. According to the power stroke hypothesis, a large conformational change in the neck linker of the microtubule-bound leading head pulls the mobile trailing head forward to complete a step (Fig. 1.5). Although the power stroke in other molecular motors such as myosin

had been observed in experiment and associated with conformational changes within lever arms [2,33,34], the structural origin of the power stroke in kinesin was unclear. In late 1999, the Vale group used several lines of plausible evidence to argue for the existence of a power stroke in kinesin [35], involving the neck linker region between the motor head and the fibrous stalk (made of intertwining coils).

It was argued, first in the paper [35] in 1999, and subsequently in a series of studies [37–42] that prior to ATP binding, the neck linker (NL) is disordered and does not interact with the rest of the motor head. Upon ATP binding, however, the NL docks to the mechanochemical head and becomes ordered. To support this, the authors provided evidence collected using several different experimental techniques, such as Foster resonance energy transfer (FRET), and *Cryo*-electron microscopy. For example, they estimated the distance between the neck linker and the motor head under AMPPNP or a no-nucleotide condition, by measuring the FRET efficiency between a dye attached to the neck linker and another dye to the motor head. It was found that the distance between the two dyes decreases by 1 nm upon adding AMPPNP. This result indicates that neck linker docks to the motor head upon ATP binding.

In addition, they also attached gold nano-particles to the neck linker of the motor heads, which were fixed to the microtubule [35]. They observed the distribution of the nano-particle under different nucleotide conditions using *Cryo*-electron microscopy. Under nucleotide-free conditions, there are several peaks in the distribution, indicating that the neck linker is disordered and can adopt multiple conformations. In the presence of AMPPNP, however, only a single peak was observed in

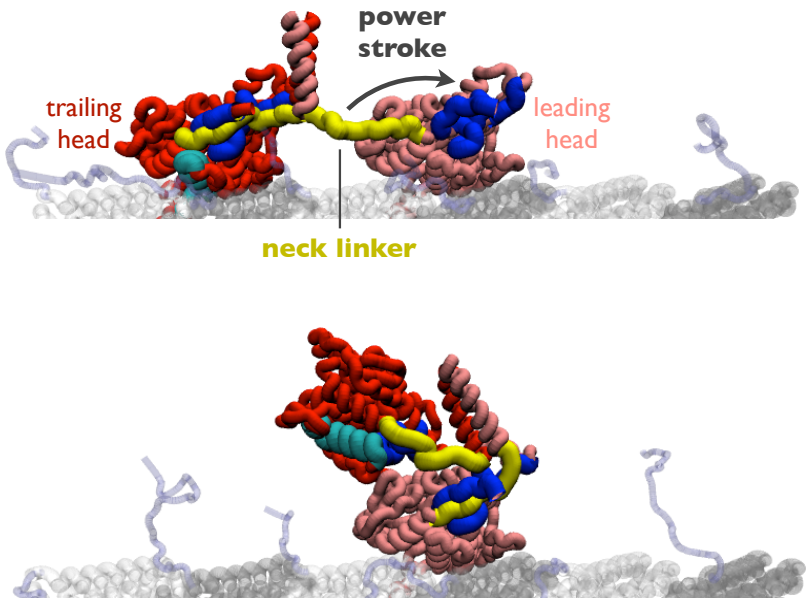

Figure 1.5: Large conformational change or "power stroke" in the neck linker of the microtubule-bound leading head

The upper (lower) panel shows the conformation of kinesin before (after) the power stroke (adapted from [36]).

the distribution of the gold particle attached to the neck linker, corresponding to an ordered neck linker docked to the motor head. Therefore, several experimental observations showed that there exists an ATP-induced large conformational change (which we will term the "power stroke") in the neck linker region of the kinesin.

1.3.11 January 2004: Kinesin walks hand-over-hand

No matter what fraction of the kinesin step is associated with the "power stroke" or with Brownian motion, respectively, a key question in 2004 was whether kinesin moves in a hand-over-hand or inchworm manner (Fig. 1.6). If the hand-over-hand model is correct, during a single step, the trailing head would detach from the initial binding site on the microtubule, pass the microtubule-bound leading head, and bind to the target binding site in front of the leading head. The head would travel $\sim$ 16 nm, from the initial to the target binding site, during each step. On the other hand, if the inchworm model is correct, the leading head would detach from the microtubule and take an 8 nm step forward; then the trailing head would take another 8 nm step to the binding site initially occupied by the leading head. However, before 2004 it was experimentally difficult to track the motion of each motor head at nanometer accuracy, which would be needed to distinguish between the hand-over-hand and inch-worm model.

Selvin and his group developed a technique, Fluorescence Imaging at One-Nanometer Accuracy (FIONA), that is capable of tracking the position of a single dye with nanometer accuracy and subsecond resolution [43]. When they attached

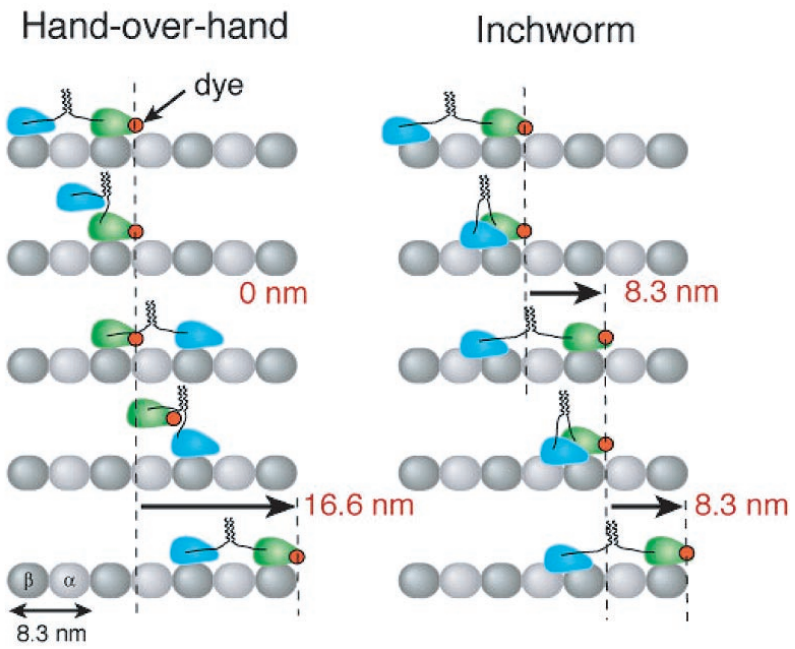

Figure 1.6: The hand-over-hand and Inchworm model

The two motor heads of the kinesin are colored in blue and green. The α- and β-tubulin of the microtubule are colored in grey and white (adapted from Yildiz *et al.* [43]).

the dye to the motor head of kinesin, they found that the motor head moves $\sim$ 16 nm during a single kinesin step, in a manner that is only consistent with the hand-over-hand model.

1.4 Key theoretical models of molecular motors

Single-molecule experiments led to the characterization of interesting biophysical properties of molecular motors, in particular the force-velocity relation [27]. These properties inspired a large number of theoretical works [31, 32, 44–61], which included specific models for kinesin [45, 47, 48, 53, 57], myosin [46, 48, 60] or RNA polymerase [54], and general models for molecular motors [44, 52, 55, 56, 58, 59, 61]. Indeed, several key concepts in quantifying the motility of motors and more general issues related to the role of mechanical forces in biology are documented in a pioneering monograph by Howard [51]. In what follows we present a discussion of five representative but distinct examples of theoretical models for molecular motors that are related to our study.

1.4.1 June 1993: A unified model of myosin, kinesin and dynein

Myosin, kinesin, and dynein are ATP-dependent motor proteins that move on actin and microtubule tracks, with different speeds, and have different biochemical rates. Leibler and Huse proposed a unified model [52] of the mechanochemical cycles of these three motor proteins. In the model, the motor protein goes through one detached state (detached from the corresponding track) and three attached states

in sequence. ATP binding, ATP hydrolysis, phosphate release, and ADP release cause transitions between those four states (one detached, and three attached). Based on the model, the authors derived the motor speed as functions of the ATP concentration. Because the model was also applicable to systems containing multiple motor proteins, a prediction for the relation between the speed of transport and the number of motor proteins was also obtained. More importantly, Leibler and Huse sorted motor proteins into "porters" (such as processive kinesins or cytoplasmic dyneins) and "rowers" (such as myosins or flagellar dyneins), based on the fraction of the time the motor stays bound to the track.

One impressive feature of the paper, besides the interesting results highlighted above, is that the authors stated clearly the limitations of the model. "It is important to stress that our model does not, and cannot, give any definite predictions concerning detailed structural issues". At the end of the paper, Leibler and Huse also made a suggestion for experimentalists who hope to "detect the step" of motor proteins: "the connection between the motor and the bead whose position is being measured should be as rigid as possible".

1.4.2 April 1995: A specific model for the dimeric kinesin

Oster *et al.* took a completely different approach (different from Leibler's), and developed a specific model for kinesin [53]. This was the first model, in which the two motor heads of kinesin was treated independently. In this model, each motor head could be in the W (weakly associated with the microtubule) or the S (strongly

associated with the microtubule) state. In the process of walking on the microtubule, the dimeric kinesin would repeatedly go through three states in sequence: SS (both heads strongly associated with the microtubule), WS (one head detaches from the microtubule), SW (the detached head moves forward and passes the microtubule-bound head), and SS (a step is complete). Using this specific model, Oster *et al.* were able to fit the force-velocity curve to experiments.

Although the model represented bold ideas, the large number of free parameters used to fit the experiments resulted in some criticism. Indeed, the transcript of the conference discussion section on this model was also published in same issue of the Biophysics Journal [53]. Leibler was concerned about the number of free parameters in the model. In contrast, Hackney, as a leading kinesin biochemist, stated "I like (the) model very much", possibly because of the explicit modeling of both kinesin motor heads.

1.4.3 May 1997: General theory of Brownian motors

Given that thermal noise is unavoidable at nanometer length scales, it is possible that molecular motors, such as kinesin, simply move via Brownian motion. Two articles published in 1997 [31, 32] laid the foundation for a general theory of how Brownian motion could be harnessed to produce directed motion. A more comprehensive review of the theory of Brownian motors was published later [50]. The following paragraphs highlight the article by Astumian [31], which offered perhaps the simplest explanation of the mechanism of Brownian motors.

First, Astumian provided a few examples of directional transport originating from coupling Brownian motion to time-dependent electrical fields or chemical reactions. Following these case studies, it was argued by the author that the Fokker-Planck (FP) equation provides a mathematical framework to study fluctuation-driven transport in general. Assume that at $t = 0$, a particle is at x_0. The probability $P(x,t)$ of finding the particle at location x at time t can be described by the FP equation

$$\frac{\partial P(x,t)}{\partial t} = -\frac{\partial}{\partial x}[\frac{U(x,t)}{\gamma}P(x,t)] + D\frac{\partial^2 P(x,t)}{\partial x^2} \tag{1.1}$$

where $U(x,t)$ is the time dependent potential, γ is the friction coefficient, and D is the diffusion coefficient.

Although the objective of his paper was to discuss the general operating mechanism of Brownian motors, Austumian touched on the mechanism of specific molecular motors. "It is not yet clear whether molecular motors such as muscle myosin or kinesin move by using an ATP-driven power stroke", "or whether energy from hydrolysis of ATP is used to bias thermally activated steps". "This question may be resolved soon with the use of recently developed techniques for studying molecular motors at the level of a single molecule".

1.4.4 March 1999: Discrete chemical kinetic models for molecular motors

Characterization of physical properties of kinesin (such as the force-velocity relation) by single molecule experiments [27, 62–64], stimulated theorists to develop

quantitative models to understand these properties. At the time, a continuum model, Eq.1.1, of Brownian motors already existed [31]. The continuum model brought up the concept that molecular motors such as kinesin can move by a biased Brownian ratchet mechanism. However, direct quantitative comparison between the model and experiments is mathematically challenging if not impossible [49], due to the unknown potentials, such as $U(x,t)$, and partial differential terms in the continuum model, Eq.1.1. Therefore, Fisher and his coworkers developed an alternative model [44–49] that is based on venerable chemical kinetics. Most importantly in these models the complexity of the reaction cycle can be explicitly taken into account.

In the discrete kinetic model developed by Fisher *et al.*, kinesin moves between different chemical states (such as the ATP-bound state, and the ADP-bound state) in the enzymatic (ATPase) cycle. As a result, the detailed motion of kinesin as it moved along the multi-protofilament microtubule, was simplified and described by rates of chemical reactions [44]. In the model, reaction rates depend on the external force and concentrations (of ATP, ADP, *etc*). Because of the discrete nature of the kinetic model, the nonlinear time-dependent second-order partial differential equation, Eq.1.1, was replaced by analytically solvable linear equations. Using the discrete kinetic model, Fisher *et al.* obtained analytic expressions for many important properties of molecular motors, such as the force [47,48], the speed [47,48], the processivity [45], and dwell time [46]. Successful fit of these quantities to experiments, provided insights into the mechanochemical coupling of kinesin. For example, the authors were able to identify the reactions within the ATPase cycle that are most

sensitive to external force [47, 48], and the physical displacement associated with each reaction [47, 48].

One of the novelties of the discrete kinetic model of kinesin developed by Fisher *et al.*, compared with other kinetic models, is that the model was generalized to two-dimensions [47]. Instead of assuming that each chemical reaction in the ATPase cycle is coupled to a one-dimensional physical displacement along the microtubule axis, Fisher *et al.* took into the account the possibility that kinesin also moves along a second axis during the ATPase cycle. The second axis implemented in the kinetic model of kinesin [47], is not the lateral axis, pointing from one microtubule protofilament to the other; it is the axis perpendicular to the microtubule surface, or the z-axis as so referred to by the authors [47]. Inclusion of the z-axis allowed Fisher *et al.* to predict that ATP binding causes kinesin to "crouch" prior to its major step. The structural origin of such "crouch" motion, was later revealed by the coarse-grained simulation developed in this thesis. The importance of the motion of kinesin along the z-axis, is supported by a recent single-molecule experiment [65]. This experiment showed that external force along the z-axis affected the stepping behavior of kinesin, in particular, the difference between odd and even steps (called "limping" [65, 66]).

1.4.5 November 2005: The first model for multiple motors

Lipowsky *et al.* pushed theoretical modeling of molecular motors in a new dimension, by proposing a model of how multiple motors transport a single cargo

[61]. By assuming that each motor operates independently, Klumpp and Lipowsky predicted that the run length would increase dramatically as the number of motors increases. Although later Gross *et al.* showed that the run length of cellular cargos in *Drosophila* embryos is not controlled by the number of motors [67], the authors did state that the lack of dependence is likely due to cellular regulators of the run length that are absent *in vitro*.

1.5 Outstanding questions and structural-based models

These theoretical studies provided a basis for understanding the global aspects of kinesin motility, such as the force-velocity relation. However, fundamental and vexing questions remain unanswered [68]. Here we highlight four major questions regarding the motility of kinesin, that are not yet answered and that are most interesting to address.

First, does kinesin move by a power stroke (as identified above in sec.1.3.10) or by diffusion of the detached motor head? A related issue is what is the fraction of the 16 nm step associated with a power stroke and with diffusion?

Second, how does kinesin stay on a single protofilament of the microtubule, given that a microtubule contains 13 protofilaments?

Third, how do the two motor heads coordinate with one another in order to stay out-of-phase in their nucleotide states? Coordination of nucleotide state is important, because the entire molecule will detach from the microtubule once ADP is bound to both motor heads. Recent experiments [69,70] show that intramolecular

strain between the two motor heads plays an important role in coordinating the nucleotide state. Particularly interesting from a structural perspective is how strain coordinates the nucleotide states of the motor heads.

Fourth, how does single headed kinesin Kif1a [30] move processively on microtubules? Here "processive" means that a motor runs many steps, with displacements of, say, $\sim$1 μm without detaching from the microtubule.

Most current theoretical models rest on the assumption that the microtubule track contains only one protofilament. As a consequence, it is not clear from these models how kinesin stays on a single microtubule protofilament.

Moreover, as Leibler emphasized "the model discussed here does not make microscopic or structural predictions" [52]. Thus, what is also lacking is the connection between the stepping kinetics of kinesin and the associated structures. In particular, the consequence of conformational change in the neck linker during a single kinesin step remains unclear. Besides this, the conformational change of kinesin induced by microtubule binding is not known.

The major thrust of the work presented in this thesis is to provide the much needed structural basis for understanding the stepping process, and to answer a few of these outstanding questions [68]. Most importantly our work, for the first time, shows that the microtubule plays a major active role in facilitating the stepping kinetics in kinesin.

1.6 Goals accomplished in this thesis

This thesis answers the first two questions listed above, using simulations of a coarse-grained model of kinesin (Chapters 2 and 3). In order to perform these simulations a model for the kinesin-MT complex is constructed, because even a low resolution structure does not exist. In addition, a partial answer to the third question will be given based on long-timescale all-atom molecular dynamics simulations (Chapter 4). Each chapter can be read separately.

In Chapter 2, two important energy scales involved in a single kinesin step are identified. This will be followed by a discussion on the constraints on these two energy scales, in order for kinesin to minimize the probability of taking side steps so that it can predominately stay on a single protofilament. Chapter 2 ends by pointing out that a single kinesin step occurs in three stages, the last of which depends on specific kinesin-microtubule interactions.

Chapter 3 starts with the quantification of the fraction of the 16 nm kinesin step associated with the power stroke and with diffusion. Then a possible mechanism adopted by kinesin to avoid side steps and stay on a single protofilament will be revealed. It is found that a large fraction, $\sim$12 nm, of the kinesin step is associated with diffusive motion of the detached head. Although the power stroke is responsible for only 4 nm out of the 16 nm, it constrains the conformational space that kinesin head can explore in a diffusive process. More importantly, the power stroke leads to a decrease in the probability that kinesin takes side steps.

In Chapter 4 long-timescale all-atom simulations are used to study the role of

the microtubule, of mutation, and of strain in regulating ADP release from kinesin. Results from five sets of simulations under different conditions of the microtubule, of mutation, and of strain, are correlated qualitatively with five previously reported experiments [18, 19, 69–71]. Based on these simulations, a simple structural model is proposed to explain the simulation results and earlier experiments. This work provides the first allosteric mechanism for microtubule-kinesin interaction.

Chapter 2

Dissecting the kinematics of the kinesin step

2.1 Summary

Kinesin walks processively on microtubules in an asymmetric hand-over-hand manner with each step spanning 16 nm. We used molecular simulations of a novel model of microtubule-kinesin complex to determine the fraction of a single step due to conformational changes in the neck linker, and that due to diffusion of the tethered head. Stepping is determined largely by two energy scales, one favoring neck linker docking and the other, ϵ_h^{MT-TH}, between the trailing head (TH) and the microtubule. Neck linker docking and an optimal value of ϵ_h^{MT-TH} are needed to minimize the probability that the TH takes side steps. There are three major stages in the kinematics of a step. In the first, the neck linker docks, resulting in $\sim$ (5-6) nm movements of the trailing head. The TH moves an additional (6-8) nm in stage II by anisotropic translational diffusion. In the third stage, spanning $\sim$ (3-4) nm, the step is complete with the TH binding to the $\alpha\beta$-tubulin binding site. The results summarized in this chapter are published [36].

2.2 Introduction

Molecular motors, such as myosin, kinesin, and dynein, which are involved in a number of cellular processes, walk along polar tracks ferrying cargo. Among the smallest motors is kinesin-1 (referred to as kinesin from here on), which is a cellular transporter that carries membrane organelles, mRNAs, and protein complexes along microtubules (MTs) [68, 72, 73]. Kinesin contains two identical motor heads and takes hundreds of steps by walking in an asymmetric hand-over-hand manner [35,43,66,74] on MTs before it detaches. In each step spanning ~ 8.1 nm, the distance between two successive $\alpha\beta$-tubulin sites, kinesin goes through an ATP-driven reaction cycle (Fig. 2.1a) that results in the alteration of the nucleotide-dependent interactions between the MT and the motor head. The processive hand-over-hand motion of the motor heads leads to cargo movement predominantly toward the MT plus end (especially at low loads), through a coiled coil and cargo-binding domain that link the heads and the cargo [75, 76]. A common theme in the motility of all motors is binding, release from the polar tracks, and subsequent rebinding of the motor head to the target binding site (TBS) [72, 77]. These processes, which result in a single step fueled by ATP consumption, involve not only coordination between the motor heads but also allosteric communication between the motor heads and regions of the polar track spanning several nanometers.

A number of remarkable studies [49, 68, 77–80] have been used to unravel the stepping mechanisms of motors (especially kinesin and myosin). Of particular relevance here are single-molecule experiments with kinesin [25,66,70,81,82], which have

provided considerable insight into the global processes that power the trailing head (TH) toward the microtubule (+) end. Single-molecule measurements of the time-dependent changes in the cargo attached to the coiled coil show that the motor head jumps between the tubulin-binding sites on a timescale that is much shorter than the waiting time between steps [43]. In order to reveal the molecular changes that occur during the jump time, which are difficult to quantify using experiments alone, we have simulated the kinematics of a single step using a coarse-grained model for the MT-kinesin complex. The new model and Brownian dynamics simulations with hydrodynamic interactions are used to answer the following questions: (1) What fraction of a single step is associated with the energetically favored conformational transitions that are linked to the power stroke? (2) How far does the trailing head move by tethered diffusion? (3) What are the key interactions that propel the TH to move predominantly parallel to a single protofilament of the MT?

Although the MT usually contains 13 protofilaments, kinesin walks on a single protofilament under normal operating conditions [24, 82, 83]. During a single step, the TH detaches from the initial $\alpha\beta$-tubulin binding site (the circle with hash marks in Fig. 2.1b), passes the MT-bound leading head (LH), and reattaches to the target $\alpha\beta$-tubulin binding site 16 nm away on the same protofilament (Figs. 2.1a and 2.1b). The target binding site (shown in green in Fig. 2.1b), however, is just one of several accessible $\alpha\beta$-tubulin binding sites along the 16 nm trip (Fig. 2.1b). Some of the potential binding sites on the curved MT surface are too far away for the TH to access them (Fig. 2.1b). However, the sites marked in pink and red can be reached by stretching the neck linker (NL) but are largely avoided during

the stepping process. It has been proposed that the conformational change from a disordered to an ordered state in the neck linker upon docking to the LH propels the TH toward the (+) end of the MT, and hence can be considered to be the power stroke [35,37]. The neck linker (shown in yellow in Fig. 2.1c) is a peptide containing 13 residues that connects the motor heads to the N-terminal of the coiled coil (the dimerization domain). When both heads are bound to the MT, the LH neck linker extends backward and does not interact with the rest of the LH [37]. Upon ATP binding to the LH, the neck linker undergoes a conformational change [35,37–42] and extends forward and docks to the cover strand and the central β-sheet of the LH. Such a conformational change (disorder $\rightarrow$ order transition) results in undocking and docking of the NL, which plays a crucial role in detaching the TH from the MT and propelling it toward the (+) end of the MT as it searches for and locates the TBS.

A number of observations suggest that conformational changes in the neck linker are necessary for the stepping kinetics of kinesin. First, immobilization of the neck linker by crosslinking it to the motor domain inhibits kinesin motility [84]. Second, disfavoring neck linker docking decreases the stall force [42]. Third, replacement of the neck linker by extended or flexible peptide impairs coupling between ATP turnover and the 16 nm step [82, 85]. Finally, the strain in the neck linkers serves as a gating mechanism so that the two heads can operate out of phase to execute the observed processive motion [68, 70, 82]. However, the adequacy of the neck linker docking model as the sole structural basis for explaining the stepping mechanism has also been questioned [68, 79], in part because the length

of a fully stretched neck linker is short of the 16 nm distance between the initial and the target binding sites [68]. In addition, it is still unclear how much of the energy released during ATP binding is used to trigger neck linker docking [68,86,87]. Thus, the consequences of neck linker docking, which appears to be the most visible conformational change during the kinesin step, occurring on a timescale of tens of μs, have not been revealed at the molecular level.

In this study, we provide a comprehensive view of the molecular events during kinesin stepping using simulations based on a coarse-grained model that is the first of its kind, to our knowledge. We explore the link between neck linker docking, directed diffusion, and the strength of interaction between the TH and the microtubule in relation to the kinematics of the kinesin step. Our simulations quantify the fraction of the step from the power stroke (NL docking) and due to the tethered diffusion, which have proved difficult to resolve using experiments, because the jump times (tens of μs) are considerably shorter than the time between steps. We show that although NL docking results in only (5-6) nm movement of the TH along the microtubule, it not only prevents reattachment to the starting site but also is essential in minimizing the probability of taking side steps at an optimum value of interaction strength between the motor head and the MT. By performing a number of mutation simulations we find, in accord with experiments [82], that enhancing the flexibility of the neck linker results in increased probability of taking side steps. Our results show that the stepping kinetics occurs in three major stages, the first of which is neck linker docking, which poises the TH to move predominantly toward the (+) end along a single protofilament of the microtubule. In the second stage, the

TH undergoes tethered directed diffusion, characterized by anisotropic translational motion but isotropic rotation. Surprisingly, a substantial fraction of the step occurs during this stage. Finally, optimal interaction between the microtubule and the TH is required to complete the step with minimal probability of taking side steps, which highlights the important role that the microtubule plays in facilitating the directed motion of the motor head.

2.3 Results and discussion

In order to explore the roles of neck linker docking to the leading head and the interaction between the TH and the MT binding sites in the stepping process, we performed a variety of simulations. The details of the simulations are in Appendix A and Appendix B. The two key parameters that control the kinematics of kinesin stepping are ϵ_h^{LH-NL}, the strength of interaction between the residues in the neck linker and those in the LH, and ϵ_h^{MT-TH}, measuring the strength of interaction between the TH and potential binding sites on the MT (see Eq. B.1 in the Appendix B, describing the force field). Docking of the NL to the LH is favorable only if ϵ_h^{LH-NL} exceeds a threshold value (see below). Further increase in ϵ_h^{LH-NL} makes neck linker docking more favorable. Similarly, increase of ϵ_h^{MT-TH} results in stronger affinity between the TH and the MT binding sites. Most of the results presented correspond to $\epsilon_h^{LH-NL} = 2.0$ Kcal/mol, resulting in rapid docking, and $\epsilon_h^{MT-TH} = 0.2$ Kcal/mol, for which the probability of the TH taking side steps is minimal. We also varied both ϵ_h^{LH-NL} and ϵ_h^{MT-TH} to ascertain their effects on the kinematics of a single

step.

2.3.1 Simulated cargo movement under a resistive load compares well with experiment

To validate the model (see Fig. A.1 in Appendix A for the structure of the complex) and the simulation strategy, we first calculated the movement of the cargo when a resistive force is applied in the (-) direction of MT (Fig. 2.1c). The resulting setup (Fig. 2.1c) mimics the experimental conditions by Carter and Cross [81], who found, by monitoring the time-dependent changes in the cargo position, $x_{cargo}(t)$, that if the resolution time exceeds $\sim$ 25 μs, the cargo moves by $\sim$ 8.1 nm without taking substeps. The calculated $x_{cargo}(t)$ for a 500 nm cargo, averaged over 99 trajectories, under a resistive load of 5 pN is in good agreement with experiments (Fig. 2.1c, top right). Our simulation results can be fit using $x_{cargo}(t) = A(1-e^{-t/\tau_c})$, where A = 6.4 nm and τ_c = 16.6 μs. The values of A and τ_c obtained in experiments (Fig. 2.1c, top right, black line) are 7.4 nm and 15.3 μs, respectively (Fig. 3 in [81]), which shows that our simulations capture the global features of the mechanics of a single kinesin step.

2.3.2 Trailing head moves $\sim$ 6 nm upon neck linker docking

In order to dissect the molecular events during the stepping process, we focused on the consequences of docking of the NL to the LH. From the distribution of first passage times for the NL to dock to the LH, calculated from (100-200) trajectories

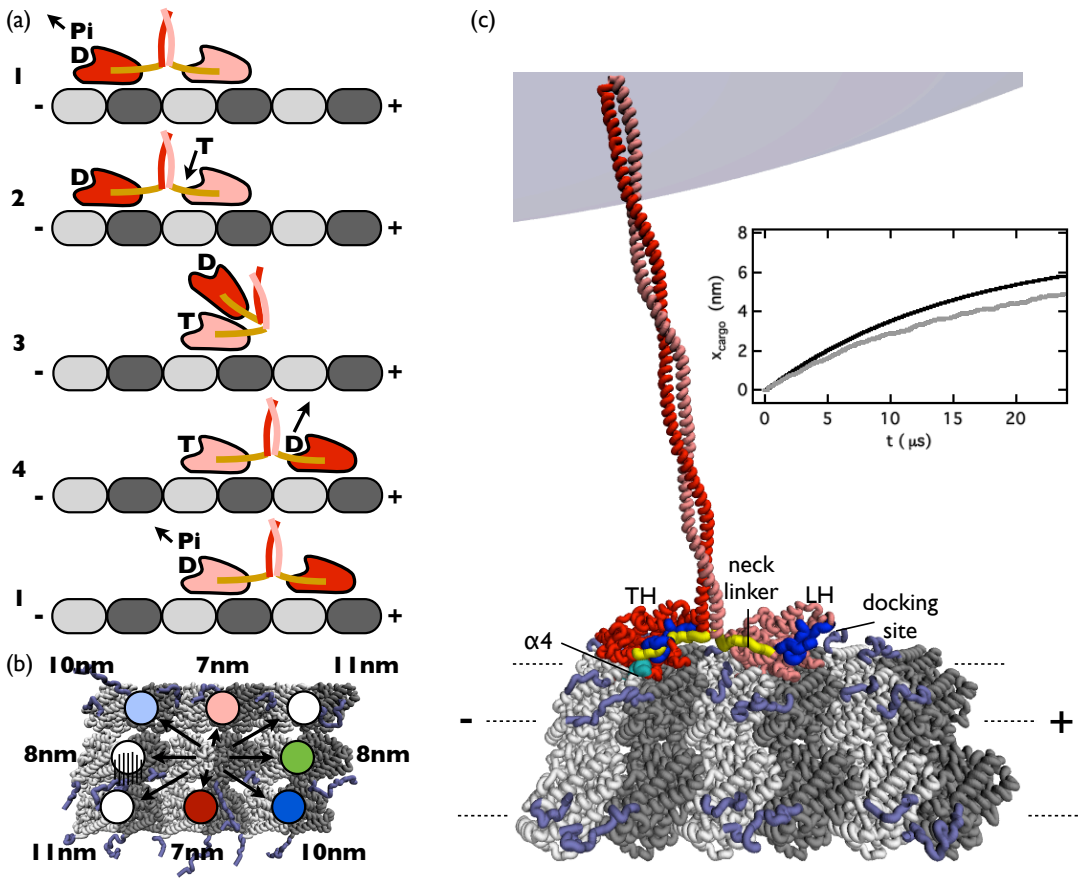

Figure 2.1: Coarse-grained simulation setup and validation

(a) Catalytic cycle of kinesin. The trailing head (TH) is shown in red and the leading head (LH) is in pink. ATP, ADP, and Phosphate are represented by T, D, and Pi, respectively. Binding of ATP, release of ADP, and Pi are indicated by incoming and outgoing arrows. (b) Distances to the various binding sites from the central location corresponding to the bound LH. The distances are between the centers of the binding sites. Pink and red circles are potential sites to which the TH can bind based on the geometry of the MT-Kin complex.. (c) The structural model of the complex used in the simulations (see Appendix A for details); α- and β-tubulin are in silver and gray, respectively, and are augmented by ehooks (violet). The TH is in red, and the LH is shown in pink. The neck linker is shown in yellow, and its docking site is in blue. Part of the 500 nm cargo is also shown. The microtubule binding the $\alpha 4$ helix of the TH is in cyan. The top right panel shows the average cargo movement along the MT axis during single 8 nm steps under a 5 pN resisting load obtained using simulations (gray line). The corresponding experimental result from Carter and Cross [81] is shown in black. Good agreement between simulations and experiment validates the model.

for which ordering is complete (Eq. 2.1 in *Analysis of trajectories* (chapter 2.5)), the mean NL docking time $< \tau_{NL} >$ ranges from 0.10 to 0.39 μs (see Table B.1 in Appendix B), depending on ϵ_h^{LH-NL}. During docking of the NL, the vector connecting the N and C termini of the NL of the LH (referred to as LH-NL), which initially points toward the (-) end of the MT (Fig. 2.2a, top), undergoes an $\sim$180° rotation and is directed toward the MT (+) end (Fig. 2.2a, middle structure). Concurrently, the TH detaches from the initial binding site. The location of the center of mass of the TH at the instant when NL docking is complete is displayed in Fig. 2.2b. The distribution, P(x_{TH}^d), of x_{TH}^d, the distance traveled by the center of mass of the TH along the MT axis (x axis), calculated from the data in Fig. 2.2b, shows that upon completion of NL docking, the mean $< x_{TH}^d > = 5.2 \pm 0.1$ nm (Fig. 2.2c), which is $\sim$ 11 nm shy of the TBS. The small value of $< x_{TH}^d >$ can arise because movement of the TH lags behind NL docking to the LH. We rule out such an explanation, because the C-terminal residue T338 of the LH-NL moves only 6.0 ± 0.01 nm along the MT when NL docking is complete (Fig. 2.2c). Thus, NL docking and the movement of the center of mass of the TH are almost synchronous.

The nature of diffusive motion of the TH can be gleaned from the time dependence of x_{TH}, x_{TH}(t) rises sharply, reaching $\sim$ 6 nm upon completion of docking. Subsequently, the TH undergoes diffusive motion until the step is complete. The diffusion time ($\sim$20 μs in Fig. 2.2d), which varies from trajectory to trajectory, is in the range (10-30) μs. These observations suggest that a large fraction ($\sim$0.6) of the total step occurs by stochastic search for the TBS, and not merely due to the power stroke generated by conformational changes in the neck linker.

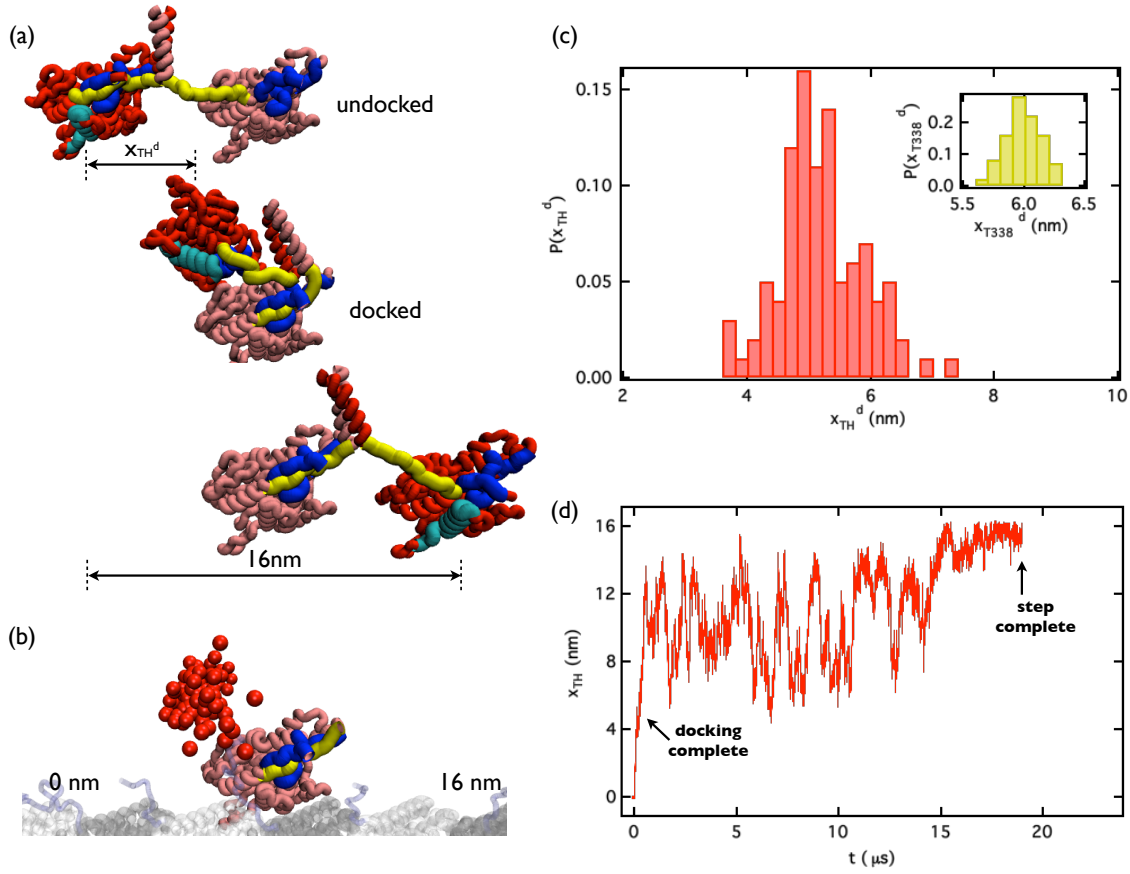

Figure 2.2: Dynamics of neck linker docking

(a) The LH and TH at the beginning (top) and end (middle) of neck linker docking to the LH, and at the end of a 16 nm step (bottom) in a representative trajectory. The center-of-mass displacement of the TH along the microtubule axis during neck linker docking is x_{TH}. (b) Location of the TH (red sphere) from 99 trajectories when neck linker docking to the LH is complete. (c) Histograms, based on 99 trajectories, of the TH movement (red) during neck linker docking to the LH. The inset shows distributions of the position of T338 of the LH. (d) Time-dependent changes in the center of mass of the TH as a function of t for a sample trajectory. The arrow shows that NL docking is complete in $\sim$1 μs and the stepping time is $\sim$20 μs. The values of ϵ_h^{LH-NL} and ϵ_h^{MT-TH} are equal to 2.0 and 0.2 Kcal/mol, respectively.

To further confirm that NL docking does not lead to completion of a full step, we performed several additional simulations by altering the key parameters in the force field (see Table B.1 in Appendix B). These simulations, in which (100-200) trajectories were generated for several force-field parameters (variations in ϵ_h^{LH-NL} and ϵ_h^{MT-TH}, and changes in the dielectric constant of the electrostatic interactions) also show that upon completion of NL docking, the TH step is incomplete (detailed in Table B.1 in Appendix B). Besides establishing the robustness of the results to changes in the force-field parameters, the complete set of results shows that NL docking alone, without directed diffusion, is insufficient to drive the TH to the neighborhood of the TBS [68, 80].

2.3.3 Minimizing the probability of side steps requires neck linker docking and optimal interaction between the motor head and the microtubule

How are side steps largely avoided, even though they are within easy access of the TH? To answer this question, we considered the possibility that NL docking and appropriate interactions with the MT reduce the probability that the TH will bind to $\alpha\beta$-tubulin binding sites on MT (pink and red circles in Fig. 2.1b). From geometrical considerations alone, it appears that NL docking to the leading head (Fig. 2.1b) restricts the TH from reaching several sites (white and light blue circles in Fig. 2.1b) even if the NL of the TH is fully stretched. However, Fig. 2.1b also shows that even after NL docking, the sites that are above and below the central

binding site (pink and red circles in Fig. 2.1b) to which the LH is anchored are accessible, as they are within reach of the stretched NL of the TH. Thus, favorable energetics must bias the TH so that the TBS is reached with substantial probability within the typical stepping time of $\sim$25 μs.

We surmise that the motor head is correctly bound to the TBS if the structure is similar to that found in the cryoEM-image of Kin-MT complex [88], which implies that both the distance and orientational criteria (Eqs. 2.3, 2.4, and 2.5 in *Analysis of trajectories* (chapter 2.5)) must be simultaneously satisfied. Incorrect binding would lead to side steps, which is realized by the TH binding to $\alpha\beta$-tubulin on neighboring protofilaments (red, pink, or dark blue circle in Fig. 2.1b), occurring in the same manner as steps to the TBS. In order to provide structural details of how NL dock- ing to the LH prevents side steps, we performed simulations using a mutant in which NL docking is made energetically unfavorable ($\epsilon_h^{LH-NL} = 0$) so that docking is prevented (see Appendix B for details). Such a construct may be realized in experiments either by deleting the cover stand [41, 42] or by replacing the NL with glycine-serine repeats [82].

2.3.4 Consequences of neck linker docking

We find that minimizing the probability of taking side steps requires optimal values of ϵ_h^{MT-TH} and docking of NL to the LH, which requires that ϵ_h^{LH-NL} exceed a threshold value (see below). Fig. 2.3a shows that in the absence of NL docking to the LH (ϵ_h^{LH-NL}), the probability of the TH taking a 16 nm step by binding to the

TBS is zero, independent of ϵ_h^{MT-TH}. For $\epsilon_h^{LH-NL} = 2.0$ Kcal/mol, the docked NL is almost intact on the timescale of a single step, thus preventing the detachment of the TH from the MT. The mean docking time, $< \tau_{NL} >$, increases from about 0.10 ms to a value greater than 3.7 μs as ϵ_h^{LH-NL} decreases from 2.0 kcal/mol to 0.4 kcal/mol. Further decrease in ϵ_h^{LH-NL} makes NL docking unfavorable. Fig. 2.3b shows that if ϵ_h^{LH-NL} decreases below 0.3 kcal/mol, then NL does not dock in a stable manner, as assessed by $\Delta_{NL}(t)$ (Eq. 2.1 in *Analysis of trajectories* (chapter 2.5)), even on timescales on the order of $\sim$5 μs.

Comparison of the wild-type (WT) and mutant simulations shows that NL docking to the LH is largely responsible for ensuring that the TH moves with substantial probability toward the target binding site. Besides decreasing the probability of side steps (see below), NL docking to the LH also prevents rebinding of the TH to the initial binding site. In order to demon- strate this particular consequence of NL docking, we first calculated the distribution P(L), where L = $|\vec{R}_{T338}^{TH}(0) - \vec{R}_{T326}^{TH}(0)|$ (Fig. 2.3c) is the distance between T338 and T326 of the TH neck linker at t=0. At t=0,P(L) peaks at $\sim$3.8 $\pm$ 0.05 nm(red in Fig. 2.3c), which is the equilibrium value of L when the motor head is bound to the initial $\alpha\beta$-tubulin binding site. In contrast, the distribution of $|\vec{R}_{T338}^{TH}(\tau_{NL}^i) - \vec{R}_{T326}^{TH}(0)|$, where i labels the ith trajectory (Fig. 2.3c), peaks around 9.8 nm (blue in Fig. 2.3c). Thus, once docking is complete, resulting in tension in the leading head NL (see below), the detached TH is too far away from the initial binding site, so that rebinding cannot occur provided ϵ_h^{LH-NL} is sufficiently large. At small values of ϵ_h^{LH-NL}, however, NL docking is reversible (Fig. 2.3b), which could result in the TH binding to the initial

binding site.

2.3.5 Effect of the interaction between the trailing head and the microtubule)

The majority of side steps observed in the mutant simulations correspond to the TH binding to the middle $\alpha\beta$-tubulin on the right protofilament adjacent to the LH-bound $\alpha\beta$-tubulin on the central protofilament (Figs. 2.1b and 2.4a), even though the pink circle is at the same distance as the red site (Fig. 2.1b). In a small fraction of trajectories, the TH is trapped in other binding sites with correct orientation. This result suggests that diffusion alone, without any additional biasing mechanism favoring the target binding site, cannot explain the observation that kinesin walks predominantly on a single protofilament under normal operating conditions [24, 82, 83]. The probability of taking side steps, P_{ss} (Eq. 2.6 in *Analysis of trajectories* (chapter 2.5)), depends on ϵ_h^{MT-TH} (the blue line in Fig. 2.3a), even when NL docking is highly favorable, $\epsilon_h^{LH-NL} = 2$ Kcal/mol. When the MT-TH interaction is strong ($\epsilon_h^{MT-TH} = 2$ Kcal/mol), only 25% of the trajectories locate the TBS. The remaining trajectories are kinetically trapped in adjacent $\alpha\beta$-tubulin sites (Fig. 2.4a) for timescales exceeding $\sim$25 μs, with the kinesin-MT interface formed only partially. As ϵ_h^{MT-TH} decreases, P_{ss} decreases dramatically, reaching a minimum at ~ 0.11 (Fig. 2.3a), which is remarkably close to the experimental estimate for the wild-type [82]. Our findings support the conclusion that rapid disorder $\rightarrow$ order transition of the leading-head neck linker decreases the probability

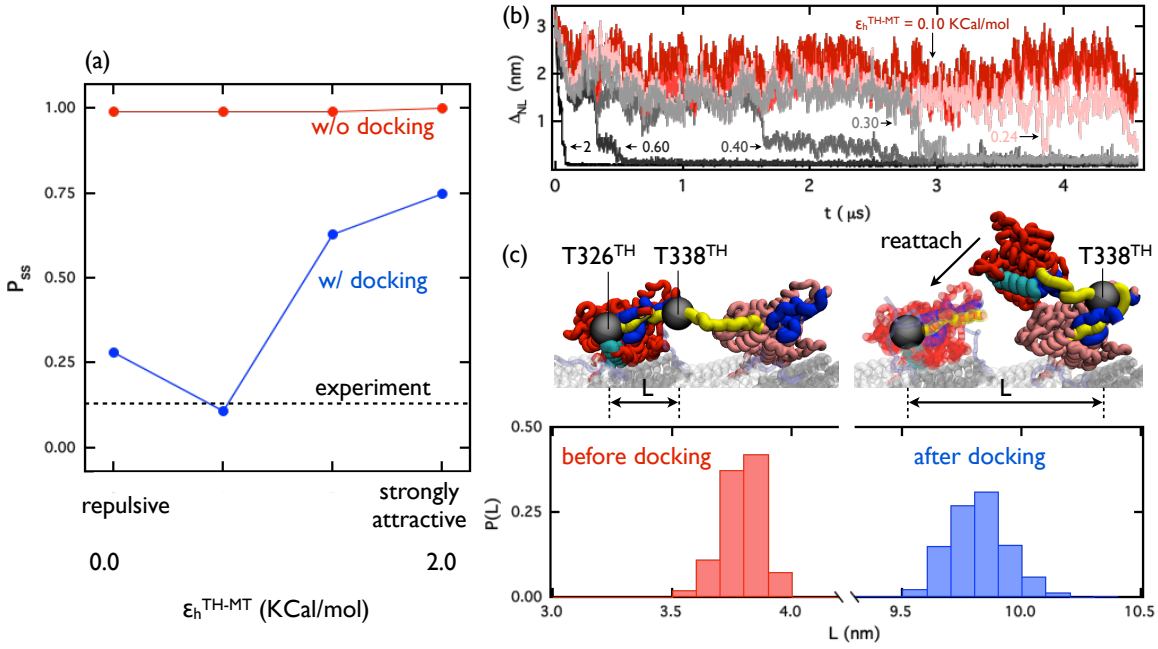

Figure 2.3: Consequences of neck linker docking

(a) Probability of side steps, P_{ss}, as a function of MT-TH interaction. Repulsive, weakly attractive, attractive, and strongly attractive corresponds to ϵ_h^{MT-TH} (Eq. B.1 in the Appendix B) values of 0.0, 0.2, 0.4, and 2.0 Kcal/mol, respectively. The dotted line corresponds to the probability, observed in experiments, that the TH takes side steps in wild-type kinesin (13%) [82]. (b) Time-dependent changes in Δ_{NL}(t), the measure (Eq. B.1 in simulation methods) used to assess the extent of docking of the NL to the leading head as a function of ϵ_h^{LH-NL}. The curves in various shades of gray show that docking is complete ($\Delta_{NL}(t) < \Delta_c$), those in pink and red show that $\Delta_{NL}(t) > \Delta_c$. (c) The structure on the left shows the locations of T326 and T338 in the TH bound to the initial binding site. The distance between these residues is less than 4 nm. The structure on the right shows the location of residue T338 of the TH after NL docking to the LH, and the location of residue T326 of the TH assuming the TH reattaches to the initial binding. The bottom panel shows the distribution of $|\vec{R}^{TH}_{T338}(0) - \vec{R}^{TH}_{T326}(0)|$ and $|\vec{R}^{TH}_{T338}(\tau^i_{NL}) - \vec{R}^{TH}_{T326}(0)|$ based on 200 trajectories, where τ_{NL} is the time at which NL docking to the LH is complete in the ith trajectory.

of side steps [89]. The dependence of P_{ss} on the TBS requires robust NL docking (ϵ_h^{LH-NL} should exceed at threshold value for docking to be favorable) as well as relatively weak MT-TH interaction. These results further imply that ADP release, which would result in an effective increase in ϵ_h^{MT-TH}, should occur late in the stepping process. Thus, besides ensuring that the TH predominately moves toward the (+) end of the MT, docking of the NL decreases the probability of long-lived side steps, provided ϵ_h^{LH-NL} and ϵ_h^{MT-TH} are in the appropriate ranges.

2.3.6 Flexibility of disordered neck linker of the leading head results in side steps

Time-dependent changes in $R_y(\mathrm{t}) = \hat{e}_y \cdot [\vec{R}^{TH}_{T326}(t) - \vec{R}^{LH}_{T326}(t)]$, the total extension of TH-NL and LH-NL projected along the y axis that is perpendicular to the central protofilament, for a sample trajectory, illustrate that the docking state of the NL determines the probability of taking side steps (Fig. 2.4). From the geometry of the MT (Fig. 2.1b), it follows that for a side step with correct orientation, R_y (Fig. 2.4a) should extend by at least ∼6 nm (Fig. 2.4b). Thus, both TH and LH neck linkers must extend to account for the needed ∼6 nm. Because the NL of the trailing head is disordered and hence flexible, it can make sideways excursions readily. The probability of the NL of the LH extending sideways greatly depends on its docking state (Figs. 2.4c and 2.4e). Upon docking, sideways movements of the NL are strictly prohibited (see the gray lines in Fig. 2.4c) whereas they can occur if docking is energetically unfavorable (black lines in Fig. 2.4c), which we mimic

with $\epsilon_h^{LH-NL} = 0$ Kcal/mol. Comparison of Figs. 2.4b-2.4d shows that if the TH takes side steps, then the NL of the LH should extend sideways by $\sim$4 nm, while the more flexible NL of the TH should extend sideways by $\sim$2 nm. Thus, as long as the NL of the LH is docked (ϵ_h^{LH-NL} exceeds a threshold value), even with the full extension of the NL the TH cannot take side steps readily (gray lines in Fig. 2.4), especially when MT-TH interaction is weak. These calculations provide a structural explanation of why the WT kinesin appears to walk predominantly along a single protofilament under normal operating conditions [24,82,83] on timescales exceeding ~ 25 μs.

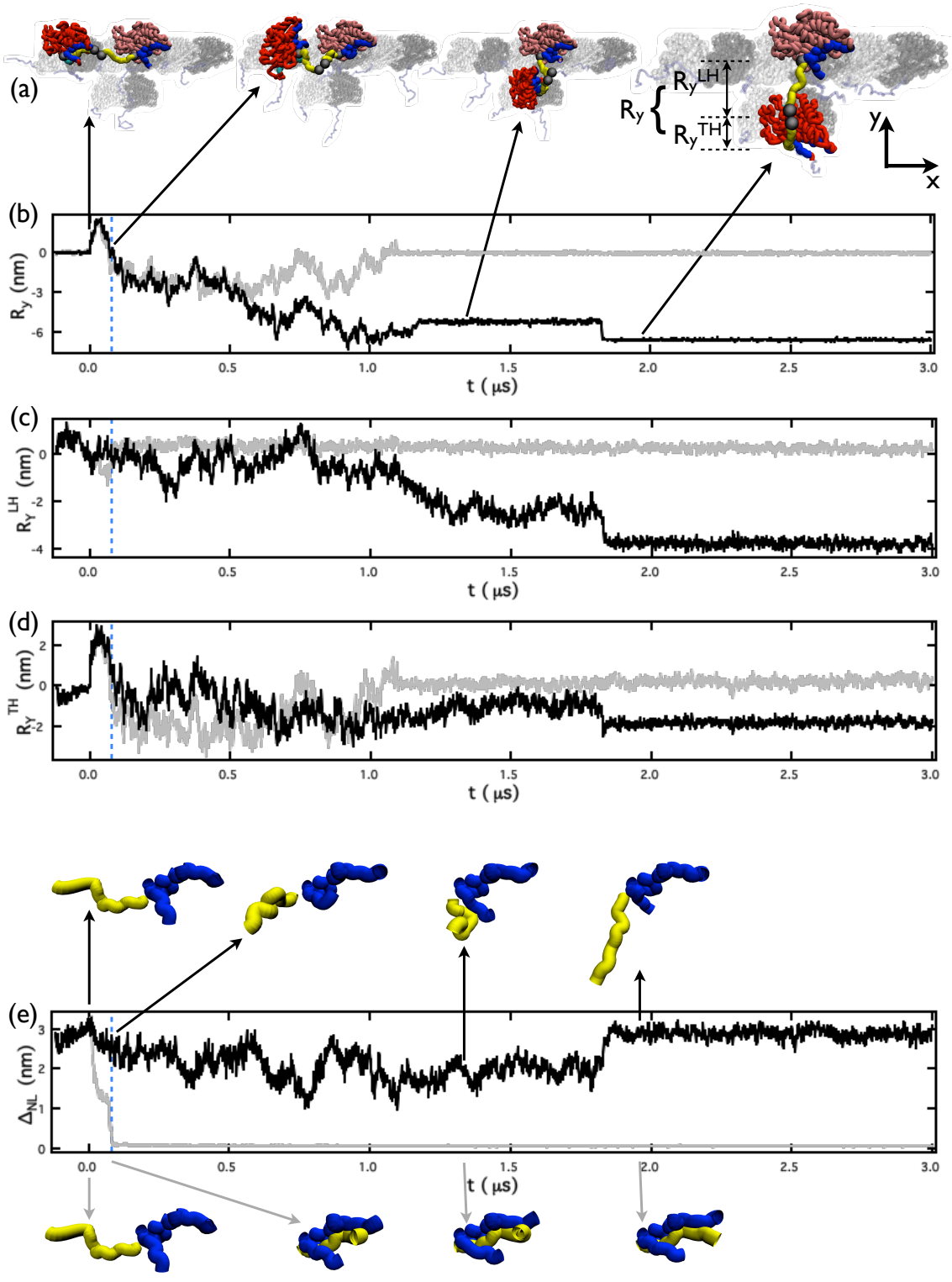

Figure 2.4: Flexibility of the disordered neck linker of the leading head leads to side steps

Figure 2.4: Flexibility of the disordered NL of the LH leads to side steps

(a) Four sequential snapshots in a representative trajectory, in which the TH binds to the middle $\alpha\beta$-tubulin on the adjacent protofilament corresponding to the red circle in Fig. 2.1b. It shows (1) the beginning of a step, (2) detachment of the TH from the initial binding site, (3) interaction of the TH with tubulin on the neighboring site, and (4) binding of the TH to the tubulin with correct orientation. (b) R_y(t) is the total extension of the TH-NL and the LH-NL projected along the y axis as a function of time for a normal 16 nm step (gray). The black line, corresponding to NL docking being unfavorable, shows that a side step requires a minimum of $\sim$6 nm of side extension. (c) $R_y^{LH}(\mathrm{t}) = \hat{e}_y \cdot [\vec{R}_{T338}^{LH}(t) - \vec{R}_{T326}^{LH}(t)]$, the extension of LH-NL projected along the y axis as a function of time, shows that a side step requires $\sim$4 nm of side extension from LH-NL (black line). (d) Same as (c), except this gives the contributions due to stretching of the TH to R_y(t) when NL docking is favorable (gray line) and unfavorable (black line). (e) Δ_{NL}(t) (defined in Eq. 2.1 in *Analysis of trajectories* (chapter 2.5)), the distance between LH-NL and LH, is plotted as a function of time for both favorable (gray) and unfavorable docking (black). Conformations of the NL of both the TH and LH at various instances are given. The results represented by gray and black lines in (B)-(E) were computed using $\epsilon_h^{LH-NL} = 2.0$ and 0.0 Kcal/mol, respectively. The value of ϵ_h^{MT-TH} was set to 2.0 Kcal/mol.

2.3.7 Binding to the target site on the microtubule occurs in three major stages

Attachment to the TBS involves three distinct stages: (1) NL docking to the LH, followed by (2) anisotropic directed diffusional search, and finally by (3) recognition and binding to the TBS with correct orientation (see Fig. 2.5a). In these simulations, we set $\epsilon_h^{LH-NL} = 2.0$ Kcal/mol but varied ϵ_h^{MT-TH}. We monitored the progress of the stepping process using d(t) and the two angles θ_1 and θ_2 (Eqs. 2.3-2.5 in *Analysis of trajectories* (chapter2.5)), which specify the orientation of the TH, as order parameters to assess binding of the TH to the TBS. The values of d, θ_1 and θ_2 are ≈ 0 when TH is correctly bound to the TBS.

The TH reaches the neighborhood (d $\approx$ 4 nm) of the TBS by an anisotropic diffusive process in a few ms depending on ϵ_h^{MT-TH}. In analyzing the dynamics in the second stage, we used only the portion of the trajectories after NL docking is complete and prior to the TH reaching the neighborhood (d $\approx$ 4 nm) of the MT (gray regions in Figs. 2.5b-2.5d). The diffusion coefficients, calculated from the slopes of the mean-square displacements along the x, y, and z components of the center of mass of the TH, yield $D_x \approx D_y \approx 15\mu m^2/s$ (Fig. B.1 in Appendix B), whereas linear transport perpendicular to the MT surface is slow, with $D_z \approx 3\mu m^2/s$. In contrast, the isotropic translational diffusion coefficient of the TH using Hydropro [90] is $D_x = D_y = D_z = D_{iso} \approx 26\mu m^2/s$. The TH also undergoes rotational diffusion (Figs. 2.5b-2.5d), which unlike translational diffusion is essentially free. The isotropic rotation time constant is $\tau_R \approx 0.28\mu s$, obtained from the decay of

the orientational autocorrelation function (see Fig. B.1 in Appendix B), and the corresponding value from Hydropro [90] is $\approx 0.21\mu s$. These results show that the second stage, constituting the major fraction of the step, involves directed diffusion of the TH with anisotropic translational diffusion but isotropic rotational motion.

The final stage, during which the TH attaches to the TBS with proper orientation ($\theta_1 \approx \theta_2 \approx 0$) and with d ≈ 0, can be directed and depends on the strength of the MT-TH interaction, and hence the nucleotide state of the motor head. Upon first entering the neighborhood of the TBS (d ≈ 4 nm), which occurs at the end of the anisotropic diffusive stage, the orientation of the TH with respect to the MT deviates substantially from that found in the Kin-MT complex (Figs. 2.5b-2.5d; Fig. B.2). Binding to the TBS with proper orientation could occur either purely by rotational diffusion or can be altered by changing ϵ_h^{MT-TH}. In order to distinguish between these two possibilities, we varied the ϵ_h^{MT-TH} from 0.0 to 2.0 Kcal/mol. For $\epsilon_h^{MT-TH} = 0$, even after entering the neighborhood of the TBS, the TH stochastically samples a broad range of d (see Fig. 2.5b and Fig. B.2e), θ_1 (Fig. 2.5b and Fig. B.2f), and θ_2 (Figs. B.2g) values. As expected in a purely diffusive process, the TH fluctuates in and out of the neighborhood of the TBS, without forming the required interface with the TBS for a 16 nm step (see Figs. B.3a-B.3c). Thus, in the absence of specific interactions between the motor head and the MT, the TH cannot bind to the $\alpha\beta$-tubulin with substantial probability.

The dynamic behavior for non-zero ϵ_h^{MT-TH} is dramatically different (Figs. 2.5c and 2.5d; Fig. B.2). For $\epsilon_h^{MT-TH} = 0.2$ Kcal/mol, for which P_{ss} is smallest (Fig. 2.3a), the TH undergoes rotational and translation diffusion even when d

$\leq$ 3 nm (Fig. 2.5c; Fig. B.3b). The stochastic motion finally ceases only after multiple trials (Fig. 2.5c), resulting in the capture of the TH by the $\alpha\beta$-tubulin, thus completing a full step. In contrast, for $\epsilon_h^{MT-TH} = 2.0$ Kcal/mol, once the TH approaches the neighbor- hood of the MT, with both θ_1(t) and θ_2(t) appreciably different from zero, the MT-TH interaction is sufficiently strong that orientational ordering occurs rapidly (see Fig. 2.5d and Fig. B.3c for a representative trajectory), resulting in the rapid cessation of translational and rotational diffusion.

The nature of arrest of translational and rotational diffusion in the final stages of stepping, leading to the capture of the TH by the TBS and completion of the step, illustrates the crucial role played by interaction of the TH with the MT. The rate of orientation arrest depends on the strength of specific interactions between the TH and the TBS (Figs. 2.5b-2.5d; Figs. B.2e-B.2g and Fig. B3 in Appendix B). Although several crystal structures [91, 92] reveal how such interactions are affected by ADP release, when the release occurs during the 16 nm step is unclear. Our simulations point to two mutually conflicting requirements for optimal stepping dynamics. A large value of ϵ_h^{MT-TH} results in rapid orientational ordering of the TH with respect to the TBS. However, the increased rate comes at the expense of enhanced probability of side steps (Fig. 2.3a). When $\epsilon_h^{MT-TH} = 0$, the probability of docking to the TBS is zero. Thus, an optimal value of ϵ_h^{MT-TH} leads to the smallest P_{ss} (Fig. 2.3a) and high probability of reaching the TBS, resulting in the correct MT-Kin interface. The importance of MT-Kin interactions in facilitating stepping has been emphasized in a number of experiments (see, for example, [93]).

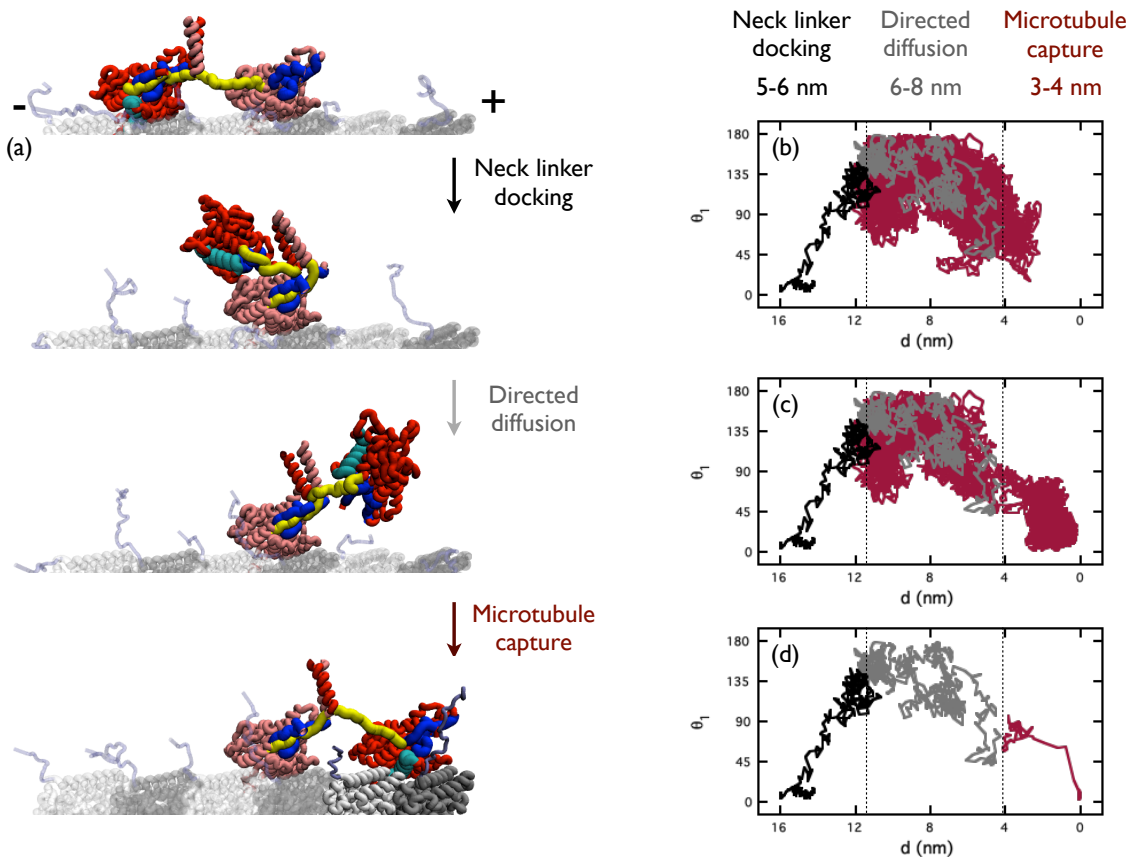

Figure 2.5: Major stages during a single step

(a) Four snapshots in a representative trajectory, corresponding to (top to bottom) the beginning of the step, the end of neck linker docking to the LH, the end of constrained diffusion, and the end of microtubule capture. Times for the three major steps are indicated. The time for directed diffusion varies from 1.8 to 3.0 μs depending on ϵ_h^{MT-TH}, the strength of MT-Kin interaction. The time for binding to the TBS occurs in 5.5 $\pm$ 0.6, 1.8 $\pm$ 0.4, and 0.5 $\pm$ 0.2 μs for ϵ_h^{MT-TH} of 0.2, 0.4, and 2.0 Kcal/mol, respectively. Microtubule capture is not observed within 25 μs in simulations with repulsive MT-TH attraction ($\epsilon_h^{MT-TH} = 0$ Kcal/mol). (b-d) Orientation of the TH (θ_1) as a function of d, the center-of-mass distance between the TH and TBS, in three trajectories, in which the MT-TH interaction is repulsive (b), weakly attractive (c), or strongly attractive (d). Each trajectory can be dissected into three stages: neck linker docking (black), constrained diffusion (gray), and microtubule capture (red). A similar plot of θ_2 as a function of d is in Fig. B.3.

2.4 Simulation methods

Although progress is being made in the use of atomically detailed models to simulate some aspects of molecular motors [94, 95], the large size of the MT-Kin complex makes it necessary to use coarse-grained models. We performed Brownian dynamics simulations with hydrodynamic interactions using the self-organized polymer (SOP) model for the MT and conventional Kinesin. In the simplest version of the SOP model, each amino acid is represented by a single interaction center located at the α-carbon. Previous applications have shown that the SOP model is successful in a number of applications (single-molecule force spectroscopy of proteins [96] and RNA [97], allosteric transitions in the chaperonin GroEL [98], ATP-induced detachment of myosin V from actin [99], and force-induced rupture of $\alpha\beta$-tubulin [100,101]). With the SOP representation of the entire system of kinesin, the coiled coil, and the MT, we generated long multiple trajectories, which allow us to obtain a detailed molecular picture of the mechanism that drives the kinesin step. Our construct for the MT-Kin complex, which closely resembles the experimental set-up and builds on a closely related model [89, 102], includes two motor heads, a 500 nm bead (cargo), and a 30 nm coiled coil that connects the motor heads to the cargo (see Appendix A for details). We also used three neighboring MT protofilaments in our simulation so that the role of MT in modulating the stepping dynamics can be directly assessed. At t = 0, the TH is bound to the $\alpha\beta$-tubulin at the (-) end of the center protofilament, and the LH is bound to the neighboring $\alpha\beta$-tubulin of the same protofilament (Fig. 2.1c). The LH neck linker (Fig. 2.1c) is undocked

(disordered) and points (from T326 to T338) backward toward the MT (-) end, while the TH neck linker (Fig. 2.1c) is docked (ordered), and points forward toward the MT (+) end.

Although we do not explicitly model ATP binding, the consequences of ATP binding and hydrolysis are explicitly taken into account in the simulations. We simulate NL docking induced by ATP binding by changing the interaction between NL and the motor head. Similarly, a weak interaction between the motor head and the binding sites on the microtubule mimics the ADP state. We triggered NL docking at t = 0 in the LH and undocking in the TH and detachment of the TH from the MT (see Appendix B for details). After detachment, the TH can reattach to any unoccupied non-minus-end $\alpha\beta$-tubulin binding sites (Fig. 2.1b). We generated a large number of trajectories for 30 μs or longer, which roughly coincides with the duration of jump of the cargo in single-molecule experiments.

We previously described the procedure for obtaining real times from simulations [103]. In order to ensure that this procedure is reasonable, we used simulations to calculate the translational and rotational diffusion constants of an isolated motor head. The simulations were in excellent agreement with the predictions based on HydroPro [90], without any adjustable parameter, which shows that the overall timescales associated with our simulations are accurate.

In order to provide structural basis of kinesin stepping we also performed a number of mutation simulations that further reveal how NL docking, characterized by ϵ_h^{LH-NL}, affects kinesin motility. Another important parameter that determines the kinematics of the kinesin step is the strength of interaction between kinesin and

MT, parameterized by the energy scale ϵ_h^{MT-TH} (see Eq. B.1 in the Appendix B). The affinity of the motor head for $\alpha\beta$-tubulin depends on the state of the nucleotide. Interaction between kinesin and the MT is strongest in the absence of nucleotide or when ATP is bound, and is weak when the motor head carries ADP. Thus, by varying ϵ_h^{MT-TH}, which in our simulations is changed from 0.2 to 2.0 kcal/mol, we can roughly mimic the state of the nucleotide. A small value of ϵ_h^{MT-TH} implies that ADP is bound to the TH during the stepping process, whereas $\epsilon_h^{MT-TH} = 2.0$ Kcal/mol may correspond to premature release of ADP from the TH.

2.5 Analysis of trajectories

Neck linker docking: To assess if neck linker is in the docked state, we first calculated

$$\Delta_{NL}(t) = \sqrt{\frac{\sum_{(i,j)} (r_{ij}(t) - r_{ij}^0)^2}{N}} \tag{2.1}$$

where i refers to a specific residue in LH neck linker and j belongs to the docking site, N is the total number of residue pairs that satisfy $r_{ij}^0 < 1$ nm. Residue j is a docking site for residue i if r_{ij} in rat monomeric kinesin structure (PDB code: 2kin) r_{ij}^0 is smaller than 1 nm. Second, we computed

$$\delta(t) = 1 - \widehat{e}_{NL}(t) \cdot \widehat{e}_{NL}(d) \tag{2.2}$$

where $\widehat{e}_{NL}(t)$ is the unit vector connecting T326 and T338 in the LH neck linker for a given t and $\widehat{e}_{NL}(d)$ is the corresponding unit vector in docked state. If $\Delta(t)$ and $\delta(t)$ are less than preset threshold values Δ_c and δ_c then we assume that the neck

linker is docked. In most of our simulations we use $\Delta_c = 0.08$ nm and $\delta_c = 0.2$. In some cases we also used $\Delta_c = 0.06$ nm and $\delta_c = 0.15$ to ensure that the conclusions do not depend on the precise values of Δ_c and δ_c (Table B.1 in Appendix B).

Binding of motor head to $\alpha\beta$-tubulin: We used two order parameters to monitor binding of TH to a specifc $\alpha\beta$-tubulin with proper orientation. The first is

$$d(t) = |\vec{r}_{cm}(t) - \vec{r}_{cm}(b)| \tag{2.3}$$

where $\vec{r}_{cm}(t)$ is the center of mass coordinate of the TH (residue 2 to 326) at time t, $\vec{r}_{cm}(b)$ is the center of mass coordinate of a motor head docked to a specific $\alpha\beta$-tubulin following assembly process (step II in Fig. A.1 of Appendix A). The reference state for assessing the correctness of motor head binding to the $\alpha\beta$-tubulin with the similar orientation is the MT-Kin complex structure 2p4n.pdb. The second is the orientational order parameter

$$\theta_1(t) = cos^{-1}(\widehat{e}_1(t) \cdot \widehat{e}_1(b)) \tag{2.4}$$

where $\widehat{e}_1(t)$ is the unit vector connecting L257 and A268 in the TH at t and $\widehat{e}_1(b)$ is the corresponding vector in the docked motor head. Similarly, we also considered

$$\theta_2(t) = cos^{-1}(\widehat{e}_2(t) \cdot \widehat{e}_2(b)) \tag{2.5}$$

where $\widehat{e}_2(t)$ is the unit vector connecting K227 and K315 in the TH for a given t and $\widehat{e}_2(b)$ is the corresponding vector in the docked motor head. If d(t), $\theta_1(t)$ and $\theta_2(t)$ are smaller than d_c (0.2 nm) and θ_c (15°) then we assume that the TH is bound to the $\alpha\beta$-tubulin with proper orientation.

Probability of side steps: From the dynamics of each trajectory we calculated the total residence time that the motor head spends in the neighborhood of an $\alpha\beta$-tubulin binding site in the protofilament that is adjacent tot the one containing the TBS (see Fig. 2.1). The probability of taking a side step

$$P_{ss} = \frac{\sum \tau_{ss}^{i}}{\sum \tau_{TBS}^{i} + \sum \tau_{ss}^{i}} \tag{2.6}$$

where the summation is over the total number of trajectories. We assume that TH is in the neighborhood of $\alpha\beta$-tubulin binding site if Root Mean Square Deviation (RMSD),

$$\Delta_{TH}(t) = \sqrt{\frac{\sum_{(i,j)} (R_{ij}(t) - R_{ij}^{0})^{2}}{N}} \tag{2.7}$$

between the TH and the binding site, is less than 4 nm. In Eq 2.7, R_{ij}(t) is the distance between residue i in the motor head and residue j in the MT at t and R_{ij}^{0} is the corresponding value in the MT-Kin complex. The summation in Eq. 2.7 is restricted to only values of $R_{ij}^{0} \leq$ 1nm.

2.6 Conclusion

We have provided detailed simulations of the structural basis of stepping of kinesin on microtubules. Besides the geometrical restrictions imposed by the polar track, two energy scales are needed to rationalize the experimental observations. One is the favorable interaction between the neck linker and the motor head required for docking and stretching of the neck linker. The other is the overall interaction between kinesin heads and the microtubule. The former has to exceed a minimum

value, while the latter has to have an optimal value to minimize the probability of the TH taking side steps. Our simulations, which provide a molecular description of the events that occur during the jump from one tubulin binding site to another, show that although NL docking to the LH moves the trailing head by less than 6 nm, it not only decreases the probability of the TH taking side steps but also prevents reattachment of the TH to the initial binding site. Therefore, besides directly pulling the motor head toward the target binding site, the power stroke also facilitates motility by regulating diffusion of the motor head so that binding to the target site is favored.

The major findings of our study support the conclusions of a number of single-molecule experiments, which showed that the primary consequences of NL docking are to (1) provide directionality of the TH movement toward the (+) end of the MT [35, 82], and (2) serve as a mechanism that prevents excursions of the TH to the neighboring $\alpha\beta$-tubulin binding sites. The present work also substantiates the importance of directed anisotropic diffusion during 16 nm steps [68,79,81,104]. Our work, which also elucidates how optimal interaction between the motor head and the micro- tubule facilitates motility of kinesin along a single protofilament, has additional implications. (1) Mutations or deletions that affect the MT-TH interaction will impair the processivity of kinesin. This prediction can be tested by mutations in either the MT [93] or the motor head [105] and by changing salt concentrations, which would also directly affect ϵ_h^{MT-TH}. (2) The enhanced probability of taking side steps, which occurs as the strength of MT-TH interaction increases, suggests that for efficient stepping, ADP release must occur only in the final stages (or after)

of the capture of the TH by the MT. In other words, ADP release time, τ_{ADP}, must approximately exceed the stepping time, τ_s. The inequality τ_{ADP} ($\sim$ms [19, 106]) is satisfied in practice.

Chapter 3

Quantification of the diffusive nature of kinesin motility

3.1 Summary

It is now firmly established that kinesin walks processively on microtubules (MTs) in an asymmetric hand-over-hand manner consuming one ATP molecule per 16 nm step. However, details of the contributions arising from docking of the approximately thirteen residue neck linker to the leading head (deemed to be the power stroke) and the potential role of diffusion of the trailing head to the 16 nm step are not fully understood. We use molecular simulations of a coarse-grained model of the microtubule-kinesin complex, which reproduces the measured stall force as well as the force required to dislodge the motor head from the MT, to show that nearly three quarters of the step is covered by bidirectional stochastic motion of the TH. However, docking of the neck linker constrains the extent of diffusion and minimizes the probability of kinesin taking side steps implying that both the events are necessary in the motility of kinesin. Surprisingly, we find that the trailing head stochastically hops hundreds of times between geometrically accessible neighboring sites on the MT before forming a stable interaction with the target binding site with correct orientation between the motor head and the α/β tubulin dimer.

3.2 Introduction

Many cellular processes, such as delivery of neuronal transmission through axon, and secretion of digestive enzyme by stomach cell, require directional transport of intracellular vesicles along cytoskeleton network [73]. Cellular transportation is carried out by motor proteins that preferentially move toward a certain direction along a particular polar cytoskeleton track [72]. For example, kinesin-1 (Kin1) or conventional kinesin, pulls cargo towards the plus (+) end of the microtubule (MT) [76]. It is now well established, thanks to a number of high precision experiments, that kinesin with two motor domains walks in a hand-over-hand manner [35, 43, 66, 74], hydrolyzing one ATP molecule per step [107]. Despite the small size of the motor domain, Kin-1 is a powerful and fast motor. It moves towards the + end of the microtubule (MT) resisting force up to 7 pN [27, 81], which is similar or larger than stall forces of bigger motors [77,108], such as dynein ($\sim$ 7 pN) and myosin ($\sim$ 3 pN). Kin-1 moves towards the + end processively at a speed of $\sim$ 800 nm / sec [27], which is clearly faster than dynein (100 nm / sec) [109], another motor protein that walks on MT but towards the minus end [108, 109]).

A remarkable series of experimental studies [68,78–80] from a number of groups has revealed many of the details of the stepping mechanism of kinesin. Two mechanisms have been proposed to explain how kinesin, small but fast and furious, uses chemical energy to walk towards the + end of the MT in a hand-over-hand manner. According to the "power stroke" model [35], neck linker (NL) docking induced by ATP binding to the microtubule-bound leading head (LH), pulls the trailing head

(TH) into the neighborhood of the target binding site that is 16 nm away from the initial binding site. In this model NL with $\sim$ 13 residues connecting the motor domain to the coiled coil is roughly analogous to lever arms in myosin motors [76]. In contrast, "Brownian ratchet" model [104] posits that ATP hydrolysis in the TH allows it to detach from microtubule to initiate diffusional search towards the target binding site. These two models are not mutually exclusive in the sense that elements of the two may be operative in determining kinesin motility.

Both models have experimental support. Experiments using single molecule FRET (Foster Resonance Energy Transfer) [37], and florescence anisotropy [40], show that the neck linker docks (power stroke) upon ATP binding to the LH. Does the motility of kinesin solely come from neck linker docking? A recent optical trap experiment [42] shows that a kinesin mutant, which lacks the cover strand (a major docking site of NL), can still walk processively but generates much less force. It can, therefore, be concluded that neck linker docking does contribute significantly to force generation. However, it also indicates that kinesin could walk by a Brownian ratchet mechanism in the absence of large external assisting or resisting load. Although diffusive motion of kinesin has not been reported in experiments, a number of observations support the Brownian ratchet model. First, the small size of even a fully stretched NL limits the potential physical displacement upon NL docking [68]. Second, the temperature dependence of stepping rates indicates an entropic nature of directional bias [104] that cannot be explained by the NL docking model alone.

As alluded to above, it has pointed out that these two mechanisms are not mutually exclusive [68]. However, an unresolved question of considerable importance

is what fraction of the kinesin step is associated with power stroke and diffusion, respectively [68]? If a large fraction of the step is associated with power stroke, we expect that the TH to move almost unidirectionally for 16 nm and the bidirectional diffusion could occur only within the neighborhood of the target binding site. An immediate consequence is that the movement of the TH (diffusion) should lag the motion of docking neck linker (power stroke). On the other hand, a majority of the 16 nm step is covered by diffusion of the TH, we expect that the motion of the TH is likely to be bidirectional and the extent of stochastic random walk of the TH should be large ($>$ 8 nm, half of the step size). It also implies that the TH should move faster than the docking LH-NL (power stroke).

In order to distinguish between the predictions of these two (extreme) models the motion of kinesin has to be tracked at sub-microsecond temporal resolution. Existing experiments recording the motion of kinesin head at lower temporal resolution show an apparently unidirectional motion and a fast step between the initial binding site (0 nm) and the target binding site (16 nm). The mechanism of TH motion is "hidden" in the jump time ($\sim$ 30 μs) between the waiting state (both heads are bound to the MT) of kinesin. Unless experiments can track the molecular events in the motor head on shorter time scales ($\sim$ (5-10) μs) one cannot unambiguously assess the interplay of power stroke and diffusive motion in facilitating the 8 nm step of kinesin. Given that a globural protein of the size of kinesin head with radius of gyration $R_g = 2$ nm, can diffuse 16 nm within $\tau \sim \frac{(16nm)^2}{2D} \sim \frac{(16nm)^2}{2\frac{k_B T}{6\pi\eta R_g}} \sim 4\mu$s in a medium as viscous as cytoplasm, microsecond or even sub-microsecond temporal resolution may be needed to capture the potential bidirectional motion of the TH

due to diffusion. However, due to difficulties in tracking kinesin experimentally at microsecond resolution [68], the importance of diffusivity of the kinesin step has been stressed but not been observed directly.

Molecular simulations are particularly suited to provide details of the stepping dynamics provided they are calibrated using experimental data. Such simulations, using coarse-grained (CG) and all atom models, have successfully investigated (i) the effects of intramolecular strain on nucleotide binding pocket of dimeric kinesin [102], (ii) the origin of substeps [89], (iii) the structural basis of neck linker docking [41], (iv) the mechanical properties of neck linker [110], and (v) the role of electrostatic interactions in kinesin-microtubule recognition [111]. Here, we use Brownian dynamics of a CG model of microtubule-kinesin (MT-Kin) complex to monitor the motion of kinesin during the 16 nm step at high temporal resolution [36]. We have previously established that our model for MT-Kin complex is sufficiently realistic to reproduce experimental time-dependent changes of the position of the cargo under a resistive force of 5 pN [81]. The present simulations are used to assess the motion of the TH and the LH neck linker separately at sub-microsecond resolution by generating several hundred trajectories. In particular, we clarify the interplay between the NL docking, the most discernible structural change during the stepping process, and tethered diffusion. Our simulations show that a substantial portion of the kinesin step occurs by a diffusive process. However, NL docking provides severe restrictions on the conformational space explored by the TH during the stochastic motion. Thus, a combination of NL docking and diffusive search for the target binding site (16 nm away) is needed for executing the movement of the TH predominantly towards the

+ end of the MT.

3.3 Results

In order to ensure that the simulations are realistic, we set out to reproduce two important experimentally measured mechanical properties of the kinesin motor, the stall force (F_s) [27, 81] and the force required to unbind TH from the MT (F_u) [112]. In our model F_s and F_u are determined by two major energy scales ϵ_h^{LH-NL} (the interaction between the NL and the LH) and ϵ_h^{TH-MT} (the interaction between the TH and the MT) [36]. Determination of the range of ϵ_h^{LH-NL} values that reproduces the measured F_s is needed for realistic modeling of NL-LH interaction, which largely determines the role of power stroke in facilitating the kinesin step. Obtaining the correct value of the unbinding force provides realistic modeling of TH-MT interaction, which affects not only the probability that Kin1 could take side steps but also determines the final stages of motor head-MT recognition [36].

3.3.1 Determination of ϵ_h^{LH-NL} value consistent with stall force F_s:

For each ϵ_h^{LH-NL}, we first performed a set control simulations in which no external force is applied to kinesin (black curve in Fig. 3.1b), and then another set of simulations in the presence of a resistive force of 7 pN (Fig. 3.1a and blue curve in Fig. 3.1b). For each set, we measured the probability of TH stepping forward to the target binding site (TBS) and backward to the initial binding site (IBS). In the optical trap experiments [27, 81], kinesin has equal probability of stepping forward

(P_f) and backward (P_b) at the stall force, F=F_s. Our simulations show that only for a narrow range of ϵ_h^{LH-NL}, $P_f \approx P_b$ at F = F_s = 7pN. At a resistive force ≈ 7pN with ϵ_h^{LH-NL} = 0.3 Kcal/mol, the probability that TH approaches the TBS at x_{TH} = 16 nm is small (Figs. 3.1b-3.1c). In the control simulation with F = 0, kinesin predominately moves forward (Figs. 3.1b-3.1c). In the rest of this paper we set ϵ_h^{LH-NL} = 0.3 Kcal/mol.

3.3.2 Calibrating the MT-TH interaction by reproducing unbinding force:

Experiments show that the unbinding force for monomeric kinesin varies from 3 pN to 9 pN depending on the nucleotide condition [112]. In order to obtain ϵ_h^{TH-MT}, we performed simulation by initially binding a single motor head to the MT (Fig. 3.1d), which mimics the experimental set up to obtain F_u, the force requires to dislodge the head from MT. By performing hundreds of simulations using various combination of ϵ_h^{TH-MT} and F (the external force), we were able to find the values of ϵ_h^{TH-MT} that allow kinesin to bind stably to microtubule in absence of external force (black curve in Fig. 3.1e-3.1f) but detaches at 3 pN corresponding to the weakly bound state (blue curve in Fig. 3.1e) or 9 pN corresponding to the strongly bound state (blue curve in Fig. 3.1f). Therefore, we can mimic both the weak and the strong binding states that kinesin is likely to experience during the 16 nm step. Because the exact timing and condition for ADP release, which strengthens the MT-kin interaction, is still unknown, here we perform simulations under both

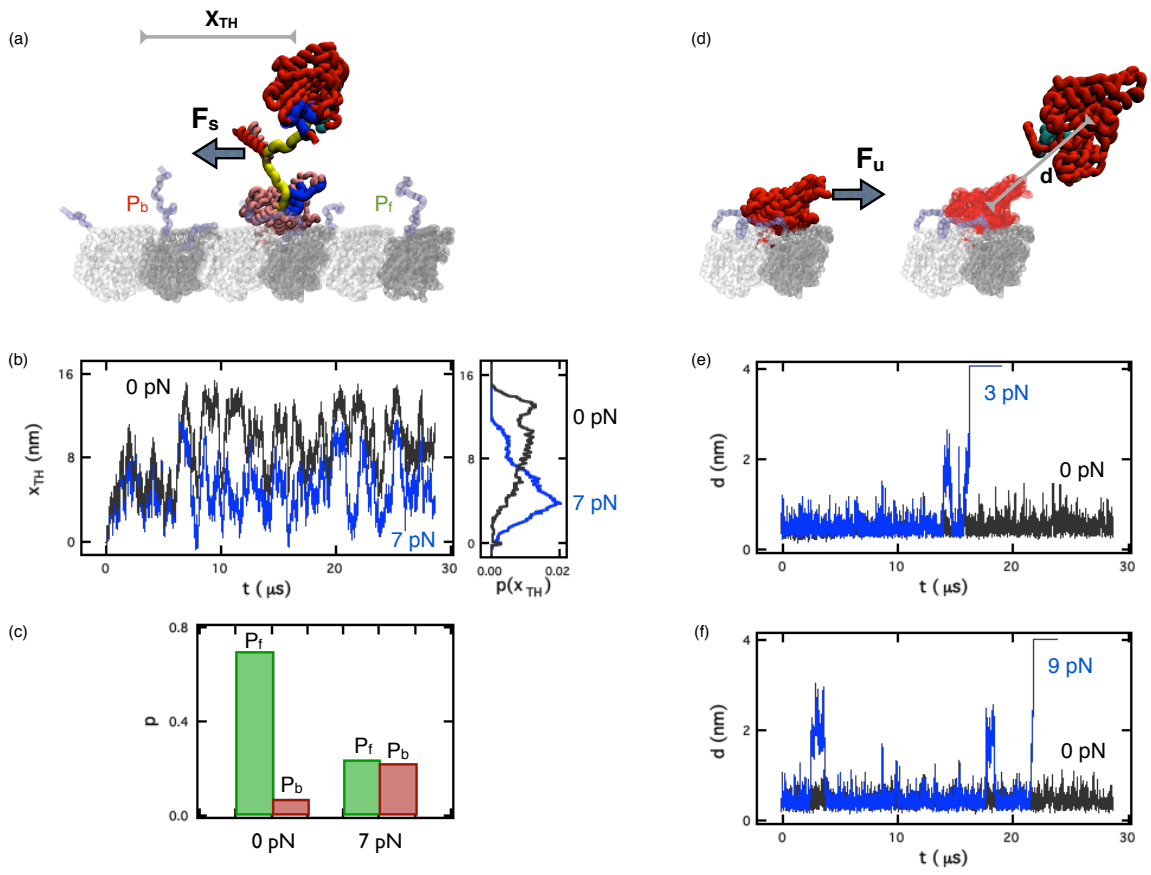

Figure 3.1: Calibrating key force field parameters using experimentally measured F_s and F_u

(a) Simulation setup to determine ϵ_h^{NL-LH} that reproduces F_s, the stall force. Force is applied to the T338 residue at the N-terminal of the coiled coil. (b) Displacement of (the center of mass of) the TH along the MT axis under an external resistive load of 0 (black) or 7 pN (blue) as a functional of time (left) and the associated distribution of x_{TH} (right), for a representative trajectory (ϵ_h^{NL-LH} = 0.30 Kcal/mol). (c) Probability of trailing head stepping forward (green) to the target binding site and backward (red) to the starting binding site under external resistive load of 0 pN and 7 pN based on a total of 200 trajectories with ϵ_h^{NL-LH} = 0.30 Kcal/mol. (d) Simulation setup to compute ϵ_h^{TH-MT} value that reproduce the experimentally measured F_u, the force needed to unbind a single motor head of kinesin from the microtubule. (e) Distance between monomeric kinesin head and microtubule under external force of 0 (black) or 3 pN (blue) as a function of time with ϵ_h^{TH-MT} = 0.16 Kcal/mol. Here $d = |\vec{R}_{com}(t) - \vec{R}_{com}(0)|$, where $\vec{R}_{com}(t)$ ($\vec{R}_{com}(0)$) is the center of mass coordinate of the kinesin head at $t > 0$ (t = 0). (f) Same as (e) except ϵ_h^{TH-MT} = 0.20 Kcal/mol.

weak and strong conditions.

3.3.3 Translation motion of the trailing head is diffusive:

Our simulations show that the 16 nm step of kinesin is diffusive, independent of our choice of ϵ_h^{TH-MT}. We observe large scale bidirectional diffusive motion of the TH throughout the 16 nm step, starting immediately after the TH detaches from the MT. Fig. 3.2, for example, shows that the center of mass of the TH fluctuates extensively (along the microtubule axis). Even when x_{TH} reaches 14 nm at ~ 7.5 μs, it decreases to ~ 4 nm at 10 μs (Fig. 3.2e). At a later time the TH enters the neighborhood of the TBS at $t \sim 17$ μs (see Fig. 3.2b and the arrow in Fig. 3.2g), but again retreats to a position behind the microtubule-bound leading head at $\sim$ 24 μs (Fig. 3.2e). Additional evidence for diffusion outside the neighborhood of the target binding site comes from the recording of d, the distance between the TH and the TBS, as a function of time (Figs. 3.2c and 3.2g). Fig. 3.2g shows that the TH stochastically searches for the TBS almost immediately after detachment from the MT. The trajectory in Fig. 3.2 is typical and we find similar behavior in all the other stepping trajectories as well. We surmise from the time-dependent changes in both x_{TH} and d_{TH} that the TH undergoes bidirectional diffusion not only within the neighborhood of the TBS, but also throughout the 16 nm step.

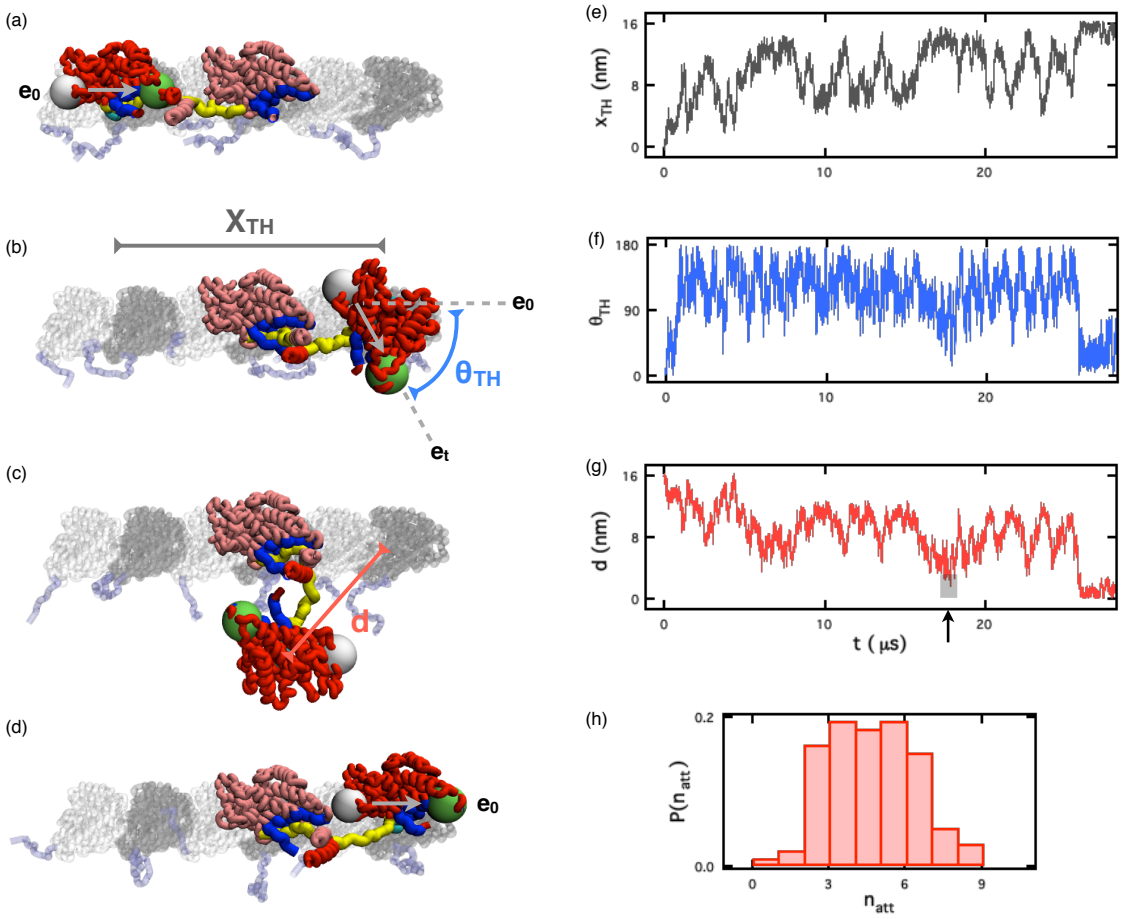

Figure 3.2: A 16 nm step of kinesin

(a-d) Four snapshots (at 0.0, 17.1, 19.3, and 27.8 μs) in a representative simulation trajectory of the 16 nm step of kinesin. The trailing head (TH) is in red, and the leading head (LH) is shown in pink. Yellow structure is the neck linker, and the docking site for the NL is in blue. α and β-tubulin are in silver and grey, respectively, and are augmented by ehooks (violet). The arrows in white ($\vec{e}_t$) indicates the orientation of the TH during the step (t $>$ 0). Here $\vec{e}_t$ is an unit vector pointing from residue V40 to residue N221 of the TH. The arrows in green ($\vec{e}_0$) indicates the initial orientation of the TH (t = 0). (e) Record of the translational motion of (the center of mass of) the TH along the microtubule axis during the 16 nm step. (f) Time-dependent changes in the rotational motion of the TH (with respect to its center of mass) during the same 16 nm step as (b). (g) The recording of d, the distance between the TH and the TBS, in a representative trajectory. One unsuccessful attempt TH made to bind to the target binding site is highlighted in black. (f) Distribution of n_{att}, the number of times the TH reaches the TBS with incorrect orientation (the number of unsuccessful attempts), based on 100 trajectories.

3.3.4 Trailing head undergoes isotropic rotational diffusion:

Time-dependent changes in x_{TH} and d_{TH} reveal only one facet of diffusive behavior of the TH during the kinesin step. The TH also undergoes rotational diffusion. We use θ_{TH} (see Fig. 3.2 for definition) to quantify the extent of rotation of the TH with respect to its center of mass. At t = 0, $\theta_{TH} \approx 0^\circ$ (Fig. 3.2f) meaning the TH is bound to the microtubule with the same orientation as observed in CryoEM image of kinesin-microtubule complex ($\vec{e}_0$ in Fig. 3.2a). We assume that stepping is complete only after the TH achieves the same orientation in the TBS ($\theta_{TH} \approx 0^\circ$). During the stepping process, θ_{TH} changes randomly between 0° and 180° (Fig. 3.2f). In the representative trajectory (Fig. 3.2), the TH is in the vicinity of the TBS at ~ 17.5 μs. However, at t ~ 17 μs the value of θ_{TH} is close to 70° (Fig. 3.2f), which implies one of the principal axes of the TH that is initially parallel to the MT axis when the TH was bound to the MT (see the white arrow in Fig. 3.2a), is almost perpendicular to the MT axis (see the white arrow in Fig. 3.2b). Because of the incorrect orientation, TH fails to bind to the target binding site at 17 μs and diffuses away from the TBS. Only at $t \sim 26$ μs does the TH achieve the correct orientation ($\sim 0^\circ$, see Fig. 3.2d).

The rotational motion of the TH is as important as translation, because kinesin head cannot bind to the microtubule and function with incorrect orientation ($\theta_{TH} \neq 0$). It has been shown using alanine scanning that all residues responsible for MT binding are located at one side of kinesin [105]. Furthermore, crystal structures of the intermediate states during Mg-ADP release and CryoEM structure of the MT-

Kin complex, suggest that activation of kinesin requires multiple specific contacts with the MT [92]. These results imply that stable binding between the TH and MT as well as the function of kinesin requires on specific orientation between the motor head and the MT. Our simulations show that a great deal of stochasticity is involved in achieving an interface between the TH and MT that satisfies the required orientation.

To further demonstrate the importance of rotational diffusion of the TH, we calculated n_{att} the number of times the TH retreats from the TBS due to incorrect orientation (Fig. 3.2h). In the trajectory shown in Fig. 3.2g, d, the distance between the TH and the TBS, transiently reaches ~ 0 nm one time at ~ 17 μs. However, it remains unbound ~ 20 μs because $\theta_{TH} \neq 0$. The distribution of the number of such failed attempts (Fig. 3.2h), based on 100 trajectories, shows that only in less than 5 % of trajectories the TH binds to the target binding site with the correct orientation at the instant when $d_{TH} \approx 0$. It is highly probable for the TH to try 3-6 times before it can finish the 16 nm step that satisfies both the distance ($d_{TH} \approx 0$) and orientational ($\theta_{TH} \sim 0^\circ$ criteria. Because of the diffusive nature of the motion, once the TH leaves the TBS, it could take the TH more than 10 μs to return to the TBS (between 17 μs and 25 μs in Fig. 3.2g for example). During this time interval, the TH may diffuse as far as 10-12 nm away from the target binding site, as illustrated in the dynamics after 17 μs in Fig. 3.2g. Thus, our results show that diffusional search for the TBS is more complicated involving a coupling between orientational and translational motion. Rotational diffusion of the TH is isotropic but the anisotropic translation motion is greatly (in the absence of applied resistive

force) biased towards the + end of the MT, which we show below is achieved by the NL docking to the LH.

3.3.5 Quantifying the fraction of the 16 nm step associated with power stroke and diffusion:

Our simulations allow us to quantify the fraction of kinesin step associated with the power stroke and that due to tethered diffusion. Although such a quantification has been reported for myosin motors [113], a similar parsing of the kinesin step remains undocumented. Here we use hundreds of trajectories, to measure the fraction associated with power stroke and diffusion. For each trajectory, we first identify the instant when power stroke associated with neck linker docking is complete (see the inset of Fig. 3.3). We calculated the extent of diffusion, x_{df}, by measuring the upper and lower values of x_{TH} that are reached after the completion of NL docking. For the trajectory in Fig. 3.3, x_{TH} fluctuates between 4 nm and 16 nm after NL docks, and therefore $x_{df} = 12$ nm. The reason x_{TH} does not fluctuate between 0 and 16 nm, is that once NL docks to the LH the limited length of the stretched TH neck linker prevents the TH from diffusing back to the initial binding site. The lower bound, 4 nm, corresponds to the fraction of 16 nm due to power stroke (x_{ps}) in this trajectory. The distribution of x_{ps}, based on 100 trajectories, shows that in general power stroke is responsible for 3-5 nm of the total 16 nm step (Fig. 3.3). Therefore, diffusion has to account for step length of $\sim$ (11-13) nm in most of the trajectories.

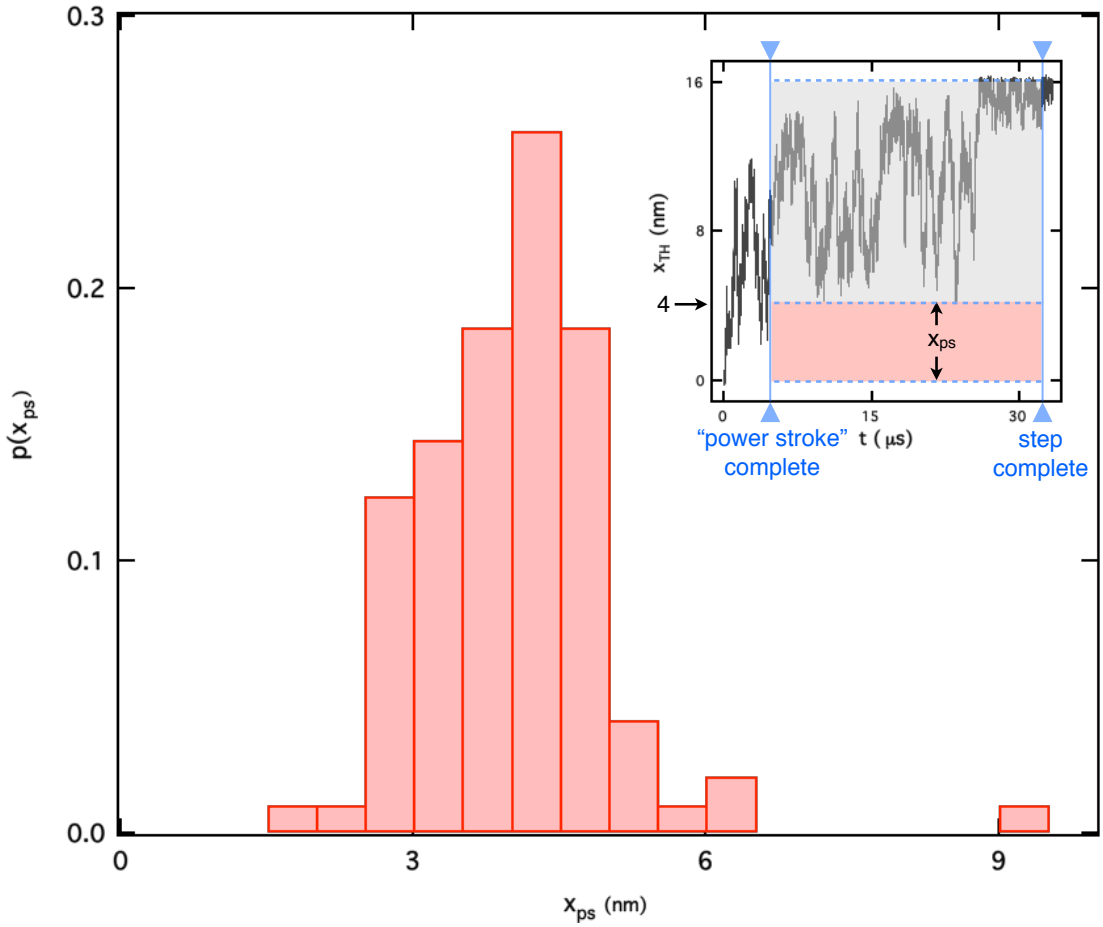

Figure 3.3: Fraction of 16 nm step associated with power stroke

Distribution of x_{ps}, the fraction of 16 nm associated with power stroke, based on 100 trajectories. The inset illustrates x_{ps} and shows the time variation in the translational motion of (the center of mass of) the TH along the MT axis in a representative trajectory. The first vertical line (solid blue) shows the instant neck linker docking (power stroke) is complete, after which the TH undergoes diffusive motion. The top and middle horizontal lines (dotted blue lines) indicate the extent of diffusional search after NL docking. The distance between the top and middle line corresponds to the fraction associated with diffusion, while the distance between the middle and bottom line corresponds to the fraction associated with power stroke.

3.3.6 Kinesin hops stochastically between multiple binding sites on the microtubule:

Does TH visit binding sites on neighboring protofilaments? This question is pertinent not only because the MT has multiple protofilaments but also because of our finding that nearly three quarters of the 16 nm step is covered by diffusion of the TH. Our simulations show that TH not only visits neighboring protofilaments but hops repeatedly between the binding sites on neighboring protofilaments and the TBS. For example, in a single trajectory (see the inset of Fig. 3.4) the TH first hops from the lower right binding site to the TBS, then diffuses from the TBS to the binding site below the site occupied by the LH. Subsequently, the TH revisits the lower right binding site, before finally being captured by the TBS. On an average, TH hops 2-3 times within 30 μs (Fig. 3.4). The average hopping rate, calculated based on hundreds of such events, is $\sim 10\ \mu s^{-1}$.

The results in Fig. 3.4 suggest that the TH may hop up to a few hundred times during a single kinesin step, depending on the affinity between ADP-bound TH and the MT. If the affinity is sufficient to trap the ADP-bound TH at a specific binding site, most likely the TBS, the TH may only hop between the geometrically allowed sites on the neighboring protofilaments 1-3 times within a step. On the other hand, if none of the accessible binding sites can trap the ADP-bound TH, hopping of the TH may persist until ADP release occurs. Release of ADP strengthens MT-kinesin interaction and hence would result in the cessation of the diffusional search and stochastic hopping. Given that the ADP release time ($\sim$ ms) is much slower than

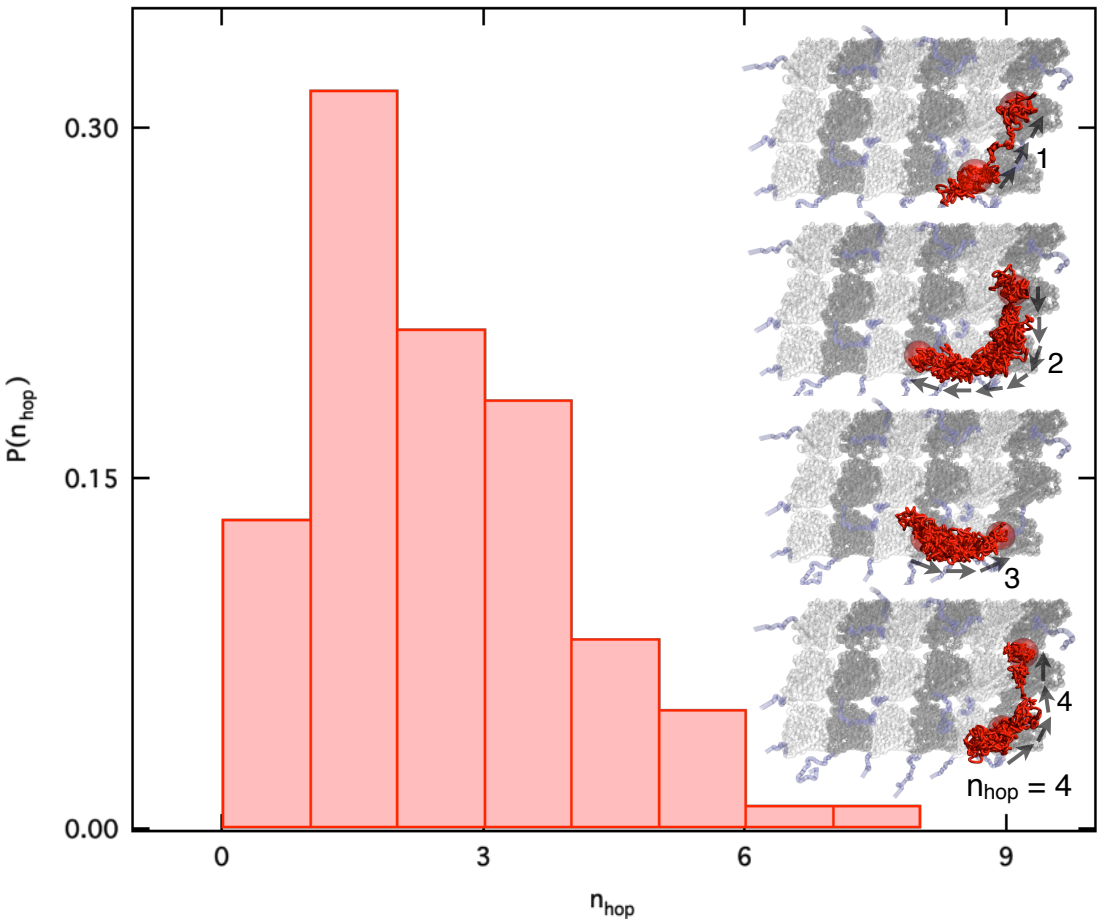

Figure 3.4: Stochastic hopping of TH between distinct binding sites

Distribution of n_{hop}, the number of hopping events within the first 30 μs, based on 100 trajectories. The insert shows four hopping events in a single trajectory.

the average hopping time between binding sites ($\sim$ 10 μs), it is likely that TH may hop hundreds of times within a single step.

3.3.7 NL docking constrains diffusion of the TH to minimize side steps:

So far we have provided four lines of evidence to support the diffusive nature of the kinesin step: high resolution recording of the translational and rotational motion of the TH (Figs. 3.2a-3.2g), multiple attempts to bind to the target binding site (Fig. 3.2h), large diffusion length (Fig. 3.3), and stochastic hopping between binding sites (Fig. 3.4). However, can diffusion alone lead to a site 16 nm away on the same protofilament as the TBS? To answer this question, we performed a mutation simulation, in which NL docking is energetically unfavorable ($\epsilon_h^{LH-NL} = 0$). We find that TH is more likely to visit binding sites on neighboring protofilaments besides the TBS, in the absence of NL docking (Fig. 3.5a). Just as in wild type simulations (where docking is favorable), we found that TH stochastically hops between the accessible binding sites due to the diffusive nature of head motion in the mutant simulations. However, in the absence of NL docking, the probability of TH hopping to neighboring side binding sites ($\sim$ 79 %) or the initial binding site ($\sim$ 20 %) is much larger than the probability of reaching the TBS ($\sim$ 1 %). On the other hand, in the wild type simulations, however, the probability of TH reaching the side, initial, and target binding site are 23 %, 7 %, and 70 %, respectively. Thus, despite the stochastic nature of tethered diffusion kinesin predominately reaches the

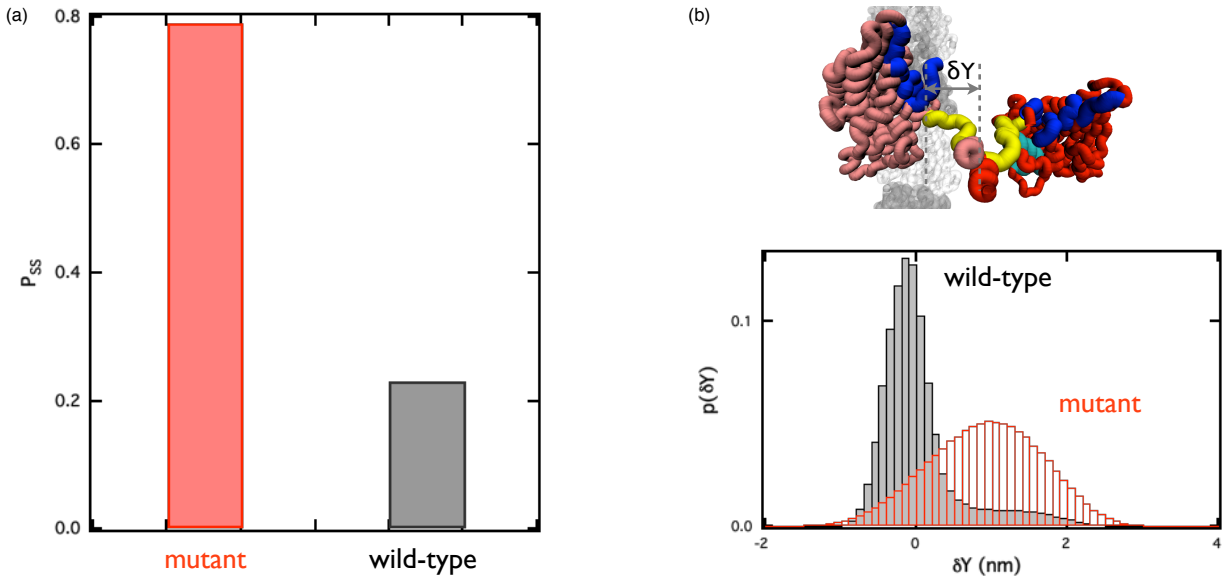

Figure 3.5: Neck linker docking decreases the probability of TH taking side steps

(a) Comparison of the probability of side steps in the mutant (docking is not energetically favorable) and wild type (docking is energetically favorable) simulations. Here $P_{ss} = \frac{\tau_{SBS}}{\tau_{TBS}+\tau_{SBS}+\tau_{IBS}}$. τ_{SBS} (τ_{TBS} and τ_{IBS}) is the average time the TH spent in the neighborhood of side binding sites on neighboring protofilaments (the TBS and the IBS) over 100 trajectories. The TH is consider to be in the neighborhood if d <4 nm (where d is defined in Eq. 2.3 in Analysis of trajectories (chapter 2.5)). (b) Distribution of sideway extension of LH-NL (δY) in the mutant and wild type simulation, where $\delta Y = (\vec{r}_{LH}^{T338} - \vec{r}_{LH}^{T326}) \cdot \hat{e}^{y}$.

TBS in the wild type simulations, which is largely due to the restriction imposed by NL docking.

Neck linker docking also decreases the probability of TH visiting side binding sites because it constrains the sideway extension of LH neck linker. Our previous study [36] showed that in order for the TH to take a side step, not only the TH neck linker but also the LH neck linker needs to extend sideways. If docking is not energetically favorable, LH neck linker can extend sideways freely (red bins in Fig. 3.5b). However, the interaction between catalytic core and LH neck linker would limit the sideway extension of LH neck linker if docking is energetically favorable (black bins in Fig. 3.5b). Therefore, although docking contributes only 3-5 nm out of 16 nm, it plays a key role in restricting the movement of kinesin along a single protofilament.

3.3.8 Comparing the motion of the docking neck linker and to the diffusing TH:

In oder to illustrate how NL docking constrains the diffusion of the TH and to establish the relation between NL docking, diffusion, and the motility of kinesin in general, we compared the displacement of the docking LH-NL and moving TH in a representative trajectory (Fig. 3.6a). More specifically, we show the motion of T338 (the red curve in Fig. 3.6b) at the boundary between coiled coil and LH-NL, which docks upon ATP binding. In the same figure, we also plot the motion of the center of mass of the TH (the black curve in Fig. 3.6b). Interestingly, the motion

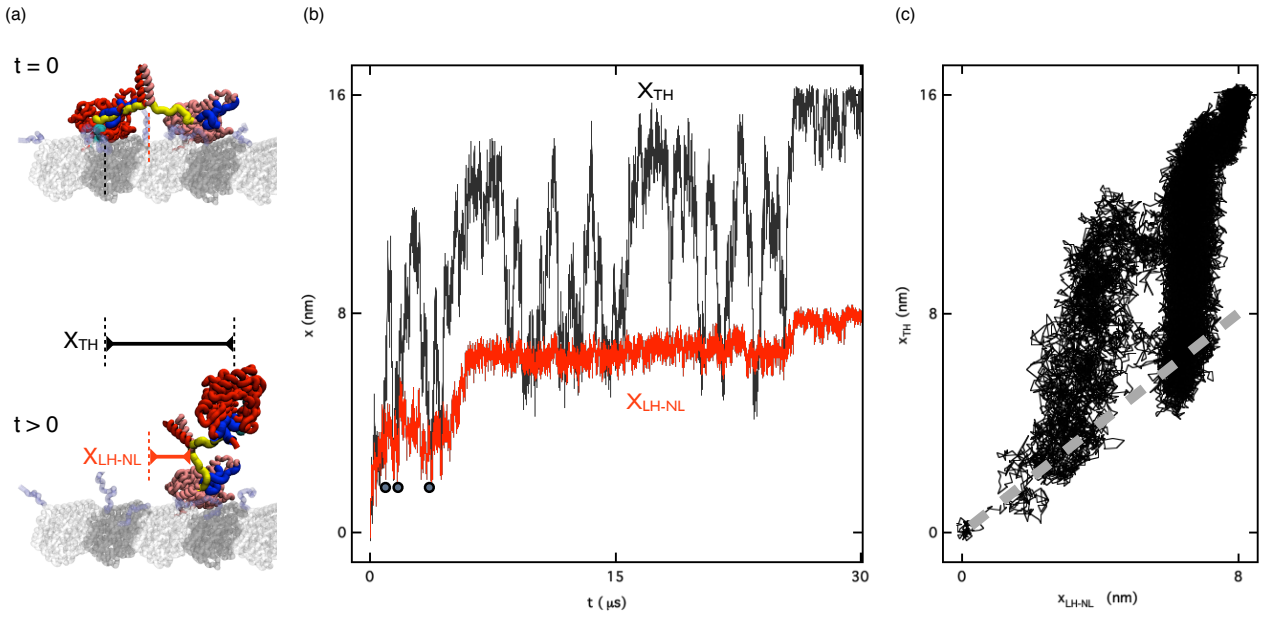

Figure 3.6: Comparing the motion of the LH-NL and the TH

(a) Two snapshots (one at t = 0 and the other at t > 0) in a representative simulation trajectory are shown to illustrate x_{TH} and x_{LH-NL}. Here $x_{LH-NL} = [x_{LH}^{T338}(t) - x_{LH}^{T338}(0)]$ and x_{TH} is the displacement of the center of mass of the TH along the MT axis as a function of time. (b) Record of the motion of the TH (black) an LH-NL (red) along the MT axis in a representative trajectory. (c) Plot of x_{TH} as a function of x_{LH-NL} in the same trajectory. Dotted line corresponds to $x_{TH} = x_{NL}$.

of the moving TH and the docking NL seems to be largely uncorrelated, except at the very early stages.

For example, at the instant when LH-NL reaches 5 nm (see the first grey dot in Fig. 3.6b), TH has already traveled a distance ≥ 10 nm, indicating that the diffusing TH is ahead of the docking LH-NL. Fig. 3.6b shows a plateau in the dynamics of T338 during which x_{T338} does not change, while x_{TH} undergoes large changes. As x_{T338} fluctuates around 5 nm (between the second and third dots in Fig. 3.6b), the x_{TH} diffuses between 4 and 12 nm. The only correlation between x_{T338} and x_{TH} seems to be that x_{T338} set a lower bound for x_{TH}, meaning x_{TH} rarely drops below the value of x_{T338} by more than ~ 1 nm.

The lack of correlation between the time-dependent changes in x_{TH} and x_{T338} is more apparent in a plot x_{TH} as a function of x_{T338} (Fig. 3.6c). The dotted line corresponds to $x_{TH} = x_{T338}$. Any data point above (below) the dotted line indicates that TH is ahead of (behind) the docking LH-NL. We find that TH follows LH-NL up to 3 nm, after which the TH is predominately ahead of the LH-NL. At the end of the step, the TH moves ~ 16 nm while LH-NL moves only ~ 8 nm. During the step, x_{TH} occasionally drops below x_{NL}, but by an amount that is less than ~ 1 nm. Thus, given the TH is ahead of the docking NL during the major duration of the step, it is inaccurate to envision that TH is pulled by NL docking towards the + end of the MT. The TH reaches the TBS at the + end through diffusion, with NL docking providing the needed restriction and guidance for the TH to reach the TBS.

3.4 Methods

3.4.1 Self-Organized Polymer (SOP) model for MT-kinesin complex:

The large size of the Mt-Kin complex, and the long timescale of kinesin step (> 10 μs) make it necessary to use coarse-grained models, which have been used with great success in a large number of problems in biology [114]. We used the self-organized polymer (SOP) model [98, 115, 116] for the MT-Kin complex. The methods used to construct the structure of the MT-kin complex is described in details in the Supplementary Information in [36]. As in our previous study, we include three microtubule protofilaments, two motor heads, a coiled coil (length $\approx$ 30 nm) and a 500 nm spherical cargo. We model each residue in the system using one interaction center located at the α-carbon position. This level of coarse graining allows us to integrate sequence specific interactions observed in crystal structures and CryoEM images at reasonable spatial resolution (~ 4 $\mathring{A}$). In addition, it is only through the use of CG models that simulations of such a large system (containing several thousands residues) can reach relevant time scales (ten of μs or longer) for observing stepping dynamics. For example, we simulated the energetically favorable but dynamically reversible neck linker docking induced by ATP docking, based on crystallographically observed contacts between residues in neck linker and motor head. We modeled the nucleotide dependent MT-Kin interactions based on residue wise contacts in the CryoEM image of the kinesin-microtubule complex. In addition the simplicity of the CG model allows us to generate several hundred trajectories to fully explore the range of parameters that govern the events in the motility of

kinesin.

3.4.2 Brownian dynamics simulation with hydrodynamic interactions:

We simulated the MT-Kin complex consisting of $\sim$ 9,000 residues by assuming that the dynamics of the system can be described by the Langevin equation in the over damped limit. The equations of motion for the motor domain of the TH (residues 2-326), which includes hydrodynamic interactions (HI), are

$$\vec{r_i}(t+h) = \vec{r_i}(t) + \sum_{j=1}^{N^{TH}} \frac{D_{ij}h}{k_B T}(-\frac{\partial H(r_i|X)}{\partial \vec{r_j}}) + \vec{\Gamma}_i(t) \tag{3.1}$$

where D_{ij} is the diffusion tensor including HI, $r_i(t)$ is the position of the i^{th} interaction center at time t, $H(r_i|X)$ is the SOP energy function (see Eq. B.1 in Appendix B), and X refers to the state of the motor domains. We used the Rotne-Prager-Yamakawa form for the 3 $\times$ 3 diffusion tensor for D_{ij} whose ij^{th} element is given by,

$$\begin{aligned}
D_{ii} &= \frac{k_B T}{6\pi\eta a} I \\
D_{ij} &= \frac{k_B T}{8\pi\eta r_{ij}}[(1+\frac{2a^2}{3r_{ij}^2})I + (1-\frac{2a^2}{r_{ij}^2})\frac{\vec{r}_{ij}\vec{r}_{ij}}{r_{ij}^2}] \text{ if } r_{ij} \geq 2a \\
D_{ij} &= \frac{k_B T}{8\pi\eta r_{ij}}[\frac{r_{ij}}{2a}(\frac{8}{3}-\frac{3r_{ij}}{4a})I + \frac{r_{ij}}{4a}\frac{\vec{r}_{ij}\vec{r}_{ij}}{r_{ij}^2}] \text{ if } r_{ij} < 2a
\end{aligned} \tag{3.2}$$

where k_B is the Boltzmann constant, and T (=290 K) is the temperature, and η (=0.003 Pa·s) is roughly the viscosity of the cytoplasm [117].

Because the dynamics during the stepping process predominantly involves movement of the motor domain, we only included HI for the dynamics of the TH. For the rest of the system (cargo, the coiled coil, and the motor domain of the LH),

we integrated the Langevin equations using

$$\vec{r_i}(t+h) = \vec{r_i}(t) + \frac{h}{6\pi\eta a}(-\frac{\partial H(r_i|X)}{\partial \vec{r_i}}) + \vec{\Gamma}_i(t). \tag{3.3}$$

where $\vec{\Gamma}_i$, the random force in Eqs. 3.1 and 3.3 satisfies $< \vec{\Gamma}_i(t) >= 0$ and $< \vec{\Gamma}_i(t)\vec{\Gamma}_j(t') >= 6D_{ij}h\delta_{tt'}$ for residues in the TH motor domain. For all other interaction sites, the Gaussian noise spectrum satisfies $< \vec{\Gamma}_i(t)\vec{\Gamma}_j(t') >= 6\frac{k_BT}{6\pi\eta R_\alpha}h\delta_{tt'}\delta_{ij}$, where R_α is either a or R_{cargo}. The radius, a, of each residue is 0.19 nm, and the integration step h is 0.12 ps. Because of the simplicity of the model, we could generate hundreds of trajectories (each 30 μs or longer), and obtain substantial statistics to describe the details of the kinesin step.

3.4.3 Two important energy scales for kinesin motility:

In our previous study [36] we showed that the motion of kinesin during the 16 nm step is determined by two energy scales. The first one, ϵ_h^{NL-LH}, is associated with neck linker docking, and the other, ϵ_h^{TH-MT}, describes the interactions between the TH and the MT. Although experiments using different techniques have reported varying estimates of the energy associated with ATP-induced neck linker docking, both the stall force F_s and force F_u required to unbind the motor domain from the MT F_u are similar in a majority of studies. Therefore, we performed simulations by varying ϵ_h^{NL-LH} and ϵ_h^{TH-MT} to obtain experimentally measured F_s and F_u values.

First, we applied force ($F = 0$, 3, 6 and 9pN) on a single kinesin head attached to the MT, and measured the probability of detachment of the initially bound state. The force is applied to residue T338 at the C-terminal of the NL, towards either the

(+) or the (-) end of the MT. We performed 10 simulations for each set of ϵ_h^{TH-MT} and F, and calculated, p_d, the probability of detachment within 30 μs. We consider that the TH detached if $d = |\vec{r}_{com}^{TH}(t) - \vec{r}_{com}^{TH}(0)| > 4$ nm where $\vec{r}_{com}^{TH}(0)$ is the center of mass coordinate of the TH when the motor head is bound to the MT at t = 0, and $\vec{r}_{com}^{TH}(t)$ is the same coordinate at t > 0. The value of $\epsilon_h^{TH-MT} \approx 0.16$ (0.20) Kcal/mol, giving zero p_d at 0 pN but non-zero p_d at 3 pN (and 6-9 pN), is chosen to model the weak (and strong) affinity state between kinesin and microtubule.

Next, we applied experimentally measured stall force on a walking kinesin dimer, and calculated the probability of the TH stepping forward to the target binding site and backward to the initial binding site. A resistive force of 7 pN is applied on the N-terminal of the coiled coil toward the (-) end of MT. We performed a few sets of simulations with the same ϵ_h^{TH-MT} but different ϵ_h^{NL-LH}, with each set containing 100 trajectories. We define the probability of stepping forward (p_f) and backward (p_b) as $p_f = \frac{\tau_{TBS}}{\tau_{TBS}+\tau_{IBS}+\tau_{SBS}}$ and $p_b = \frac{\tau_{IBS}}{\tau_{TBS}+\tau_{IBS}+\tau_{SBS}}$ where τ_{TBS}, τ_{IBS} and τ_{SBS} are the average times the TH spends in the neighborhood of the target, initial, and side binding sites, respectively. The TH is considered to be in the neighborhood if $d < 4$ nm. We chose the ϵ_h^{LH-NL} that yields approximately equal p_f and p_b under a resistive force of 7 pN, to be the interaction strength of ATP-induced neck linker docking.

3.4.4 Simulating 16 nm step of kinesin:

After obtaining values of ϵ_h^{TH-MT} and ϵ_h^{NL-LH} that reproduce F_u and F_s values, we simulated hundreds of kinesin steps using Brownian dynamics simulation with hydrodynamic interactions (Eqs. 3.1-3.3). We performed two sets of simulation with $\epsilon_h^{TH-MT} = 0.16$ and 0.20 Kcal/mol, corresponding to unbinding force of 3 pN and 9 pN. Most of the representative trajectories shown in the main text are generated from simulations with $\epsilon_h^{TH-MT} = 0.20$ Kcal/mol, because we did not observe the completion of 16 nm steps for $\epsilon_h^{TH-MT} = 0.16$ Kcal/mol within our simulation time window (30 μs). However, we did confirm that the key results such as the fraction associated with power stroke and diffusion, the hopping rate, and the probability of side steps change less than 10 % when we decrease ϵ_h^{TH-MT} from 0.20 to 0.16 Kcal/mol. Given that the duration of diffusional search with $\epsilon_h^{TH-MT} = 0.20$ Kcal/mol in each of 100 trajectories generated is about an order of magnitude longer than the first passage time for reaching 8 nm, the distributions of key properties in the diffusional search such as hopping rate are unlikely to change significantly by further increasing the simulation time.

3.5 Conclusion:

We have used realistic (our model with two key energy scales reproduce the experimentally measured values of the stall force and the force required to unbind the motor head from the microtubule) simulations to quantify the extent to which purely diffusive motion of the TH contributes to the 16 nm step. Surprisingly, we

find that nearly three quarters of the step involves almost random search of the target binding site by the TH. However, in order to execute the 16 nm step and stay on the same protofilament of the MT ATP-driven docking of the NL (sometimes thought of as a power stroke in the context of kinesin motility) is essential. Mutant simulations show that in the absence of NL docking the probability of taking a side step step is greatly increased and the chances of the TH reaching the target binding site with stable MT-Kin interaction is greatly diminished. Our simulations, which for the first time quantified the contributions power stroke and diffusion make to the 16 nm step, show that an interplay between both the events are crucial in kinesin successfully taking the 16 nm step.

One of the remarkable findings in our work is that the TH hops stochastically a large number of times between geometrically accessible alternative MT binding sites before stably locating the site that is 16 nm away on the same protofilament. Single molecule experiments [118, 119] support such a possibility, thus adding credence to our simulation results. By measuring the orientation of TH using fluorescence anisotropy [119] and the distance between the two heads using FRET [118], two groups independently showed that ADP-bound TH does not bind to the MT, and is mobile when the other head (in APO state or no nucleotide state) is strongly bound to the MT. These results indicate that the weak interaction between ADP-bound TH and the MT is not sufficient to support a two-head bound state. Our simulations show that although monomeric ADP-bound head stays bound to the MT resisting external forces up to 3 pN, the ADP-bound head in a kinesin dimer cannot bind stably to any site on the MT when the other head (in ATP-bound state) is strongly

bound to the MT. Thus, during a single 16 nm step the TH may hop stochastically between side binding sites and target binding site few times to few hundreds times until ADP is released.

The observed stochastic hopping is not unrelated to the timing of ADP release from the TH. Indeed, it can be argued that minimizing the probability that kinesin takes side steps could be regulated by properly timed ADP release from the TH. It is only after ADP is released from the motor head can the TH bind stably to a binding site on the MT. Therefore, side steps could be prevented if ADP release occurs only when TH is in the vicinity of the TBS. Experiments using optical trap showed that kinesin-ADP affinity is lower when NL points towards the - end of the MT [69], which implies that the TH is more likely to release the bound ADP at TBS than IBS, because TH-NL would points towards the - end of the MT as the TH approaches the TBS. However, the observation that the probability of side steps is larger than 50 % for a kinesin mutant with extended NL [82] suggests that TH could release ADP at accessible binding sites other than the TBS.

Based on these experimental observations and our simulations, we posit that NL docking is likely to play a key role in decreasing the side steps. Geometry of the MT determines that a few binding sites on neighboring protofilaments are closer to the site occupied by the LH than the TBS. As a result, if the diffusion of the TH is not constrained, TH would visit those binding sites on neighboring protofilaments much more often than the TBS. It is possible that side steps can still be prevented if TH in the wild type kinesin with neck linker of normal length is prohibited from releasing ADP at neighboring protofilaments, which does not seem

physical given that all the sites are equivalent. However, a simpler and perhaps a physically more transparent way to decrease the probability that kinesin takes side steps is to prevent the TH from visiting binding sites on neighboring protofilaments through NL docking. It is likely that the length of the NL has evolved so that it constrains the diffusion length of the TH so that kinesin completes the 16 nm step with substantial probability.

Chapter 4

Structural basis of controlling ADP release from kinesin

4.1 Summary

It is surprising that a microtubule accelerates ADP release from a kinesin by several orders of magnitude [19, 120], given that the nucleotide binding pocket of the kinesin is ∼1.5 nm away from the microtubule binding surface. Therefore, microtubules must trigger ADP release by an allosteric mechanism. However, due to the lack of crystal structure of the kinesin-microtubule complex, the allosteric network responsible for microtubule-accelerated ADP release has not been identified. Moreover, a recent study [69] suggested that the ADP release from kinesin can be assisted (inhibited) by backward (forward) strain within the neck linker, which is even further (>2.3 nm) away from the nucleotide binding pocket. The allosteric network responsible for strain-dependent ADP release is also mysterious. Using several μs all-atom simulations, we have identified a surprisingly simple allosteric network that triggers partial ADP release from the kinesin within 1 μs after microtubule binding. Interestingly, the same allosteric network is also sensitive to strain within neck linker. It triggers (inhibits) partial ADP release in response to the backward (forward) strain. In addition, the allosteric signaling within this network can be blocked by a single mutation on kinesin, which was previously shown [71] to impair the microtubule-accelerated ADP release. Thus, our simulations are consistent with

four sets of previous experiments [19, 69, 71, 120]. In conclusion, the simulations reveal the allosteric network that controls ADP release from kinesin.

4.2 Introduction

Kinesin is an ATP-dependent cellular transporter that ferries cargo towards the plus-end of the microtubule [72, 73]. Kinesin contains two motor heads, which walk along the microtubule in a hand-over-hand manner [43]. This means that during a single step, the ADP-bound trailing head detaches from the microtubule, passes the microtubule-bound leading head, and reaches the target binding site on the microtubule 16 nm away. However, the trailing head cannot bind stably to the binding site until the ADP is released. This is because when a motor head is bound to ADP, it has weak affinity to the microtubule [112]. Once the ADP release occurs, the motor head in the APO-state is poised to lock onto the target binding site. In addition, the kinesin is ready to accept a new ATP molecule and begin a new step [35, 107, 121]. Therefore, ADP release is critical for kinesin to complete a step and start a new one.

Many factors can affect the rate of ADP release from kinesin. For example, microtubules accelerate the process of nucleotide release by several orders of magnitude (from minutes to milliseconds) [19, 120]. This finding indicates that the microtubule plays an active role in the function of the kinesin [36, 88, 93, 111, 122] besides serving as a track for motility. The second known factor is mutation. A single, N-to-K switch at residue 255 of human conventional kinesin, completely im-

pairs the microtubule-accelerated ADP release [71]. ADP release from the kinesin can also be affected by strain [69]. A recent study showed that strain applied to a microtubule-bound kinesin towards the plus-end (minus-end) of microtubule increases (decreases) the kinesin-ADP affinity [69]. However, despite mounting lines of biochemical evidence, the structural basis of ADP release from kinesin remains unclear.

Can we learn from other nucleotide-binding proteins, such as the G-protein, where the mechanism of nucleotide release is relatively well understood [123]? Like kinesin, G-protein also has a very low rate of intrinsic GDP release. GDP release from G-protein is triggered *in vivo* by specific factors called guanine-exchange-factors (GEF). The crystal structures of the G-protein-GEF complex showed the intrusion of the GEF into the nucleotide binding pocket of the G-protein. Therefore, it is very likely that GEF triggers GDP release from G-protein by directly expelling the bound GDP through steric interactions.

However, such a steric mechanism is unlikely to work for kinesin, because the nucleotide binding pocket of kinesin is far ($\sim$1.5 nm) from the microtubule binding surface [29, 88, 105, 122]. Therefore, microtubule must accelerate ADP release from the kinesin by an allosteric mechanism. Similarly, strain is also likely to regulate ADP release through an allosteric network within the kinesin. It is because the neck linker, to which strain is applied [69], is more than 2.3 nm from the nucleotide binding pocket of the kinesin. Identifying the allosteric network controlling ADP release from kinesin is important for our understanding of nucleotide release from proteins in general. ADP release from many other ATPases, such as myosin [77, 99,

124] and GroEL [98, 125], is also triggered allosterically by specific factors.

Two types of structural studies predict certain elements of the allosteric network, responsible for controlling ADP release from the kinesin. The first type, focused on the nucleotide-kinesin-microtubule complex, is based on a Cryo-electron microscopy study, which suggested that switch-I region moves towards the nucleotide binding P-loop (labelled in Figs. 1.4 and 4.3) during and after ADP release [122]. Another study based on EPR spectroscopy indicates that the nucleotide binding pocket is closed upon microtubule binding [126]. The second type studied the structure of kinesin in the absence of the microtubule. Crystal structures of kinesin [92, 127] in combination with mutagenesis studies [71] and biochemical assays [71, 92, 127], have revealed several important interactions surrounding the nucleotide binding pocket, such as the R-E salt bridge. However, due to the lack of the crystal structure of the kinesin-microtubule complex and the difficulty of probing strain-induced conformational changes, many questions remain unanswered. (i) What elements in the allosteric network are responsible for sensing the microtubule? (ii) What structural elements are sensitive to the applied strain? (iii) What elements trigger ADP release? (iv) How do elements responsible for sensing the microtubule and strain, communicate with elements controlling ADP release? (v) How do mutations disrupt the needed allosteric communication for ADP release?

To answer these questions, we performed five different sets of microsecond all atom molecular dynamics simulations in explicit water (see Appendix C for details). We simulated (1) ADP-kinesin complex, (2) ADP-kinesin-microtubule complex, (3) ADP-kinesin mutant-microtubule complex, (4) ADP-kinesin-microtubule complex

under forward strain, and (5) ADP-kinesin-microtubule complex under backward strain. These simulations were performed on Anton supercomputers [128], which can be used to generate multiple μs long trajectories in atomic details. These powerful computers have been used to provide structural details for many important experimentally confirmed discoveries [129, 130] due to the ability to produce microsecond simulations on large systems such as ion channels [131] and G-protein coupled receptors [130]. We observed that upon microtubule binding, the adenine base, the ribose, and the α-phosphate of the ADP are completely released from the nucleotide binding pocket of the kinesin. More importantly, such partial ADP release can be inhibited by the previously reported mutation. It can also be inhibited by forward strain applied to the neck linker (towards the +end of the microtubule). Therefore, our simulation results are consistent with earlier experiments [19, 69, 71, 120], and provide a structural interpretation of the ADP release mechanism. Most importantly, we discovered a surprisingly simple allosteric network that triggers partial ADP release upon microtubule binding. The network model explains the inhibition of nucleotide release in response to mutation or forward strain, thus providing an unified explanation of a number of experimental facts.

4.3 Results

4.3.1 ADP binds stably to kinesin in the absence of microtubule.

To study the effect of microtubule binding on kinesin-ADP affinity, we first performed a set of control simulations of the ADP-kinesin complex in the absence of

the microtubule. We found that although the adenine base shows transient deviation from the conformation in the crystal structure [132], in general ADP binds stably to the nucleotide binding pocket of kinesin. Fig. 4.1a shows three representative ADP conformations captured in our simulations. The difference between the snapshot in green (crystal structure) and yellow (simulation) indicates the extent of the deviation caused by the rotation of the adenine base.

Given that the rest of ADP, in particular the β-phosphate, is stably bound to the nucleotide binding pocket throughout the duration of the simulations, we quantified the conformational change of the nucleotide by measuring the rotation of the adenine with respect to the β-phosphate (Fig. 4.1a). The record of the rotational angle θ(t), as a function of time, shows that initially, the adenine rotates by $\sim$ 45 degrees (Fig. 4.1b), and therefore breaks the stacking interaction with H93 of the P-loop, which is present in the crystal structure of ADP-bound kinesin [132]. However, the transient deviation of the adenine base is still in the vicinity of the nucleotide binding pocket (Fig. 4.1a). It is recaptured by H93 at $\sim$ 0.3 us and adapts the conformation observed in the crystal structure, as indicated by a drop of θ to $\sim$ 0 degrees (Fig. 4.1b). The fluctuation in θ(t) around the value in the crystal structure is not large enough to eject ADP.

The distribution of the rotational angle θ shows two peaks (Fig. 4.1b). The smaller peak at $\sim$ 45 degrees corresponds to a population of slightly deviated ADP conformations (the snapshot in yellow in Fig. 4.1a). The larger peak near $\sim$ 0 degrees corresponds to the ADP conformation observed in the crystal structure (the snapshot in blue in Fig. 4.1a). Therefore, we conclude that in the absence of the

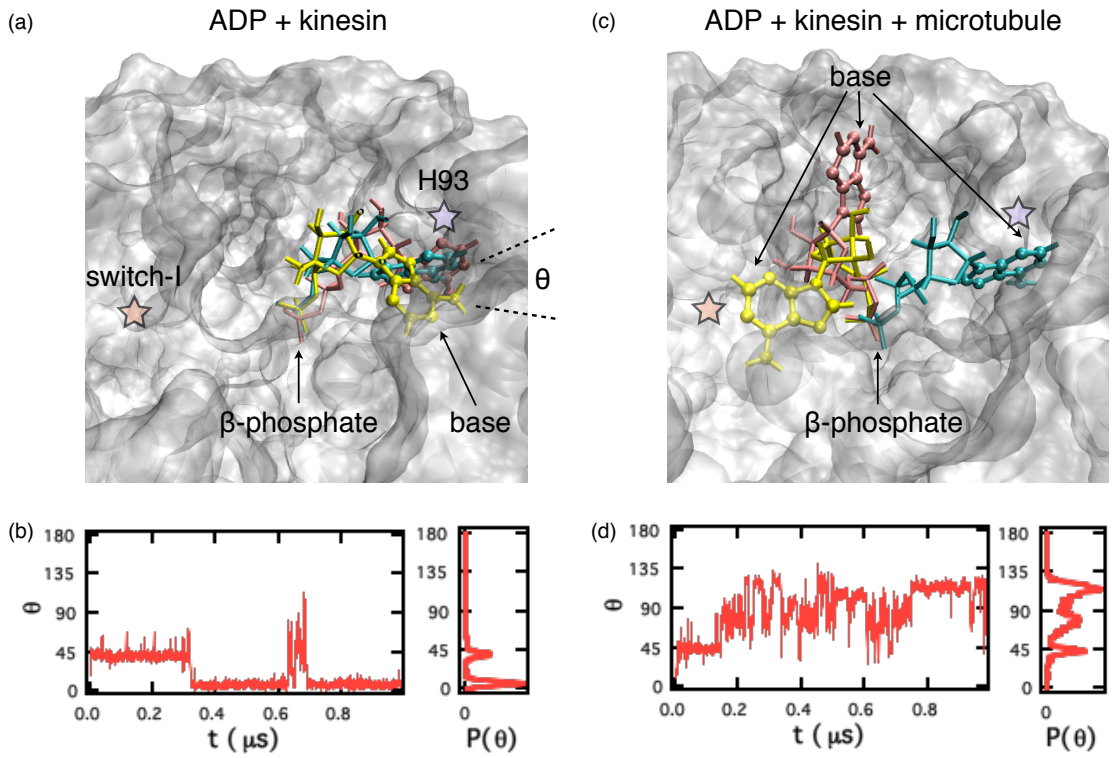

Figure 4.1: ADP is partially released from kinesin upon microtubule binding

(a) Three representative ADP conformations (in yellow, green, and red) observed in representative 1μs all atom molecular dynamics simulations of the ADP-kinesin complex. The kinesin is shown in white. The approximate location of switch-I and H93 of the P-loop are indicated by the pink and purple stars, respectively. (b) The time-dependent record and the distribution of θ, quantifying the rotation of the adenine base of the ADP with respect to the β-phosphate. Here $\theta = cos^{-1}\{\frac{[\vec{r}_{ad}(t)-\vec{r}_{bp}(t)]\cdot[\vec{r}^{c}_{ad}-\vec{r}^{c}_{bp}]}{|\vec{r}_{ad}(t)-\vec{r}_{bp}(t)||\vec{r}^{c}_{ad}-\vec{r}^{c}_{bp}|}\}$, where $\vec{r}_{ad}(t)$ ($\vec{r}_{ph}(t)$) is the center of mass coordinate of the adenine base (β-phosphate) in the simulation, and $\vec{r}^{c}_{ad}$ ($\vec{r}^{c}_{ph}$) is the corresponding coordinate in the crystal structure of ADP-kinesin complex (1MKJ.pdb). (c) Same as (a) except for the simulations of the ADP-kinesin-microtubule complex. For the purpose of clarity, the microtubule in not shown here. (d) Same as (b) except for the simulations of the ADP-kinesin-microtubule complex.

microtubule ADP binds stably to the nucleotide binding pocket of the kinesin.

4.3.2 ADP is partially released upon microtubule binding.

In the presence of the microtubule however, the entire ADP molecule except the β-phosphate, is completely dislodged from the nucleotide binding pocket (Fig. 4.1c). During the simulation, the adenine ring of the ADP has moved more than 1.5 nm, from the initial location near H93 on right hand side of kinesin (the purple star in Fig. 4.1c), to the vicinity of switch-I on the left hand side (the pink star in Fig. 4.1c).

The large conformational change of ADP upon microtubule binding is also reflected by the increase of the rotational angle θ to up to 145 degrees (Fig. 4.1d). The record of θ(t) as a function of time shows that the adenine ring first rotates by 45 degrees, indicating a small deviation from the crystal structure. Then, instead of dropping to 0 degrees as occurred in the absence of the microtubule, θ(t) continues to increase and then fluctuates widely between 45 and 135 degrees. This result suggests that the adenine base, the ribose, and α-phosphate have been completely released from the nucleotide binding pocket.

The distribution P(θ) of θ in the presence of the microtubule (Fig. 4.1d), is very different from that observed in the absence of the microtubule (Fig. 4.1b). In the presence of the microtubule, P(θ) has three peaks. The major peak near $\sim$120 degrees corresponds to the ADP conformation in yellow (Fig. 4.1c). Here only the β-phosphate remains inside the nucleotide binding pocket. The adenine base, the

ribose, and the α-phosphate are released from the nucleotide binding pocket.

To test if the result is robust, we calculated P(θ) in a second independent simulation trajectory of the ADP-kinesin-microtubule complex. The distribution again shows a dominate peak near 120 degrees, indicating partial ADP release (See Fig. D.1 in Appendix D). Therefore, while the ADP binds stably to the kinesin in the absence of the microtubule, in the presence of the microtubule most parts of ADP (the adenine, ribose, and α-phosphate, but not the β-phosphate) are released from the nucleotide binding pocket in our microsecond simulations.

Comparison of the results obtained in these simulations suggests that the allosteric network within kinesin responds to microtubule binding. Within a microsecond, the allosteric network has not only sensed microtubule binding, but triggered a conformational change that leads to partial ADP release.

4.3.3 Simulation results explain experimental observations

If the conformational change observed in our microsecond simulations is crucial to the release of the entire ADP molecule at a much slower timescale [19, 120], we expect that the conformational change and the partial ADP release to be inhibited by the previously reported N-to-K mutation [71]. Therefore, we performed a third set of simulations, where we introduced a single mutation (N255K) on the kinesin. The N-to-K mutation has been shown to impair the microtubule-accelerated ADP release from different members of the kinesin family [71].

In the simulations of the ADP-kinesin(N255K)-microtubule complex, we ob-

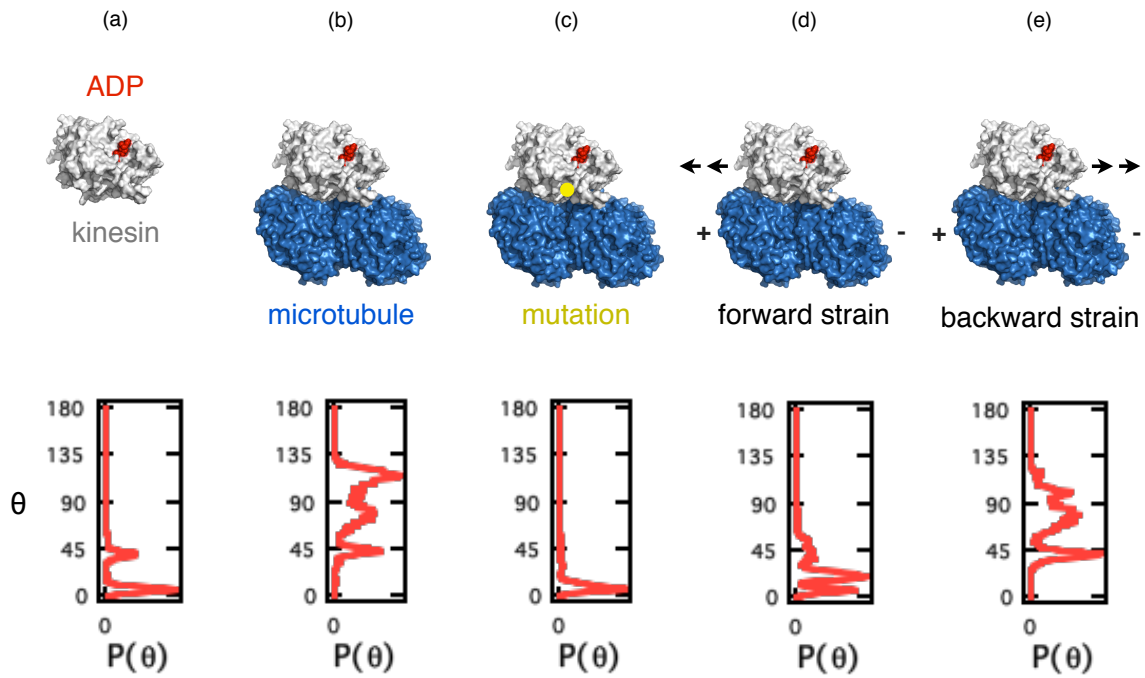

Figure 4.2: The summary of results of five sets of molecular dynamics simulations

(a) The simulation system (ADP-kinesin complex) and the corresponding distribution of θ quantifying the rotation of the adenine base of the ADP with respect to the β-phosphate in a representative trajectory. (b) The simulation system (ADP-kinesin-microtubule complex) and the corresponding P(θ). (c) The simulation system (ADP-kinesin[N255K]-microtubule complex) and the corresponding P(θ). The yellow dot indicates the approximate location of the mutation N255K. (d) The simulation system (ADP-kinesin-microtubule complex under forward strain) and the corresponding P(θ). The arrow indicates the direction of the strain. (e) The simulation system (ADP-kinesin-microtubule complex under backward strain) and the corresponding P(θ). The arrow indicates the direction of the strain.

served P(θ) with a single peak near 0 degrees (Fig. 4.2c). It means that the ADP is bound stably to the nucleotide binding pocket. The partial ADP release triggered by microtubule binding is indeed inhibited by the mutation in the simulations. Therefore, these results imply that the N-to-K mutation disrupts the signaling within the allosteric network. As a consequence, even if the network senses the presence of the microtubule, it fails to trigger the conformational change that leads to partial ADP release.

In order to investigate how the allosteric network within kinesin responds to external strain, we performed two additional sets of simulations. In the first set, we applied forward strain within the neck linker towards the + end of the microtubule (Fig. 4.2d). Forward strain was shown to increase the kinesin-ADP affinity [69]. In the second set, we applied backward strain, which was shown to decrease the protein-nucleotide affinity [69].

Under forward strain, we observed an angular distribution (Fig. 4.2d) similar to the distribution before microtubule binding (Fig. 4.2a). We surmise that forward strain inhibits partial ADP release. In comparison, when we generated backward strain within the neck linker, the angular distribution, P(θ) (Fig. 4.2e) is similar to the distribution of the ADP-kinesin-microtubule complex (Fig. 4.2b). Therefore, we observed the release of the adenine base, the ribose, and the α-phosphate of the ADP from the nucleotide binding pocket under backward strain.

In summary, our simulations show that microtubule binding triggers the release of the adenine, the ribose, and the α-phosphate of the ADP release from the nucleotide binding pocket of the kinesin within a microsecond. In addition, such

partial ADP is blocked by a previous reported mutation on kinesin. It can also be inhibited by forward strain within the neck linker. Therefore, our results (Fig. 4.2) are in accord with experiments, which demonstrated that while microtubule binding accelerates ADP release from kinesin [19, 120], certain point mutation [71] and forward strain [69] can inhibit the nucleotide release process. Assuming that the conformational change causing the partial ADP release within a microsecond is also critical to the ultimate release of the entire nucleotide, our simulations reveal for the first time the allosteric network (see next subsection) responsible for controlling ADP release from the kinesin.

4.3.4 A simple allosteric network controls ADP release from the kinesin

One might imagine that only an intricate allosteric network would be capable of sensing different environmental conditions (such as the presence of forward strain), and controlling ADP release accordingly. However, our simulations suggest that the allosteric network used to respond to different external forces is surprisingly simple. In the following, we will first describe the elements in the allosteric network, including the key element that triggers partial ADP release. Second, we will explain how this network senses the presence of the microtubule and triggers ADP release. The model also explains how mutation could alter communication within the allosteric network. Finally, we will explain how forward strain affects the allosteric network.

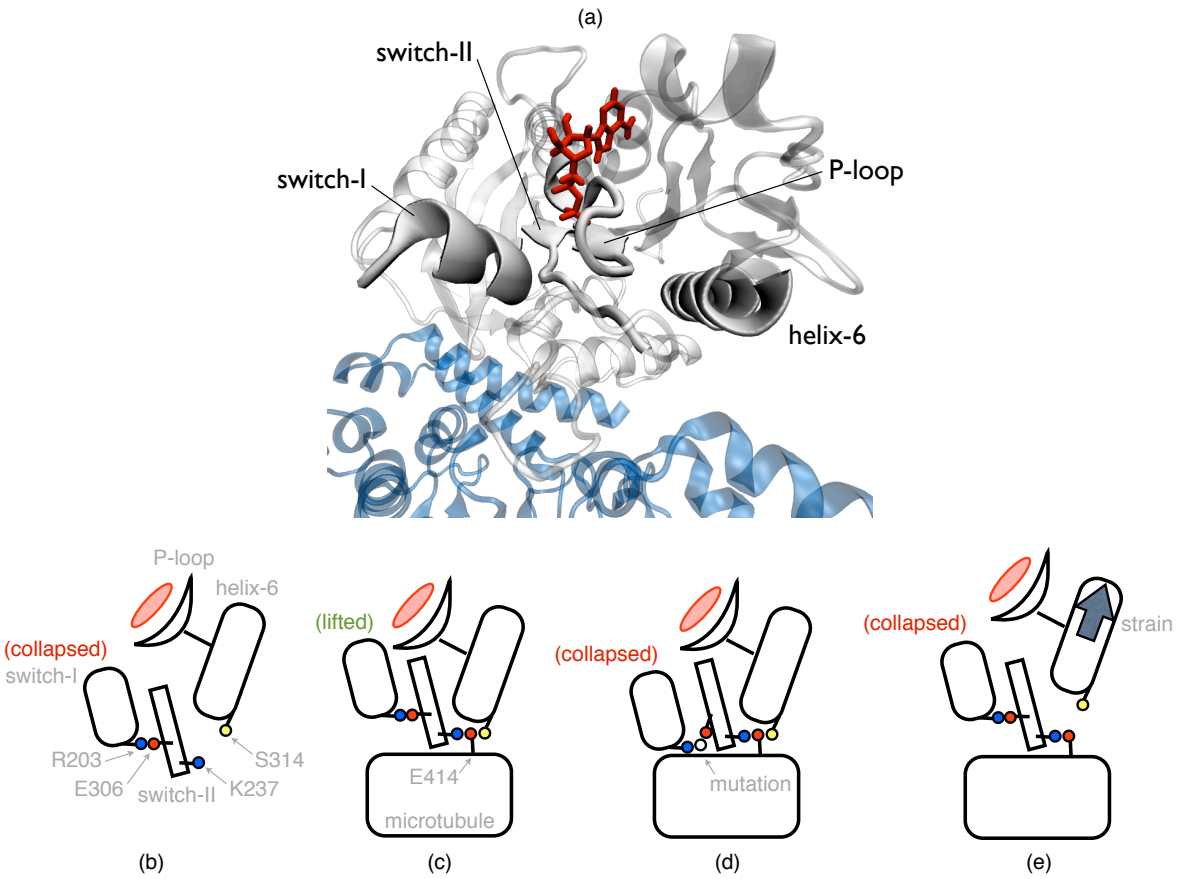

Figure 4.3: The allosteric network and its response to microtubule, mutation, and strain

(a) Four elements (switch-I, switch-II, helix-6 and the P-loop) of the allosteric network are highlighted. Kinesin is colored in white, ADP in red, and the microtubule in blue. (b) A cartoon representation of the allosteric network and its conformation in the absence of the microtubule. (c) The conformation of the allosteric network in the presence of the microtubule. (d) The conformation of the allosteric network in the presence of the mutation N255K. (e) The conformation of the allosteric network under forward strain.

There are four elements in the proposed allosteric network model, switch-I, switch-II, helix-6 and the P-loop (Figs. 4.3a-4.3b). While the P-loop is the element that holds the ADP in the crystal structure, switch-I is the element that triggers partial ADP release. The conformation of switch-I depends on three key interactions between these four elements. Only if all three interactions are intact, can switch-I adapt a lifted conformation to trigger partial ADP release (Fig. 4.3c).

First, switch-I and switch-II are connected by a salt bridge (between R203 and E236, see Fig. 4.3b). Second, switch-II could be linked to helix-6 through a microtubule-mediated interaction (between K237 and S314, see Fig. 4.3c). Third, helix-6 and the P-loop are held together by three or four hydrogen bonds **evidences?**. Given the interaction between helix-6 and the P-loop is stable in all the trajectories, the conformation of switch-I is determined by the R203-E236 salt bridge between switch-I and switch-II, and the microtubule-mediated interaction between switch-II and helix-6. The salt-bridge and the microtubule-mediated interaction constitute an "AND" gate to control the conformation of switch-I. The conformation of switch-I, in turn, triggers or inhibits ADP release.

In the absence of the microtubule (Fig. 4.3b), the microtubule-mediated interaction between switch-II and helix-6 cannot be formed. Therefore, even if the salt-bridge between switch-I and II is already formed, both switch-I and II are in a collapsed conformation **what odes this mean?**. The collapsed switch-I is too far away from the P-loop and the bound nucleotide, to trigger partial ADP release. Therefore, no partial ADP release is observed in the absence of the microtubule.

Upon microtubule binding (Fig. 4.3c), the microtubule-mediated interaction

between switch-II and helix-6 is formed. The salt-bridge between switch-I and II remains stable. As a result, both switch-I and II are pushed up towards the P-loop. Once switch-I adapts this lifted conformation, it is close enough to the bound nucleotide to trigger partial ADP release **provide summary of the model here**.

We have already argued that both the salt-bridge and the microtubule-mediated interaction are necessary for a lifted switch-I and partial ADP release. If any of these interactions are disrupted it could inhibit partial ADP release. For example, the mutant N255K disrupts the salt-bridge between switch-I and II (Fig. 4.3d). Forward strain breaks the microtubule-mediated interaction between switch-II and helix-6 (Fig. 4.3e). Both factors cause collapse of switch-I and II, thus inhibiting partial ADP release.

In the following, we will provide five lines of evidence to support the model: (i) the microtubule pushes up both switch-I and II (Fig. 4.4); (ii) the N255K mutation disrupts the salt-bridge between switch-I and II, thus causing the collapse of both switch regions (Fig. 4.5); (iii) forward strain breaks the microtubule-mediated interaction between switch-II and helix-6, and therefore causes the collapse of the switch regions (Fig. 4.6); (iv) the microtubule-mediated interaction remains intact under backward strain (Fig. 4.7); (v) only switch-I in a lifted conformation **what does lifted mean?** can trigger partial ADP release (Fig. 4.8).

4.3.5 Microtubule pushes up switch-I and II.

Microtubule binding enables the formation of the microtubule-mediated interaction between switch-II and helix-6, and thus pushes both switch-I and II towards the P-loop (Fig. 4.3c and Fig. 4.4). Upon microtubule binding, the positively charged K237 of switch-II forms a salt-bridge with the negatively charged E414 of the α-tubulin **LZ certainly can sow this**. E414 also forms a hydrogen bond with S314 of helix-6 (Fig. 4.4a). This hydrogen bond is further supported by a neighboring salt bridge between α-tubulin and helix-6 (see below). In order to demonstrate the formation of microtubule mediated interaction between switch-II and helix-6, we compare the side chain distance between K237 of switch-II and S314 of helix-6 before and after microtubule binding (Fig. 4.4b). Both the mean and the width of the distance distribution decrease upon microtubule binding. These results indicate the formation of a stable link between switch-II and helix-6.

Formation of the microtubule-mediated interaction in turn leads to the upward motion of both switch-I and II towards the nucleotide binding P-loop. To illustrate such an upward motion, we overlay the snapshot of switch-I, switch-II, and P-loop before and after microtubule binding (Fig. 4.4c). In order to quantify the motion of switch-II towards the P-loop, we measured the side chain distance between D231 of switch-II and T92 of the P-loop. We found that before microtubule binding the distance varies widely and can be as large as 6-8 $\mathring{A}$. However, the distance is sharply peaked near 3 $\mathring{A}$ after microtubule binding (Fig. 4.4d). These results show that switch-II moves towards the P-loop upon microtubule binding. Similarly, we can

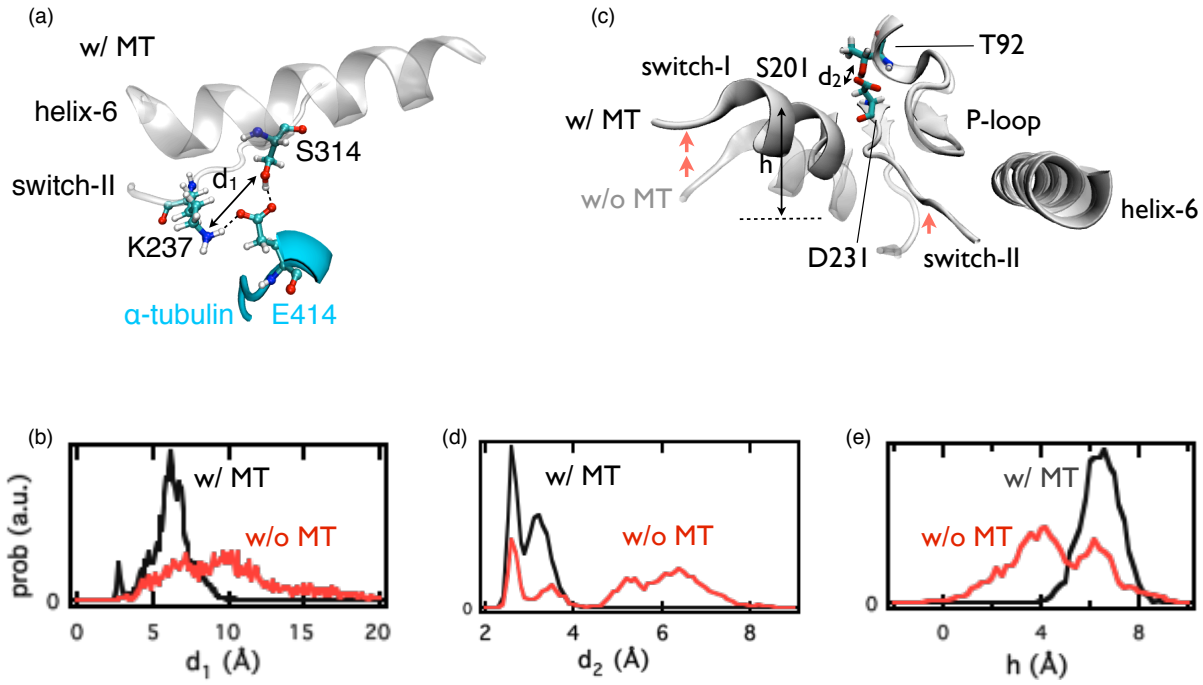

Figure 4.4: Microtubule pushes up both switch-I and II

(a) The microtubule mediated interaction between switch-II and helix-6. K237 of switch-II, E414 of the α-tubulin, and S314 of helix-6 are presented as sticks and spheres. The double ended arrow indicates d_1 (the distance between the side chain nitrogen "NZ" of K237 in switch-II and the side chain oxygen "OG" of S314 in helix-6) in the presence of the microtubule. (b) The distribution of d_1 in the absence (green) and presence (grey) of the microtubule. (c) Representative conformation of the allosteric network in the absence (transparent) and presence (white) of the microtubule. The red arrows indicate the movement of switch-I and II upon microtubule binding. The black double ended arrow on the left indicates h (the relative height of main chain carbon "CA" of S201 in switch-I), and the black arrow on the right indicates d_2 (the distance between the side chain oxygen "OG1" of T92 in the P-loop and the side chain oxygen "OD1" of D231 in switch-II) in the presence of the microtubule. (d) The distribution of d_2 in the absence (green) and presence (grey) of the microtubule. (e) The distribution of h in the absence (green) and presence (grey) of the microtubule.

also quantify the upward motion of switch-I by measuring the change in the height (see Fig. 4.4c) of a switch-I residue (S201) upon microtubule binding (Fig. 4.4e). In summary, these results collectively show that the microtubule pushes switch-I and II towards the P-loop, through microtubule-mediated interactions between switch-II and helix-6 (Fig. 4.3c).

4.3.6 N255K mutation disrupts the salt-bridge between switch-I and II.

Residue 255, in the microtubule-binding helix-4 (Fig. 4.5a), is located between the microtubule and the salt-bridge connecting switch-I and II. In the wild type, N255 is not charged, and does not form a stable contact with either R203 or E236 (Fig. 4.5a). In the mutant, however, residue K255 becomes positively charged just like R203. Therefore, K255 also forms a salt-bridge with the negatively charged E236 (Fig. 4.5b).

As a consequence, K255 pulls the E236 towards the microtubule and away from the P-loop (Fig. 4.5b). It causes the collapse of switch-I and switch-II. To demonstrate that this is indeed the case, we calculated the side chain distance between T87 of the P-loop and E236 of switch-II. We found that the distance increases significantly in the N255K mutant (Fig. 4.5c), suggesting that switch-I and II move far away from the P-loop due to the N255K mutation. In conclusion, the N255K mutation causes the collapse of switch-I and II, by pulling down the inter-switch salt bridge (Fig. 4.3d).

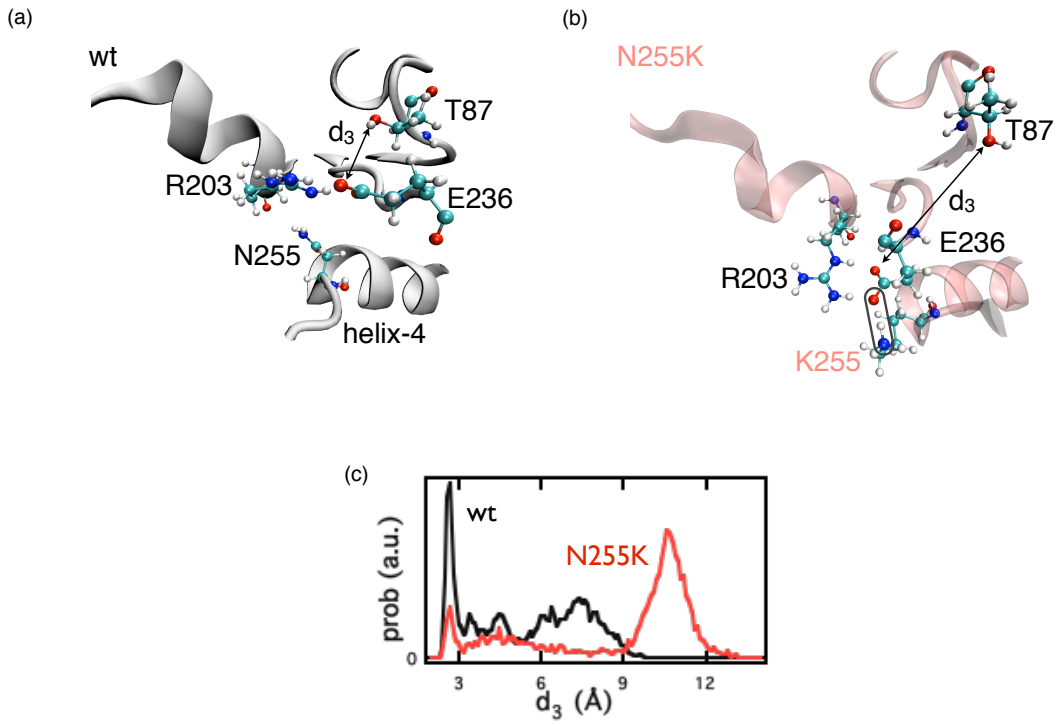

Figure 4.5: Mutation N255K disrupts the salt-bridge between switch-I and II

(a) Location of the residue 255 with respect to the salt-bridge between R203 of switch-I and E236 of switch-II in the ADP-kinesin-microtubule complex. T87 of the P-loop, R203, E236, N255 of helix-4 are presented as sticks and spheres. The double ended arrow indicates d_3 (the distance between the side chain oxygen "OG1" of T87 in the P-loop and the side chain oxygen "OE1" of E236 in switch-II) in the ADP-kinesin-microtubule complex. (b) Same as (a) except that K255 of helix-4 forms a salt-bridge with E236 of switch-II, and pulls down the salt bridge between R203 of switch-I and E236 of switch-II, in the ADP-kinesin[N255K]-microtubule complex. (c) The distribution of d_3 in the wild type (grey) and N255K mutant (pink).

4.3.7 Forward strain disrupts the microtubule-mediated interaction between switch-II and helix-6.

Forward strain pulls S314 of helix-6 towards the microtubule + end. As result, the hydrogen bond between S314 of helix-6 and E414 of the α-tubulin (Figs. 4.6a-4.6b) is broken. In order to demonstrate this, we compared the side chain distance between S314 and E414 before and after introducing forward strain. We found that the average distance between helix-6 residue and the microtubule residue increases from $\leq$5 $\mathring{A}$ to $\geq$10 $\mathring{A}$ (Fig. 4.6c). Once the hydrogen bond between helix-6 and the α-tubulin is impaired, the microtubule-mediated interaction between helix-6 and switch-II is broken.

Because forward strain impairs the microtubule mediated interaction between helix-6 and switch-II, the switch regions collapse (Figs. 4.6d-4.6e), which is evident by comparing the side chain distance between D231 of switch-II and T92 of the P-loop. Without the strain the average distance is $\sim$ 3 $\mathring{A}$ (Fig. 4.6f), allowing formation of hydrogen bonds between switch-II and the P-loop. Under forward strain, the average distance increases to more than $\sim$ 6 $\mathring{A}$ (Fig. 4.6f), indicating the collapse of switch regions. In summary, forward strain within the neck linker breaks the interaction between helix-6 and the α-tubulin, and causes the collapse of switch-I and II (Fig. 4.3e). Once switch-I is collapsed, it can no longer trigger partial ADP release.

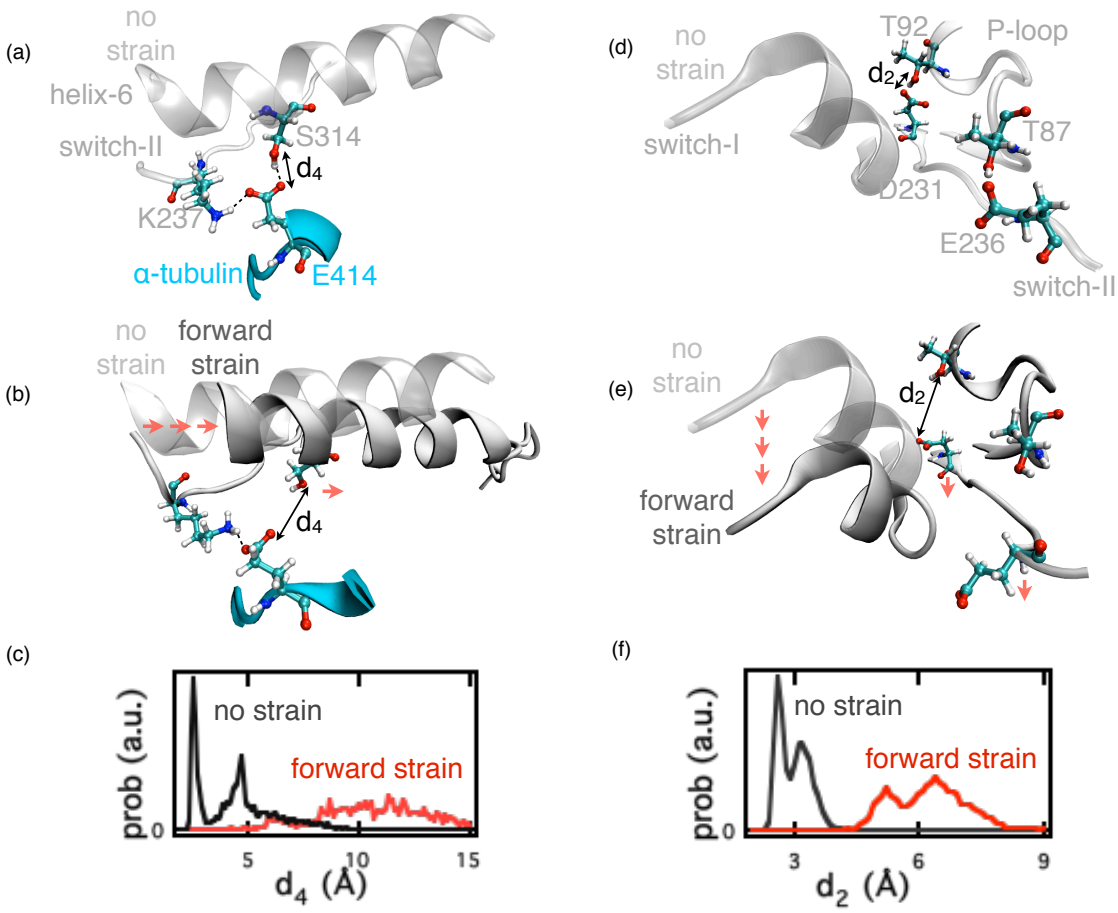

Figure 4.6: Forward strain disrupt the microtubule-mediated interaction between switch-II and helix-6

(a) The microtubule mediated interaction between switch-II and helix-6 under the no strain condition. The double ended arrow indicates d_4 (the distance between the side chain oxygen "OE1" of E414 in the α-tubulin and the side chain oxygen "OG" of S314 in helix-6). (b) Forward strain within the neck linker causes a corresponding forward motion (indicated by red arrows) of helix-6, and breaks the hydrogen bond between S314 in helix-6 and E414 in the α-tubulin. (c) The distribution of d_4 under no strain (black) or forward strain (red) conditions. (d) Both switch-I and II are in the lifted conformation under the no strain condition. The double ended arrow indicates d_2 (the distance between the side chain oxygen "OG1" of T92 in the P-loop and the side chain oxygen "OD1" of D231 in switch-II). (e) Forward strain within the neck linker causes the collapse (indicated by red arrows) of the switch regions, and breaks two hydrogen bonds between the P-loop and switch-II (T92-D231 and T87-E236). (f) The distribution of d_2 under no strain (black) or forward strain (red) conditions.

4.3.8 The microtubule-mediated interaction remains intact under backward strain.

In the previous section we showed how forward strain causes the collapse of the switch regions and therefore inhibits partial ADP release. Given that backward strain is also applied to the neck linker at the C-terminal of helix-6, it seems surprising that partial ADP release still occurs under backward strain. In the following, we will examine how forward and backward strain affect kinesin differently. In particular, we will focus on why the interaction between helix-6 and the α-tubulin, which is broken under forward strain (Fig. 4.7b), remains intact under backward strain (Fig. 4.7a).

Two factors protect the hydrogen bond between S314 in helix-6, and E414 of the α-tubulin. First, the hydrogen bond is protected by an upstream salt bridge between R321 of helix-6 and E415 of the α-tubulin (Fig. 4.7a). While R321 is only $\sim$5 $\mathring{A}$ away from T324, the boundary between helix-6 and the strained neck linker, S314 is $\sim$15 $\mathring{A}$ away from T324. Therefore, the upstream salt bridge between R321 and the α-tubulin, if stable, can decrease the impact of the strain on the downstream hydrogen bond. Indeed, the salt bridge is stable under backward strain. Under backward strain, the average distance between these two R321 and E415 is $\sim$3 $\mathring{A}$ (Fig. 4.7c), suggesting that the salt bridge is stable. Under forward strain, however, the average distance increases to $\sim$10 $\mathring{A}$ (Fig. 4.7c), indicating that the salt bridge is broken.

Second and perhaps more importantly, the geometry of the microtubule pre-

vents the backward motion of helix-6 under backward strain. Helix-6 and helix-4 are connected through a salt-bridge and a hydrogen bond. Therefore, any backward motion of helix-6 will cause a corresponding motion for helix-4. However, as helix-4 sites are in a groove between α- and β-tubulin, its motion can be constrained by the geometry of the groove. Our simulations show that it is much easier for helix-4 to move in the forward (+ end of the microtubule) direction (Figs. 4.7d-4.7e). To show that, we tracked the motion of E270 of helix-4 along the microtubule axis. We found that E270 moves towards the + end of the microtubule by ~ 8 $\mathring{A}$ under forward strain. In comparison, it moves merely ~ 1 $\mathring{A}$ towards the -end under backward strain (Fig. 4.7f). Therefore, backward strain fails to produce sufficient movement of helix-6 to break the important interaction between helix-6 and the α-tubulin.

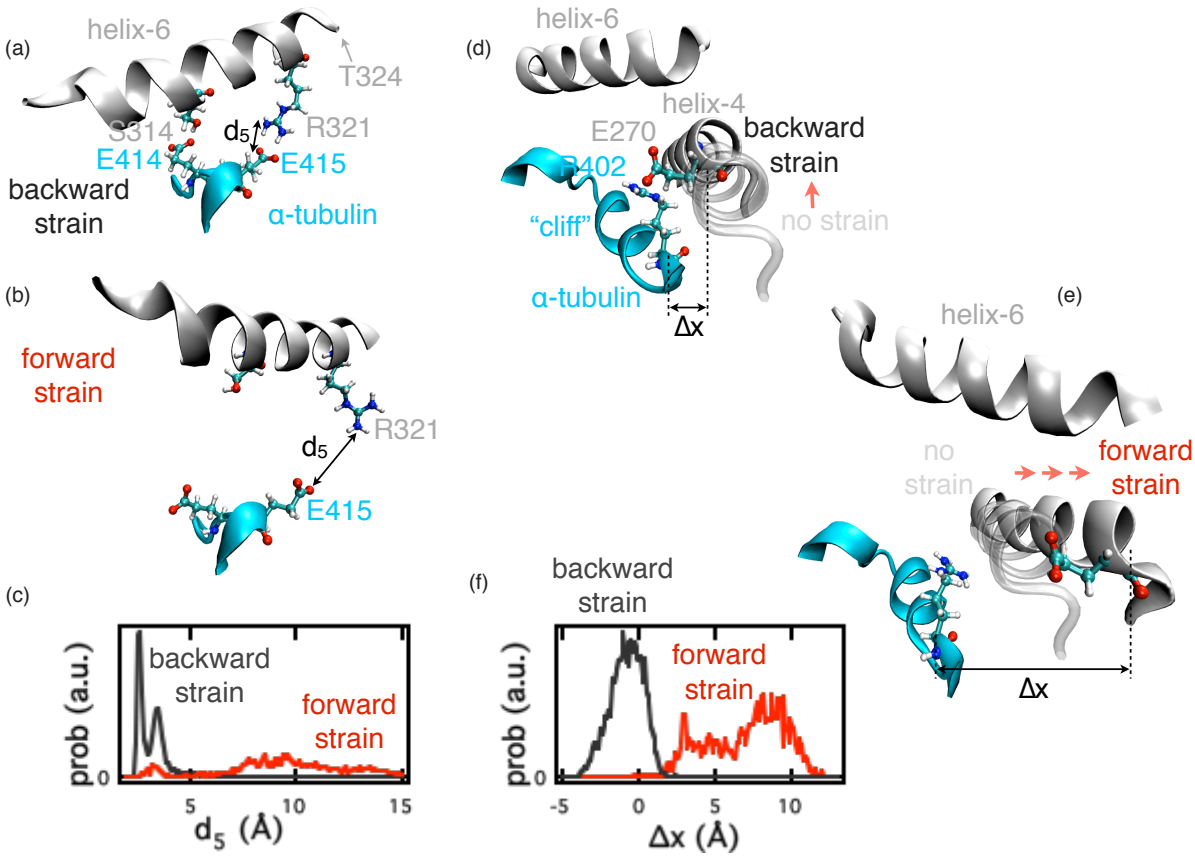

Figure 4.7: The microtubule-mediated interaction between switch-II and helix-6 remains intact under backward strain

(a) Under backward strain, the hydrogen bond between S314 of helix-6 and E414 of the α-tubulin is protected by an upstream salt-bridge between R321 and E415. T324 is the boundary between helix-6 and the strained neck linker. The double ended arrow indicates d_5 (the distance between the side chain nitrogen "NH1" of R321 in helix-6 and the side chain oxygen "OE1" of E415 in the α-tubulin). (b) Under forward strain, both the hydrogen bond (S314-E414) and the salt-bridge (R321-E415) between helix-6 and the α-tubulin are broken. (c) The distribution of d_5 under backward strain (black) or forward strain (red) conditions. (d) Backward strain causes limited backward motion (indicated by the red arrow) of helix-4 and helix-6. The double ended arrow indicates Δx (the difference between the x coordinate of the main chain carbon "CA" of E270 in helix-4 and the x coordinate of the "CA" of R204 in the α-tubulin), which quantifies the movement of the C-terminal of helix-4 along the microtubule axis. (e) Forward strain leads to significant forward motion (indicated by red arrows) of helix-4 and helix-6. (f) The distribution of Δx under backward strain (black) or forward strain (red) conditions.

4.3.9 Only switch-I in the lifted conformation can trigger partial ADP release.

So far we have shown that while the microtubule pushes switch-I into a lifted conformation, either the point mutation or forward strain causes switch-I to collapse. We found that switch-I in a lifted conformation triggers nucleotide release by making contacts with the ribose and adenine of the ADP. In comparison, switch-I in a collapsed conformation is too far away from the bound nucleotide to maintain stable contacts. As a result, the collapsed switch-I cannot trigger partial ADP release. In order to show this, we measured the distance between the side chain oxygen atom of S201 of switch-I and the O2 oxygen atom of the ribose of the ADP (Fig. 4.8a). In the presence of the microtubule, the distance could easily drop below 5 $\mathring{A}$ (Fig. 4.8b). This would allow the formation of hydrogen bonds between the lifted switch-I and the nucleotide. Contacts between switch-I and the ribose of the ADP would then dislodge the adenine base, the ribose, and the α-phosphate from the nucleotide binding pocket. In the absence of the microtubule, the distance usually stays above 10 $\mathring{A}$ (Fig. 4.8b), which prevents switch-I from forming stable contacts with the ADP. As a consequence, in the absence of the microtubule, switch-I cannot pull the nucleotide out of its binding pocket, and trigger partial ADP release.

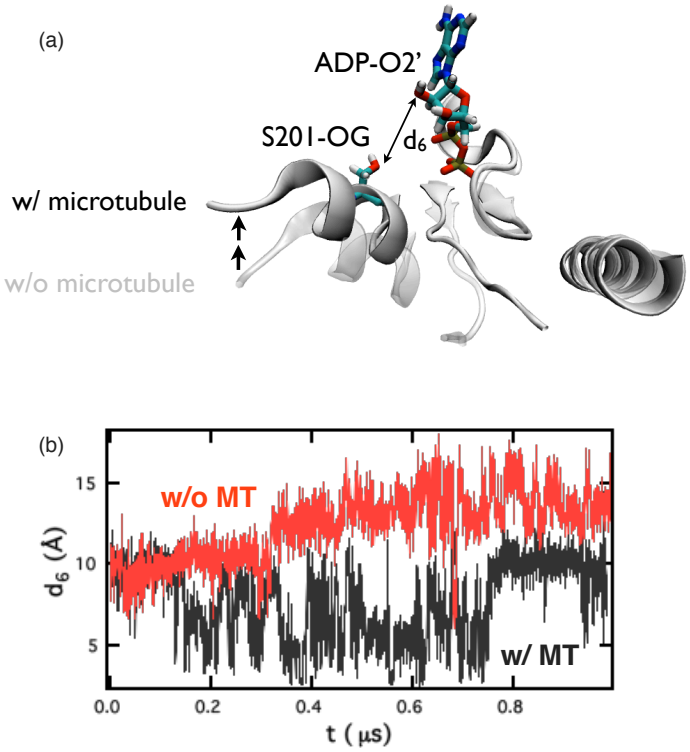

Figure 4.8: Switch-I in lifted conformation makes significant contact with the ADP

(a) Switch-I moves towards the bound nucleotide (indicated by two black arrows) upon microtubule binding. The double ended arrow indicates d_6 (the distance between the side chain oxygen "OG" of S201 in switch-I and the oxygen "O2' " of the ribose of the ADP), which quantifies the distance between switch-I and the ADP. (b) Time-dependent changes in d_6 in the absence (grey) and presence (black) of the microtubule.

4.4 Conclusion

Using extensive molecular dynamics simulations we have proposed a simple allosteric network model for kinesin that describes communication between the motor head and the microtubule. The allosteric network provides a structural explanation of the observed acceleration of ADP release from kinesin upon microtubule binding [19, 120]. The proposed network model also tidily explains how a single point mutation on kinesin inhibits the microtubule-accelerated ADP release [71], as well as the effects of intramolecular strain on kinesin-ADP affinity [69, 70].

It must be emphasized that only partial ADP release was observed in the μs all-atom simulations. The beta-phosphate of the ADP remained stably bound to the nucleotide pocket on the microsecond time scale accessible in our simulations. This finding is not surprising because experiments [19, 120] suggest that the release of the beta-phosphate occurs in milliseconds, which is far beyond the reach of current all-atom simulations. Therefore, our assumption is that the conformational change observed in the μs simulations, which triggers the release of the adenine base, the ribose, and the α-phosphate, is also related to the release of the β-phosphate at much longer timescales.

With this assumption, our allosteric network model shows that ADP release from kinesin is regulated by an "AND" gate. Both the salt-bridge between R203 and E236 and the microtubule-mediated coupling between K237 and S314 must form for ADP release. In the absence of the microtubule, the coupling between K237 and S314 is not formed, and therefore ADP release is slow. The microtubule

accelerates ADP release by connecting K237 to S314. The mutation at residue 255 from N to K inhibits ADP release by disrupting the salt-bridge between R203 and E236, while forward strain does so by breaking the microtubule-mediated coupling between K237 and S314.

Kinesin is just one example where ADP release is regulated through an allosteric network. In many other molecular motors (such as myosin [33, 99], dynein [133, 134], and the molecular chaperone GroEL [98, 125]), the nucleotide binding pocket is also separated from the binding domain of the corresponding factor (such as an actin filament, a microtubule, or a misfolded protein), which triggers ADP release and activates the molecular motor. The case study on kinesin presented in this chapter might provide insights for future study of the allosteric mechanisms in other molecular motors.

Chapter 5

Summary and future perspectives

5.1 Two basic questions about the kinesin step

In this thesis coarse-grained simulation methods have been used to answer two basic questions about the kinesin step. First, does kinesin move by power stroke or diffusion? Second, how does kinesin stay on a single protofilament on the microtubule, given that the polar track usually contains 13 protofilaments?

Previous experiments had identified the power stroke (associated with neck linker docking), a large conformational change in kinesin triggered by ATP binding. However, no experiment so far has quantified the fraction of the kinesin step associated with the power stroke and diffusion. In addition, three experiments based on three different methods showed that kinesin usually walks along a single protofilament. Nevertheless, none of them offered a structural explanation as to how kinesin avoid side steps.

In order to answer these two questions, we simulated thousands of kinesin steps. On average, only 4 nm of the 16 nm kinesin step was found to be associated with the power stroke. The remaining 12 nm is covered by diffusion of the detached head (Fig. 3.3). It is important to point out that although the power stroke is responsible for only one quarter of the kinesin step, it constrains the diffusion of the kinesin molecule and decreases the probability of side steps (Fig. 3.5).

5.2 Structural basis of controlling ADP release from kinesin

Although the microtubule binding site and the nucleotide binding pocket of the kinesin are separated by 1.5 nm [29,105,132], ADP release from kinesin is accelerated by several orders of magnitude upon microtubule binding [19, 120]. Similarly, ADP release is also regulated by strain [69, 70], even though the strain is applied to a region more than 2.3 nm away from the nucleotide binding pocket [29, 132].

However, it is difficult to probe the conformational change of kinesin in response to strain and the microtubule by existing experimental techniques. As a result, how strain and the microtubule reshapes the nucleotide binding pocket of the kinesin has been mysterious.

The results of coarse-grained simulations set the stage for a detailed investigation of the role the microtubule plays in ADP release, which is required for kinesin to complete a step. In order to achieve a detailed structural basis for microtubule-acceleration of ADP release a series of long (1μs) all atom molecular dynamics simulation in explicit water were performed. Furthermore, to answer the questions regarding the effects of strain on ADP release, two additional sets of molecular dynamics simulations (Fig. 4.2) were also performed.

The simulations revealed a surprisingly simple allosteric network that could be responsible for acceleration of ADP release by the microtubule (Fig. 4.3). Moreover, the same allosteric network regulates the ADP-kinesin interaction in a strain-dependent manner.

5.3 Going beyond kinesin?

Stochastic processes are important for the function of many biological systems. For example, diffusion is essential for the motility of kinesin, as shown by our coarse-grained simulations. This can be counterintuitive, given the apparently unidirectional motion of kinesin-transported organelles observed by the optical microscopy [22, 23], as well as the seemingly deterministic kinesin steps recorded using the optical trap or the FIONA (Fluorescence Imaging at One-Nanometer Accuracy [43]). However, diffusion of the kinesin motor head occurs on a faster timescale than the temporal resolution of these techniques (> 30 μs [68]). The kinesin motor head can move by ~ 16 nm through diffusion within a few microseconds, due to its small size (the radius of gyration: ~ 2 nm).

In retrospect, it seems quite natural that cells have developed a transporter that utilizes diffusion or stochastic thermal motion. Kinesin is perhaps just one example of the adaption of cells to its inevitable stochastic microenvironment. Are there other examples at both molecular and cellular level where the thermal motion or stochastic processes in general serve a functional role for biological systems?

5.4 Future perspectives

The present work raises three interesting questions that are of general interest. First of all, why do certain kinesin mutants limp? It was observed in single-molecule experiments that kinesin mutants take alternate fast and slow steps [66]. A recent study suggested that the asymmetry is due to the motion of kinesin perpendicular to

the microtubule surface [47,65]. However, the structural origin of the perpendicular motion, and the difference in the kinesin structure after an odd or even step, are not clear. The coarse-grained simulation method developed in the thesis could well address this question.

A second general question concerns the functional role of thermal fluctuations in other cellular processes. One process of particular interest is transcription initiation in bacteria [135, 136]. On initiation, the RNA polymerase binds to a specific region on DNA called the promoter, which signals where useful information is stored on the DNA. Then the RNA polymerase opens the double stranded DNA, reads the information stored in the template strand, and produces a matching RNA molecule.

In bacteria such as *Thermus aquaticus*, however, the polymerase recognizes a particular promoter region in the single stranded form [135]. This means that the double stranded DNA needs to unwind at least locally, before the polymerase can even recognize the promotor. How could the double stranded DNA open spontaneously, given that it is stabilized by multiple hydrogen bonds and stacking interactions per base? According to one hypothesis [135], thermal fluctuations cause transient flipping-out of a DNA base, which can be recognized and captured by the bacterial RNA polymerase. One could test this hypothesis, using long-timescale molecular dynamic simulations.

A third problem, perhaps more challenging than the first two, is to identify the allosteric network, responsible for the mechanochemical coupling within dynein. Similar to kinesin, dynein is also a cellular transporter that moves along the microtubule [8,137]. One distinct feature of dynein is that the nucleotide binding pockets

and the microtubule binding domain (MTBD) are connected by a 10-nm stalk made of two intertwining helices [133, 134]. Nevertheless, the affinity between the MTBD and the microtubule is still controlled by the nucleotide bound to the other end of the dynein. In addition, despite the long separation between the MTBD and the nucleotide binding pocket, microtubule binding also accelerates ADP release from dynein.

To study the underlying allosteric mechanism from a computational perspective, probably requires multiscale approaches. Given the exceptionally large size of the dynein motor ($\sim$ 15 nm in length and $\sim$ 1.5 Megadaltons in weight), it is impossible to study its allosteric network using only molecular dynamics simulations. The coarse-grained simulation methods (used in the thesis) will be very helpful in studying such large biomolecules. Another advantage of the coarse-grained methods, is that a wide range of parameters can be explored. This allows us to discover key physical ingredients needed to understand complex systems. If all theorists, who are interested in biology could combine the knowledge gained by experimentalist with a toolbox of theoretical and computational techniques, the future would be bright!

Appendix A

Structure of the microtubule-kinesin complex

A.1 Parts list for Microtubule-Kinesin complex

Simulations of stepping dynamics of kinesin along mictrotubules (MTs) require knowledge of the MT-kinesin (MT-Kin) complex. Because even low resolution MT-Kin complex is not currently available we constructed one by stitching together a number of available structures. Although the structures have different resolutions they suffice for our simulations, which are performed using coarse-grained models. The initial conformation of the MT-Kin complex, which may also be the resting state *in vitro* experiments at saturating ATP concentration [118], is taken to be two motor heads bound to MT with the coiled coil attached to the two neck linkers. In order to construct a model for the MT-Kin complex we used the following structures whose coordinates are available in the Protein Data Bank (PDB): (1) For the polar track, we used part of the Downing MT structure [138], which has 13 protofilaments. The Downing model was constructed by fitting the bovine tubulin crystal structure (code 1jff.PDB) onto CryoEM density map. (2) The complex MT-Kin(2p4n.PDB) [88], which was obtained by docking bovine tubulin structure (1jff.PDB) and human monomeric kinesin-1 crystal structure (1bg2.PDB) onto a low resolution CryoEM map of the nucleotide-free MT-Kin complex. (3) Crystal structure of the rat monomeric kinesin-1 (2kin.PDB) [132] containing resolved neck

linker, a structural element that plays a crucial role in kinesin motility [42,82,84,139]. (4) The rat dimeric kinesin-1 crystal structure (3kin.PDB) [75], which is needed to obtain the distance between the C-terminal residues T338 of the neck linker of the leading (LH) and trailing (TH) heads. (5) For the coiled coil we used the *E. Coli* cortexillin I structure (1d7m.PDB) [140].

A.2 Assembly of the MT-Kin complex including coiled coil and cargo

With the parts list at hand, we developed the needed structure of the MT-Kin complex including coiled coil and cargo using the scheme shown in Fig. A.1. The final structure in Fig. A.1 was obtained with two goals in mind. (1) Both heads should be bound to MT, which in our simulations has three protofilaments augmented by e-hooks. (2) The heads are both linked to a cargo, a bead as in many single molecule experiments, through a 30 nm coiled coil.

In order to obtain the MT-Kin complex we proceeded in several steps (see Fig. A.1). In step I, we extracted three protofilaments from the Downing MT, which contains just two $\alpha\beta$ tubulin dimers. We extended the size of each protofilament by adding an additional $\alpha\beta$ unit so that in our simulations each protofilament has three $\alpha\beta$ units. We also added two e-hooks containing 10 (FEEENEGEEF) and 23 (ATA EEEGEMYEDD EEESEAQGPK) residues to the C-terminus of each α and β-tubulin, respectively (Fig. A.1). We have used one letter code for amino acids [141] (http://www.fao.org/docrep/004/Y2775E/y2775e0e.htm). The ehook sequences and the sequence for loop 11 (L11) for the motor domain (see below) were

taken from Protein Knowledge base (UniProtKB) Q2HJB8, Q2T9S0 and Q2PQA9.

In the second step, we attached two motor heads to the center protofilament of the MT with attached e-hooks (Fig. A.1). We first overlapped $\alpha\beta$-tubulin part of 2p4n.PDB onto the $\alpha\beta$-tubulin at the minus-end of the center protofilament. Subsequently, kinesin part of the overlapped 2p4n.pdb was replaced by rat monomeric kinesin structure, which contains the structurally resolved neck linker. Similarly, the second motor head (leading head) was attached to the adjacent $\alpha\beta$-tubulin in middle of the center protofilament. We added the 12 missing residues (SK TGAE-GAVLDE) associated with L11 (SER240 to GLU251) in the motor head of the rat monomer to both heads.

Step III (Fig. A.1) involves dimerization of the two motor heads through a 30 nm coiled-coil. The neck linker (residues T326 to T338) of the leading head was rotated around T326 by about 140^0 so that the distance between T338 of the leading and trailing heads is similar to that in rat dimeric Kin-1 structure. We attached the coiled-coil structure from the rat dimer structure to T338 of the leading and trailing heads. The coiled-coil was further elongated at the C-terminus end by successively adding coiled-coil structure (S254 to K341) from *E. Coli* contexillin I until the contour length becomes 30 nm.

Finally, we linked the C-terminal of the coiled-coil to the spherical cargo. The 500 nm cargo was attached to residue A554 of the coiled-coil so that the initial conformation of the cargo and the coiled- coil satisfied the following conditions. (i) The C-terminal of the coiled-coil, the cargo end of the coiled-coil, and the centroid of cargo are collinear (Fig. A.1). (ii) The N-terminal of coiled-coil, the C-terminal

of the coiled-coil, and the MT axis are coplanar. (iii) The cargo is 20 nm above MT surface (iv) Projection of the centroid of cargo onto the MT axis is behind the projection of the motor end of the coiled-coil.

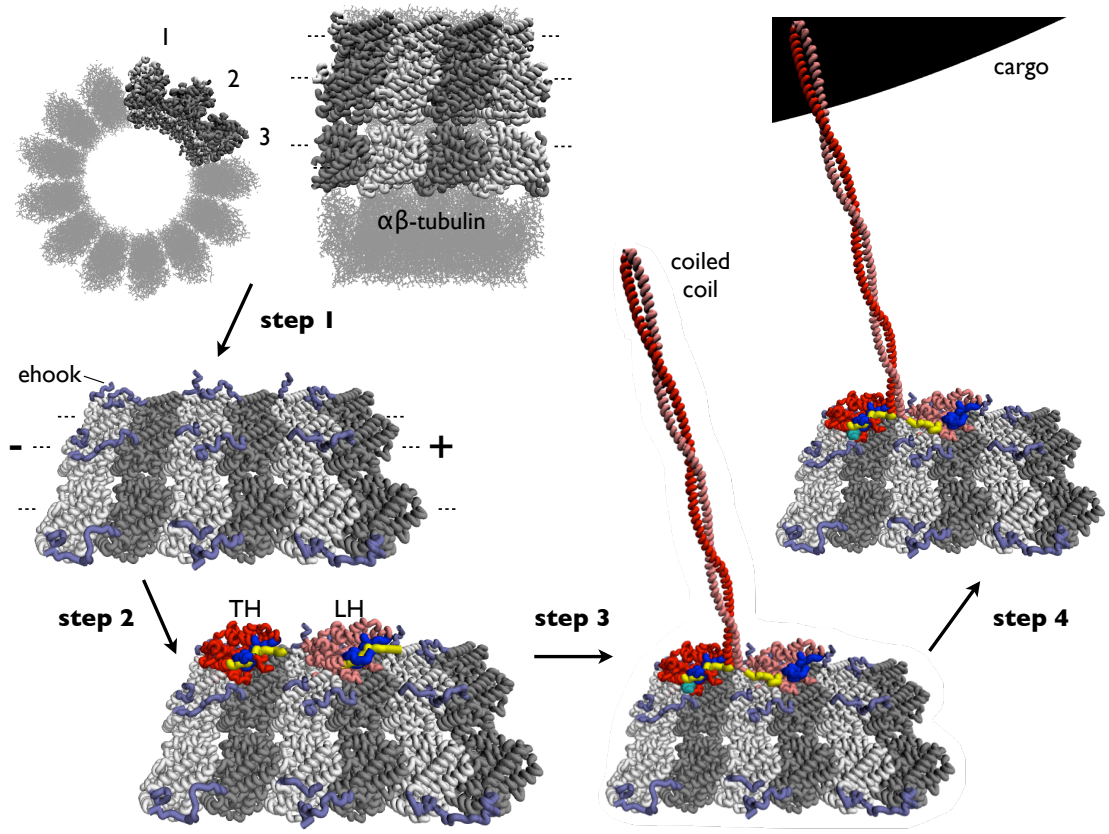

Figure A.1: Steps in modeling of the MT-Kin complex including coiled coil and cargo

α- and β-tubulin are in silver and grey, respectively, and are augmented by e-hooks(violet). The trailing head (TH) is in red, and the leading head (LH) is shown in pink. Yellow structure is the neck linker, and its docking site is in blue. Black represents the 500 nm Cargo. In the final structure, the MT contains three protofilaments, one of which is behind the center protofilament to which TH and LH are bound.

Appendix B

Coarse-grained simulation methods

B.1 Coarse grained Self-Organized Polymer (SOP) model

The large size of Kin (> 1000 residues), MT (> 7000 residues), and the long timescale of kinesin step (> 10 μs) make it necessary to use coarse-grained models, which have been used with great success in a large number of problems in biology [114]. We used the Self-Organized Polymer (SOP) model [98, 115, 116] for the MT-Kin complex. The SOP model has been extensively validated by successful prediction of unfolding pathways of green fluorescence protein [96], allosteric transitions in DHFR [116], and force unfolding of tubulin [100]. In the SOP model, each residue is modeled by one bead centered at C_α atom. Interactions between beads are given by state dependent energy function $H(r_i|X)$ (see Eq. B.1).

Upon ATP binding to the LH and ATP hydrolysis of the TH, kinesin-1 switches from two-head-bound waiting state (W) to a LH-bound stepping state (S) [76]. The trailing head is free to search for the adjacent MT binding site. In order to simulate a single kinesin step along the MT, starting from the state W, we require the energy functions $H(r_i|X)$ to have two distinct minima. One of the minima corresponds to the waiting state (W), and the other represents the stepping state (S). In the W state, the neck linker in the TH is docked, while the LH favors undocked state. The TH is bound to the $\alpha\beta$-tubulin at the (-) end of the center protofilament, and

the LH is bound to the middle $\alpha\beta$-tubulin of the same protofilament (Fig. A.1 final structure). In the S state, the TH favors neck linker undocked state, whereas LH favors docked state triggered by ATP binding. The TH can bind to any non-minus-end and unoccupied $\alpha\beta$-tubulin sites (Fig. 2.1a in chapter 2), while the LH remains bound to the middle $\alpha\beta$-tubulin of the center protofilament throughout the simulations, which mimics the requirement for processive movement.

The SOP energy function that describes the MT-Kin complex is

$$\begin{aligned} H(r_i|X) &= V_{FENE} + V_{NB}^A + V_{NB}^R + V_{NB}^E \\ &= -\sum_Y \sum_{i=1}^{N^Y-1} \frac{k}{2} R_0^2 log(1 - \frac{(r_{i,i+1} - r_{i,i+1}^0(X))^2}{R_0^2}) \\ &\quad + \sum_{Y,Y'} \sum_{i,j} \epsilon_h^{Y-Y'} [(\frac{r_{ij}^0(X)}{r_{ij}})^{12} - 2(\frac{r_{ij}^0(X)}{r_{ij}})^6] \Delta_{ij} \\ &\quad + \sum_Y \sum_{i=1}^{N^Y-2} \epsilon_l (\frac{\sigma}{r_{i,i+2}})^6 + \sum_{Y,Y'} \sum_{i,j} \epsilon_l (\frac{\sigma}{r_{ij}})^6 (1 - \Delta_{ij}) \\ &\quad + \sum_{Y,Y'} \sum_{i,j} \frac{q_i q_j}{4\pi\epsilon r_{ij}} e^{-\kappa r_{ij}} \end{aligned} \tag{B.1}$$

The labels Y and Y' refer to residues TH, LH, and $\alpha\beta$-tubulin. In Eq. B.1, r_{ij} is the distance between the i^{th} C_α atom of protein Y and j^{th} C_α atom of protein Y', and r_{ij}^0 are the corresponding values in the equilibrated state. Notice that Y and Y' can be identical.

The first term in Eq. B.1, V_{FENE}, the finite extensible non-linear elastic (FENE), accounts for chain connectivity, which includes peptide bonds within proteins and the link between the cargo and the N-terminal A553 of the coiled coil. We used $k = 20$ Kcal / (mol $\cdot \mathring{A}^2$) and $R_0 = 2$ $\mathring{A}$. For any peptide bond resolved in crystal structures, $r_{i,i+1}^0$ is the bond length in the PDB structure. Otherwise,

$r^0_{i,i+1}$ is assumed to be 3.8 $\mathring{A}$. For the link between cargo and coiled-coil, we chose $r^0_{i,i+1} = R_{cargo} + 3.8\mathring{A}$. The precise values of k and R_0 are not significant as long as they represent covalent linkage faithfully.

The second term, V^A_{NB}, represents the non-peptide-bond attractive interactions between two residues that are in contact ($\Delta_{ij} = 1$) in state X . Attractive interactions account for the stability of the motor heads and the coiled coil, and prevent premature dissociation of the LH from MT. In both the W and S states, we require that the motor heads remain folded as in the rat monomeric kinesin structure. Accordingly, we assign attractive interaction between residue i and j if (1) $|i - j| > 2$ and (2) r^0_{ij}, the distance in the rat monomeric kinesin structure, is smaller than 1 nm. Similarly, the coiled coil should remain folded as shown in the final structure in Fig. A.1. Attractive interactions between residue i of the LH and residue j of the $\alpha\beta$-tubulin if r^0_{ij} the distance between them in the MT-Kin complex structure is smaller than 1 nm, ensures that the LH is bound to the MT during a single step.

For pairs of interaction with $\Delta_{ij} = 0$, the potential, V^R_{NB} (the third term in Eq. B.1) is repulsive. We chose $\epsilon_l = 1$ Kcal/mol (Eq. B.1) and $\sigma = 3.8$ $\mathring{A}$. For repulsive interactions between residues and the cargo, $\epsilon_l = 1$ Kcal/mol and $\sigma = R_{cargo} + 3.8$ $\mathring{A}$.

To approximately model the effects of electrostatic interactions between the charged residues, we used a simple Debye Huckel potential V^E_{NB} (the fourth term in Eq. B.1). Here $\kappa^{-1} = 1$ nm for $\epsilon = 80\epsilon_0$, and $\kappa^{-1} = 0.35$ nm for $\epsilon = 10\epsilon_0$. The value of 10 ϵ_0 is in the range normally used in the simulation of proteins. In a recent application of promotor melting by bacterial polymerase we have shown varying ϵ

over a reasonable range does not alter the nature of results [136].

The SOP energy function is fairly general requiring only structural models. There are specific additional terms required for applications to stepping dynamics of kinesin. In order to account for the observation that typically coiled coil does not reverse its orientation [142] we constrained $\widehat{u}(0) \cdot \widehat{u}(t) = 1$ for all t where $\widehat{u}(t)$ is the unit vector connecting the two alanines at 553 located at the C-terminal of the coiled coil. Similarly, the distance between two A553 residues are fixed at all times. We used $V_H = \frac{k'}{2}(z_c - z_c^0)^2$, to constrain the height of the cargo above the MT surface. The height of cargo is constrained *in vitro* by the optical trap and presumably by steric repulsion with MT *in vivo*. The restraint also ensures that during the stepping process the cargo moves forward in stead of moving downward, which is physically unrealistic especially during processive motion.

B.2 Equations of motion with hydrodynamic interactions

We assume that the dynamics of the system including the cargo during the stepping process can be described by the Langevin equation in the overdamped limit. The discretized equations for the motor domain of TH (residues 2-326), which includes hydrodynamic interactions, are

$$\vec{r}_i(t+h) = \vec{r}_i(t) + \sum_{j=1}^{N^{TH}} \frac{D_{ij}h}{k_B T}(-\frac{\partial H(r_i|X)}{\partial \vec{r}_j}) + \vec{\Gamma}_i(t). \tag{B.2}$$

Because we are focussed on the dynamics during the stepping process, which predominantly involves movement of the motor domain, we only included hydrodynamic

interactions on the dynamics of the TH. For the rest of the system, which includes the cargo, the coiled coil and the motor domain of LH, we integrated the Langevin equations using

$$\vec{r_i}(t+h) = \vec{r_i}(t) + \frac{h}{6\pi\eta a}(-\frac{\partial H(r_i|X)}{\partial \vec{r_i}}) + \vec{\Gamma}_i(t). \tag{B.3}$$

In Eq. B.3 we assume that the diffusion coefficient ($= k_BT/6\pi\eta a$) is a constant because the coiled-coil remains intact and the LH remains bound to the MT during the stepping dynamics. To account for the possibility that parts of the motor domain of the TH might locally unfold, at least partially, we included the diffusion tensor in Eq. B.2. We used the Rotne-Prager-Yamakawa [143–146] form for the 3×3 diffusion tensor given by D_{ij}. The ij^{th} element of the Rotne-Prager-Yamakawa diffusion tensor is

$$\begin{aligned}
D_{ii} &= \frac{k_BT}{6\pi\eta a} I \\
D_{ij} &= \frac{k_BT}{8\pi\eta r_{ij}}[(1+\frac{2a^2}{3r_{ij}^2})I + (1-\frac{2a^2}{r_{ij}^2})\frac{\vec{r}_{ij}\vec{r}_{ij}}{r_{ij}^2}] \text{ if } r_{ij} \ \geq 2a \\
D_{ij} &= \frac{k_BT}{8\pi\eta r_{ij}}[\frac{r_{ij}}{2a}(\frac{8}{3}-\frac{3r_{ij}}{4a})I + \frac{r_{ij}}{4a}\frac{\vec{r}_{ij}\vec{r}_{ij}}{r_{ij}^2}] \text{ if } r_{ij} < 2a
\end{aligned} \tag{B.4}$$

where k_B is the Boltzmann constant, and T (=290 K) is the temperature, and η (=0.003 Pa·s) is roughly the viscosity of the cytoplasm [117], which is nearly three times larger than the water viscosity. The random force in Eqs. B.2 and B.3 satisfies $< \vec{\Gamma}_i(t) >= 0$. As required by the fluctuation-dissipiation theorem $< \vec{\Gamma}_i(t)\vec{\Gamma}_j(t') >= 6D_{ij}h\delta_{tt'}$ for the residues in the TH motor domain. For all other interaction sites, including the cargo, the Gaussian noise spectrum satisfies $< \vec{\Gamma}_i(t)\vec{\Gamma}_j(t') >= 6\frac{k_BT}{6\pi\eta R_\alpha}h\delta_{tt'}\delta_{ij}$, where R_α is either a or R_{cargo}. The radius, a, of each residue is 0.19 nm, and the integration step h is 0.12 ps.

B.3 Triggering Kinesin Stepping

Initial events in the stepping of kinesin along the MT include docking of neck linker to the catalytic core in the LH, and detachment of the TH from the initial binding site. Docking of the neck linker is accomplished by assigning attractive interaction, ϵ_h^{LH-NL}, at $t = 0$ to each residue pair (i, j) between the neck linker ($i \in$ T326-T338) and the rest of the LH ($j \in$ A2-T326) that satisfies (i) $|i - j| > 2$ and (ii) $r_{ij}^0 < 1nm$ in rat monomeric kinesin structure. Simultaneously, we make the interaction between the motor head of TH and $\alpha\beta$-tubulin subunits toward the (-) end repulsive, to trigger dissociation of TH from the initial binding site. Subsequently, the TH can bind to any of the available sites on the MT surface although heometrical restrictions prevent certain sites from being accessible (see Fig. 2.1b). Interactions between the TH and the three $\alpha\beta$-tubulin sites located towards the (+) end is attractive with strength ϵ_h^{MT-TH}. For two $\alpha\beta$-tubulin above and below the LH, we reduced the strength to $0.5\epsilon_h^{MT-TH}$, because optical trap unbinding experiments [69, 112] indicate that strength of TH-MT interaction depends on the relative position between TH and LH. We varied ϵ_h^{MT-TH} from 0 to 2.0 Kcal/mol in different simulations to account for dependency of MT-TH interaction on the nucleotide state of the TH. The value of ϵ_h^{MT-LH} between LH and MT, however, is set to 2.0 Kcal/mol, to prevent unbinding of LH from MT.

B.4 Simulation Details

We prepared an ensemble of initial equilibrium conformations of the entire system by integrating the equations of motion (Eqs. B.2 and B.3) using $H(r_i|X = W)$. The equilibration was performed for 10^6 time steps, corresponding to $\sim$0.12 μs A trajectory describing the $W \rightarrow S$ transition, with the initial condition $r_i(0)$ obtained during the equilibration run, was generated using Eqs. B.2 and B.3 using $H(r_i|X = S)$. Trajectories for the $W \rightarrow S$ transition are deemed complete after the centers of mass of the motor head and cargo take a 8 nm step towards the + end of the MT. The time for taking a 8 nm step typically exceeds 10 μs. In all we generated between (100-200) trajectories for a range of parameters (see Table B.1 for details).

In the initial stages of the $W \rightarrow S$ transition (usually within about 12 ns $\ll$ the time for completing a single step) there are numerical instabilities due to high forces that arise from switches from $H(r_i|X = W)$ to $H(r_i|X = S)$. To prevent such instabilities, we used $\sigma_{ij}^{W\rightarrow S} = \frac{(K-k)\cdot\sigma + k\cdot r_{ij}^0}{K}$ [98, 116], which is a combination of σ and r_{ij}^0 in 2kin.PDB. Here $K = 100$, and k increase from 0 to 100 within 12 ns. Previous studies showed that the dynamics is not affected by the precise choice of K because the conformational changes in the enzyme (kinesin, coiled coil, and cargo construct in the present case) are slower compared to the transition time [98, 116]. In our case, the fastest process (neck linker docking 0.1 μs) is about one order of magnitude slower than 12 ns during which numerical instabilities typically occur.

In the Brownian dynamics simulations with hydrodynamics interaction, we

immobilized the MT structure except the ehooks. We performed a few tests to ensure that relaxing this condition does not quantitatively affect our results. The immobilization of MT surface has negligible affect on the kinematics of a single step because the persistence length of the microtubule is much larger than the 16nm movement of the TH. Thus fluctuations of the MT on the length scale of a single step is not important. Although other components, such as kinesin-1 or ehooks, can interact with MT according to $H(r_i|X)$, the coordinates of MT (except ehooks) are fixed throughout our simulations.

B.5 Mutation simulations

There are two key energy scales (ϵ_h^{LH-NL} and ϵ_h^{MT-TH}) that control the kinetics of a single step. In order to reveal consequences of neck linker docking to the leading head we performed a number of computations, which we refer to as mutation simulations. In the wild type simulations, we assigned attractive interactions between the residues in the neck linker and the docking site in the catalytic core of the motor head so that NL docks to the leading head. In the mutation simulations, we varied the interactions between the LH neck linker and the docking site in the S state to assess the consequence of lack of NL docking to the leading head. In particular, we varied the strength of the attractive interactions, ϵ_h^{LH-NL}, between NL and LH.

To date there are very few studies that have studied how MT-Kin interactions influence the kinesin step. We conducted a number of simulations to probe the role of

MT in affecting the stepping dynamics. The role MT plays in affecting the stepping dynamics of kinesin is studied by changing the MT-HT interaction strength. These changes also approximately mimic the nucleotide state of the motor head.

Table B.1: Dependence of TH movement upon NL docking on parameters of the force-field

ϵ_r [a]	ϵ_h^{LH-NL} [b]	ϵ_h^{MT-TH} [c]	Def.[d]	τ_{NL} (μs)	x_{TH}^d (nm) [e]	x_{T338}^d (nm)	# of traj.
80	2.0	2.0	1	0.15 ± 0.003	5.1 ± 0.1	6.0 ± 0.01	200
80	2.0	2.0	2	0.62 ± 0.015	8.2 ± 0.2	6.4 ± 0.02	200
80	4.0	2.0	1	0.10 ± 0.002	4.9 ± 0.1	5.9 ± 0.01	100
80	1.0	2.0	1	0.39 ± 0.015	6.4 ± 0.2	6.1 ± 0.02	100
80	2.0	4.0	1	0.15 ± 0.004	5.2 ± 0.1	6.0 ± 0.01	100
80	2.0	1.0	1	0.15 ± 0.004	5.2 ± 0.1	6.0 ± 0.01	100
80	2.0	0.4	1	0.15 ± 0.004	5.2 ± 0.1	6.0 ± 0.01	99
80	2.0	0.2	1	0.15 ± 0.004	5.2 ± 0.1	6.0 ± 0.01	99
80	2.0	0.0	1	0.15 ± 0.003	5.2 ± 0.1	6.0 ± 0.01	100
10	2.0	2.0	1	0.17 ± 0.003	5.0 ± 0.1	5.9 ± 0.01	200
10	2.0	2.0	2	0.67 ± 0.016	7.6 ± 0.2	6.3 ± 0.02	200
10	4.0	2.0	1	0.11 ± 0.003	4.7 ± 0.1	5.9 ± 0.01	100
10	1.0	2.0	1	0.43 ± 0.012	5.9 ± 0.2	6.0 ± 0.02	100
10	2.0	4.0	1	0.17 ± 0.005	5.2 ± 0.1	5.9 ± 0.01	100
10	2.0	1.0	1	0.17 ± 0.004	5.1 ± 0.1	5.9 ± 0.01	100
10	2.0	0.0	1	0.17 ± 0.004	5.0 ± 0.1	5.9 ± 0.01	100

[a] $\epsilon_r = \frac{\epsilon}{\epsilon_0}$, where ϵ is the dielectric constant in V_{NB}^E of Eq. B.1.
[b] ϵ_h^{LH-NL} is the coefficient ϵ_h in V_{NB}^A of Eq. B.1, for attractive interactions between the LH neck linker and its docking sites.
[c] ϵ_h^{MT-TH} is the coefficient ϵ_h in V_{NB}^A of Eq. B.1, for attractive interactions between the TH and $\alpha\beta$-tubulins on MT.
[d] Definition 1 for docked neck linker corresponds to $\Delta_c = 0.08$ nm and $\delta_c = 0.2$. Definition 2 corresponds to $\Delta_c = 0.06$ nm and $\delta_c = 0.15$.

[e] Average distance traversed by the TH along the microtubule axis.

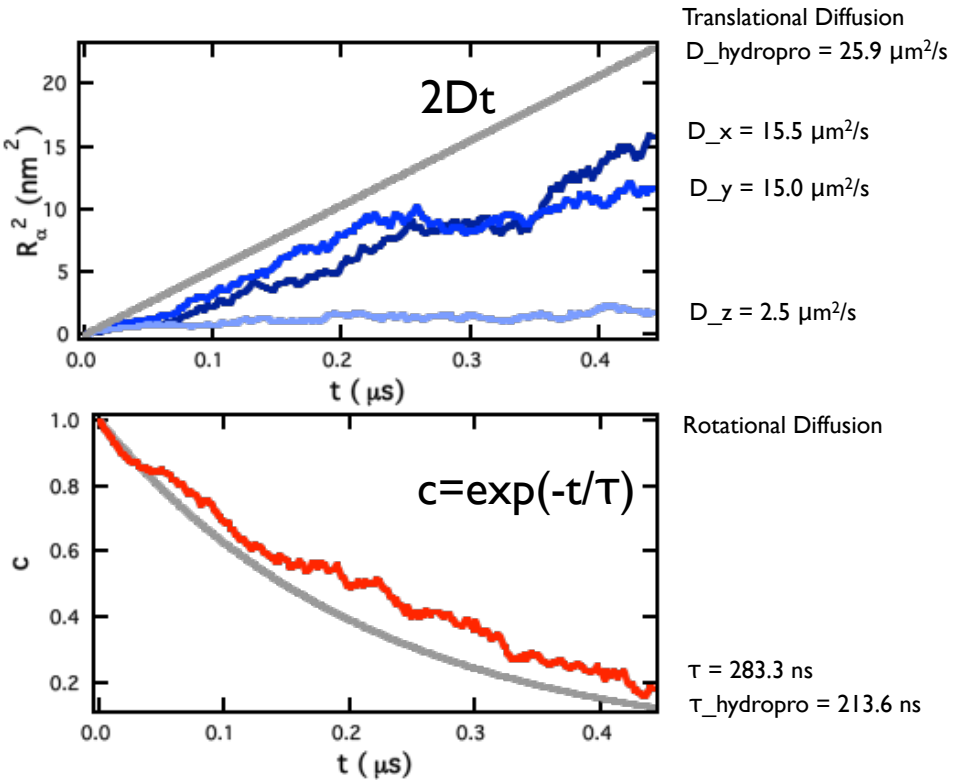

Figure B.1: Diffusion constants of the TH during a single step

Mean square displacements along x (dark blue), y (blue), and z (light blue) axis, during the first 0.45 μs of directed diffusion (Fig. 2.5), calculated using trajectories, in which the TH reaches the neighborhood of the TBS. Auto-correlation function $c(t) = 0.5(cos\theta_1(t) + cos\theta_2(t))$, during the first 0.45 μs of directed diffusion stage, is plotted in red and the grey line corresponds to c(t) for a freely rotating motor head in isolation predicted by HydroPro [90]. Angles θ_1 and θ_2 are defined in Eqs. 2.4-2.5 in chapter 2.

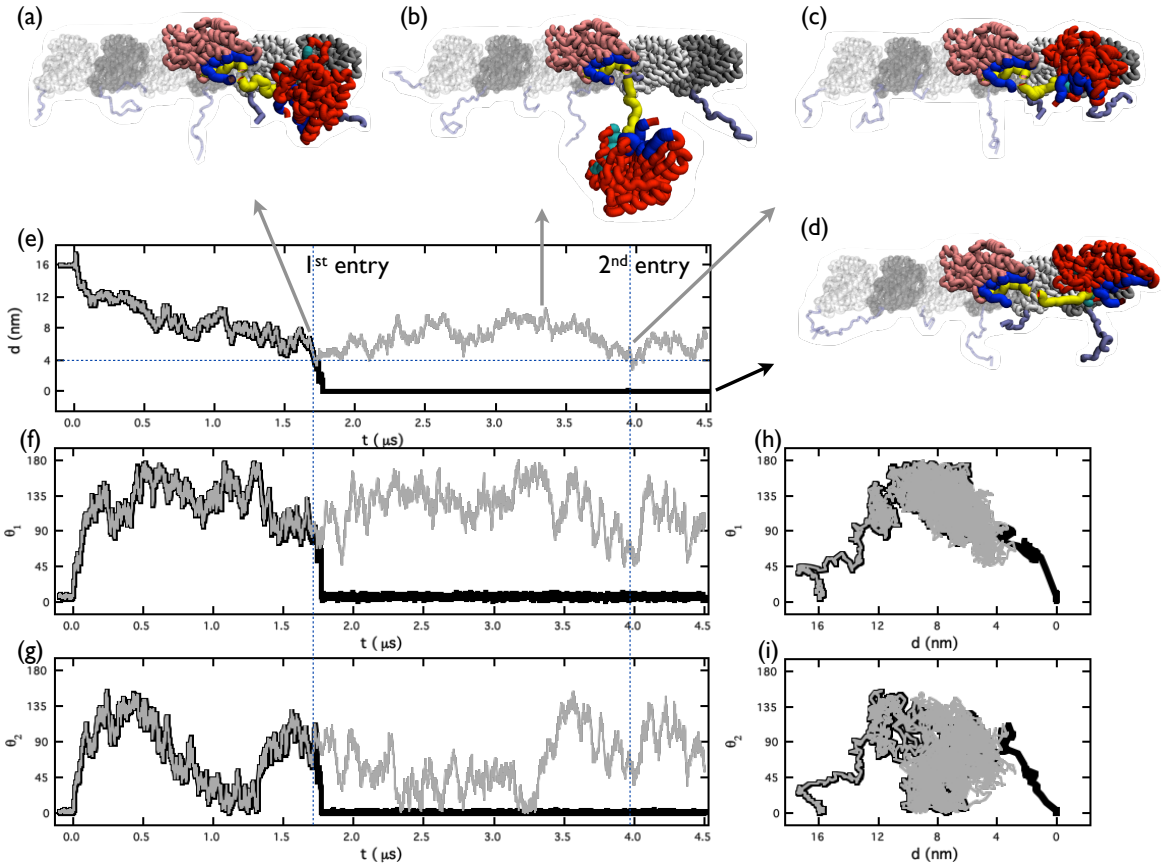

Figure B.2: Effect of TH-MT interaction on TH binding to the TBS

(a-c) Three snapshots in a representative trajectory in which TH-MT interaction is repulsive, show that TH fluctuates in and out of the neighborhood of the TBS. (d) A snapshot of TH bound to the TBS, in simulations in which TH-MT interaction is strongly attractive (ϵ_h^{MT-TH} =2 Kcal/mol). (d) The time dependent changes in $d(t)$ (Eq. 2.3 in chapter 2) as a function of t. (e) and (f) Variation of $\theta_1(t)$ and $\theta_2(t)$ (Eqs. 2.4-2.5 in chapter 2) as a function of t. In (d), (e) and (f), black lines are for trajectories with strong TH-MT and grey for repulsive TH-MT interactions. (h) and (i) shows $\theta_1(t)$ and $\theta_2(t)$ as a function of d during the first 4.5 μs.

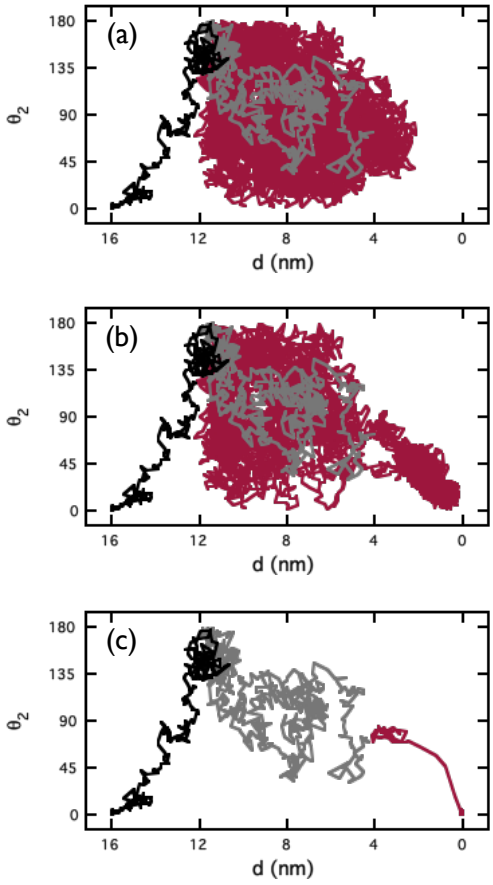

Figure B.3: Effect of ϵ_h^{MT-TH} on the TH dynamics in the final stage of the 16nm step

The angle θ_2 (Eqs. 2.5 in chapter 2), the orientation of TH, as a function of d, the center of mass distance between the TH and TBS, in three trajectories, in which the TH-MT interaction is repulsive (a), weakly attractive (b), and strongly attractive (c). In each trajectory, the jump dynamics ca be partitioned into three stages: neck linker docking (black), constrained diffusion (grey), and microtubule capture (red).

Appendix C

Molecular dynamics simulation methods

C.1 Preparation of simulation systems

For all five sets of simulations, we used the same structural model of the kinesin-microtubule complex (Protein Data Bank ID: 2p4n). 2p4n.pdb was constructed based on docking the crystal structure of human kinesin (1bg2.pdb) and the crystal structure of bovine microtubule (1jff.pdb) into the Cryo-electron microscopy image of the kinesin-microtubule complex at 9 $\mathring{A}$ resolution [88]. We downloaded 2p4n.pdb from the Protein Data Bank and modified it, to fit the goal of the each of the five sets of simulations.

In the first set of simulations (ADP-kinesin complex), we deleted the microtubule in the 2p4n.pdb, keeping only the kinesin. Next, we added one residue (A2) at the N-terminal of the kinesin, and deleted two residues (T324 and I325) belong to the neck linker at the C-terminal of the kinesin. The reason we deleted the two remaining residues (T324 and I324) of the neck linker, is to ensure that there would be no intramolecular strain induced by the neck linker in the first set of simulations.

The second set of simulations (ADP-kinesin-microtubule complex) is the same as the first set, except we kept the microtubule in 2p4n.pdb. In the third set of simulations (ADP-kinesin[N255K]-microtubule complex), we made one additional change: switching the kinesin residue 255 from N to K. This N to K mutation

was found to impair the microtubule-accelerated ADP release using biochemical assays [71].

In the fourth set (ADP-kinesin-microtubule complex under forward strain), we grafted the neck linker (T324 to T336) from another crystal structure of human kinesin 1mkj.pdb into the system. T324 to T336 from 1mkj.pdb is attached to K323 of the ADP-kinesin-microtubule complex. To mimic the forward strain within the neck linker, the vector pointing from the α-carbon of T324 to the α-carbon of T336 is kept parallel to the microtubule axis and towards the (+) end of the microtubule.

The last set (ADP-kinesin-microtubule complex under backward strain) is similar to the previous set, except that the grafted neck linker is pointing towards the (-) end of the microtubule. Given these manuel modifications performed to the original structure file 2p4n.pdb, we equilibrated these modified structures by $\sim$ 10-20 ns (see below) to minimize unrealistic conformations and interactions.

C.2 Equilibration of simulation systems

First, we solvated each ADP-kinesin-microtubule complex by constructing a $125\mathring{A}\times$ $87\mathring{A}\times$ $120\mathring{A}$ water box surrounding the protein complex. The length of the water box along the longitudinal and lateral axis of the microtubule, are $125\mathring{A}$ and $87\mathring{A}$, respectively. For the ADP-kinesin complex, we chose a cubic water box ($96\mathring{A}\times$ $96\mathring{A}\times$ $96\mathring{A}$). After solvation, we add ions to (1) neutralize the system and (2) reach the ionic concentration (150mM).

Next, we equilibrated each structure for 10-20 ns, after 100,000 steps of energy

minimization. The force field we used is CHARMM22 [147, 148], and the ensemble is NPT (P = 1atm, T = 310K).

During this equilibration stage and later microsecond simulations, we applied system-dependent constraints on each ADP-kinesin-microtubule complex. In all four sets of simulations with the microtubule, we fixed the α-carbon atom of the C25 and E290 of the α-tubulin, and S25 and E290 of the β-tubulin. All these residues locate far from the kinesin-microtubule interface in 2p4n.pdb. Such position constraints are necessary (1) to prevent the translational and rotational diffusion of the microtubule, and (2) to apply strain within the neck linker of the kinesin in certain simulations. In order to apply forward (backward) strain, we fixed the T336 to the forward (backward) position at the end of the manuel structural modification, to keep the extension and the orientation of the neck linker.

C.3 Microsecond molecular dynamics simulations on Anton supercomputer

After five sets of equilibration on a local computer cluster using NAMD [149], we transferred the equilibrated structures to the Anton supercomputer [128–131], hosted at Pittsburgh Supercomputing Center (PSC). There, for each set of simulations, we performed at least two 1μs simulations, starting from different equilibrated structures. For all simulations performed at PSC, we also used the same CHARMM22 force field, and the NPT ensemble (P = 1atm, T = 300 K).

Bibliography

[1] T. A. McMahon. Muscles, reflexes and locomotion. *Princeton Univ. Press, Princeton, NJ, 1984.*

[2] H. E. Huxley. Mechanism of muscular contraction. *Science*, 164:1356–1365, 1969.

[3] R. E. Cheney, M. K. Oshea, J. E. Heuser, M. V. Coelho, J. S. Wolenski, E. M. Espreafico, P. Forscher, R. E. Larson, and M. S. Mooseker. Brain myosin-V is a two-headed unconventional myosin with motor activity. *Cell*, 75:13–23, 1993.

[4] A. L. Wells, A. W. Lin, L. Q. Chen, D. Safer, S. M. Cain, T. Hasson, B. I. Carragher, R. A. Milligan, and H. L. Sweeney. Myosin VI is an actin-based motor that moves backwards. *Nature*, 401:505–508, 1999.

[5] I. R. Gibbons and A. J. Rowe. Dynein - a protein with adenosine triphosphatase activity from cilia. *Science*, 149:424–426, 1965.

[6] K. E. Summers and I. R. Gibbons. Adenosine triphosphate-induced sliding of tubules in trypsin-treated flagella of sea-urchin sperm. *Proc. Natl. Acad. Sci. U. S. A.*, 68:3092–3096, 1971.

[7] M. A. Sleigh. Cilia and flagella. *Academic Press, New York, NY, 1974.*

[8] B. M. Paschal, H. S. Shpetner, and R. B. Vallee. MAP1C is a microtubule-activated ATPase which translocates microtubules in vitro and has dynein-like properties. *J. Cell Biol.*, 105:1273–1282, 1987.

[9] B. J. Schnapp, R. D. Vale, M. P. Sheetz, and T. S. Reese. Single microtubules from squid axoplasm support bidirectional movement of organelles. *Cell*, 40:455–462, 1985.

[10] R. D. Vale, B. J. Schnapp, T. S. Reese, and M. P. Sheetz. Movement of organelles along filaments dissociated from the axoplasm of the squid giant axon. *Cell*, 40:449–454, 1985.

[11] R. D. Vale, B. J. Schnapp, T. S. Reese, and M. P. Sheetz. Organelle, bead, and microtubule translocations promoted by soluble factors from the squid giant axon. *Cell*, 40:559–569, 1985.

[12] B. Grafstein and D. S. Forman. Intracellular transport in neurons. *Physiol. Rev.*, 60:1167–1283, 1980.

[13] B. R. Lasek. Axoplasmic transport in cat dorsal root ganglion cells as studied with 3H-leucine. *Brian Res.*, 7:360–377, 1968.

[14] R. D. Vale, T. S. Reese, and M. P. Sheetz. Identification of a novel force-generating protein, kinesin, involved in microtubule-based motility. *Cell*, 42:39–50, 1985.

[15] R. J. Lasek and S. T. Brady. Adenlyl imidodiphosphate (AMP-PNP) a non-hydrolyzable analog of ATP produces a stable intermediate in the motility cycle of fast axonal transport. *Biol. Bull.*, 167:503, 1984.

[16] S. T. Brady. A novel brain ATPase with properties expected for the fast axonal transport motor. *Nature*, 317:73–75, 1985.

[17] J. M. Scholey, M. E. Porter, P. M. Grissom, and J. R. Mcintosh. Identification of kinesin in sea urchin eggs, and evidence for its localization in the mitotic spindle. *Nature*, 318:483–486, 1985.

[18] S. A. Kuznetsov and V. I. Gelfand. Bovine brain kinesin is a microtubule-activated ATPase. *Proc. Natl. Acad. Sci. U. S. A.*, 83:8530–8534, 1986.

[19] D. D. Hackney. Kinesin ATPase: rate-limiting ADP release. *Proc. Natl. Acad. Sci. U. S. A.*, 85:6314–6318, 1988.

[20] J. M. Scholey, J. Heuser, J. T. Yang, and L. S. B. Goldstein. Identification of globular mechanochemical heads of kinesin. *Nature*, 338:355–357, 1989.

[21] N. Hirokawa, K. K. Pfister, H. Yorifuji, M. C. Wagner, S. T. Brady, and G. S. Bloom. Submolecular domains of bovine brain kinesin identified by electron microscopy and monoclonal antibody decoration. *Cell*, 56:867–878, 1989.

[22] A. Ashkin, K. Schutze, J. M. Dziedzic, U. Euteneuer, and M. Schliwa. Force generation of organelle transport measured *in vivo* by an infrared laser trap. *Nature*, 348:346–348, 1990.

[23] S. M. Block, L. S. B. Goldstein, and B. J. Schnapp. Bead movement by single kinesin molecules studied with optical tweezers. *Nature*, 348:348–352, 1990.

[24] S. Ray, E. Meyhofer, R. A. Milligan, and J. Howard. Kinesin follows the microtubules protofilament axis. 121:1083–1093, 1993.

[25] K. Svoboda, C. F. Schmidt, B. J. Schnapp, and S. M. Block. Direct observation of kinesin stepping by optical trapping interferometry. *Nature*, 365:721–727, 1993.

[26] K. Visscher, M. J. Schnitzer, and S. M. Block. Single kinesin molecules studied with a molecular force clamp. *Nature*, 400:184–189, 1999.

[27] K. Svoboda and S. M. Block. Force and velocity measured for single kinesin molecules. *Cell*, 77:773–784, 1994.

[28] D. D. Hackney. Evidence for alternating head catalysis by kinesin during microtubule-stimulated ATP hydrolysis. *Proc. Natl. Acad. Sci. U. S. A.*, 91:6865–6869, 1994.

[29] F. J. Kull, E. P. Sablin, R. Lau, R. J. Fletterick, and R. D. Vale. Crystal structure of the kinesin motor domain reveals a structural similarity to myosin. *Nature*, 380:550–555, 1996.

[30] Y. Okada and N. Hirokawa. A processive single-headed motor: Kinesin superfamily protein KIF1A. *Science*, 283:1152–1157, 1999.

[31] R. D. Astumian. Thermodynamics and kinetics of a Brownian motor. *Science*, 276:917–922, 1997.

[32] F. Julicher, A. Ajdari, and J. Prost. Modeling molecular motors. *Rev. Mod. Phys.*, 69:1269–1281, 1997.

[33] I. Rayment, W. R. Rypniewski, K. Schmidtbase, R. Smith, D. R. Tomchick, M. M. Benning, D. A. Winkelmann, G. Wesenberg, and H. M. Holden. Three-dimensional structure of myosin subfragment-1: a molecular motor. *Science*, 261:50–58, 1993.

[34] R. Dominguez, Y. Freyzon, K. M. Trybus, and C. Cohen. Crystal structure of a vertebrate smooth muscle myosin motor domain and its complex with the essential light chain: Visualization of the pre-power stroke state. *Cell*, 94:559–571, 1998.

[35] S. Rice, A. W. Lin, D. Safer, C. L. Hart, N. Naber, B. O. Carragher, S. M. Cain, E. Pechatnikova, E. M. Wilson-Kubalek, M. Whittaker, E. Pate, R. Cooke, E. W. Taylor, R. A. Milligan, and R. D. Vale. A structural change in the kinesin motor protein that drives motility. *Nature*, 402:778–784, 1999.

[36] Z. Zhang and D. Thirumalai. Dissecting the Kinematics of the Kinesin Step. *Structure*, 20:628–640, 2012.

[37] M. Tomishige, N. Stuurman, and R. D. Vale. Single-molecule observations of neck linker conformational changes in the kinesin motor protein. *Nat. Struct. Mol. Biol.*, 13:887–894, 2006.

[38] S. S. Rosenfeld, G. M. Jefferson, and P. H. King. ATP reorients the neck linker of kinesin in two sequential steps. *J. Biol. Chem.*, 276:40167–40174, 2001.

[39] G. Skiniotis, T. Surrey, S. Altmann, H. Gross, Y. H. Song, E. Mandelkow, and A. Hoenger. Nucleotide-induced conformations in the neck region of dimeric kinesin. *EMBO J.*, 22:1518–1528, 2003.

[40] A. B. Asenjo, Y. Weinberg, and H. Sosa. Nucleotide binding and hydrolysis induces a disorder-order transition in the kinesin neck-linker region. *Nat. Struct. Mol. Biol.*, 13:648–654, 2006.

[41] W. Hwang, M. J. Lang, and M. Karplus. Force generation in kinesin hinges on cover-neck bundle formation. *Structure*, 16:62–71, 2008.

[42] A. S. Khalil, D. C. Appleyard, A. K. Labno, A. Georges, M. Karplus, A. M. Belcher, W. Hwang, and M. J. Lang. Kinesin's cover-neck bundle folds forward to generate force. *Proc. Nat. Acad. Sci. USA*, 105:19247–19252, 2008.

[43] A. Yildiz, M. Tomishige, R. D. Vale, and P. R. Selvin. Kinesin walks hand-over-hand. *Science*, 303:676–678, 2004.

[44] M. E. Fisher and A. B. Kolomeisky. The force exerted by a molecular motor. *Proc. Natl. Acad. Sci. U. S. A.*, 96:6597–6602, 1999.

[45] M. E. Fisher and A. B. Kolomeisky. Simple mechanochemistry describes the dynamics of kinesin molecules. *Proc. Natl. Acad. Sci. U. S. A.*, 98:7748–7753, 2001.

[46] A. B. Kolomeisky and M. E. Fisher. A simple kinetic model describes the processivity of myosin-V. *Biophys. J.*, 84:1642–1650, 2003.

[47] M. E. Fisher and Y. C. Kim. Kinesin crouches to sprint but resists pushing. *Proc. Natl. Acad. Sci. U. S. A.*, 102:16209–16214, 2005.

[48] D. Tsygankov and M. E. Fisher. Mechanoenzymes under superstall and large assisting loads reveal structural features. *Proc. Natl. Acad. Sci. U. S. A.*, 104:19321–19326, 2007.

[49] A. B. Kolomeisky and M. E. Fisher. Molecular motors: A theorist's perspective. *Annu. Rev. Phys. Chem.*, 58:675–695, 2007.

[50] P. Reimann. Brownian motors: noisy transport far from equilibrium. *Phys. Rep.-Rev. Sec. Phys. Lett.*, 361:57–265, 2002.

[51] J. Howard. Mechanics of motor proteins and the cytoskeleton. *Sinauer Assoc., Sunderland, MA, 2001.*

[52] S. Leibler and D. A. Huse. Porters versus rowers: a unified stochastic model of motor proteins. *J. Cell Biol.*, 121:1357–1368, 1993.

[53] C. S. Peskin and G. Oster. Coordinated hydrolysis explains the mechanical behavior of kinesin. *Biophys. J.*, 68:S202–S211, 1995. 7th Biophysical discussions on molecular motors - structure, mechanics and energy transduction, Airlie, VA, Oct 21-23, 1994.

[54] H. Y. Wang, T. Elston, A. Mogilner, and G. Oster. Force generation in RNA polymerase. *Biophys. J.*, 74:1186–1202, 1998.

[55] R. Lipowsky. Universal aspects of the chemomechanical coupling for molecular motors. *Phys. Rev. Lett.*, 85:4401–4404, 2000.

[56] C. Bustamante, D. Keller, and G. Oster. The physics of molecular motors. *Accounts Chem. Res.*, 34:412–420, 2001.

[57] A. Mogilner, A. J. Fisher, and R. J. Baskin. Structural changes in the neck linker of kinesin explain the load dependence of the motor's mechanical cycle. *J. Theor. Biol.*, 211:143–157, 2001.

[58] H. Qian. Cycle kinetics, steady state thermodynamics and motors: a paradigm for living matter physics. *J. Phys.-Condes. Matter*, 17:S3783–S3794, 2005.

[59] J. H. Xing, H. Y. Wang, and G. Oster. From continuum Fokker-Planck models to discrete kinetic models. *Biophys. J.*, 89:1551–1563, 2005.

[60] G. H. Lan and S. X. Sun. Dynamics of myosin-V processivity. *Biophys. J.*, 88:999–1008, 2005.

[61] S. Klumpp and R. Lipowsky. Cooperative cargo transport by several molecular motors. *Proc. Natl. Acad. Sci. U. S. A.*, 102:17284–17289, 2005.

[62] K. Svoboda, P. P. Mitra, and S. M. Block. Fluctuation analysis of motor protein movement and single enzyme kinetics. *Proc. Natl. Acad. Sci. U. S. A.*, 91:11782–11786, 1994.

[63] H. Kojima, E. Muto, H. Higuchi, and T. Yanagida. Mechanics of single kinesin molecules measured by optical trapping nanometry. *Biophys. J.*, 73:2012–2022, 1997.

[64] H. Higuchi, E. Muto, Y. Inoue, and T. Yanagida. Kinetics of force generation by single kinesin molecules activated by laser photolysis of caged ATP. *Proc. Natl. Acad. Sci. U. S. A.*, 94:4395–4400, 1997.

[65] A. N. Fehr, B. Gutierrez-Medina, C. L. Asbury, and S. M. Block. On the Origin of Kinesin Limping. *Biophys. J.*, 97:1663–1670, 2009.

[66] C. L. Asbury, A. N. Fehr, and S. M. Block. Kinesin moves by an asymmetric hand-over-hand mechanism. *Science*, 302:2130–2134, 2003.

[67] G. T. Shubeita, S. L. Tran, J. Xu, M. Vershinin, S. Cermelli, S. L. Cotton, M. A. Welte, and S. P. Gross. Consequences of Motor Copy Number on the Intracellular Transport of Kinesin-1-Driven Lipid Droplets. *Cell*, 135:1098–1107, 2008.

[68] S. M. Block. Kinesin motor mechanics: Binding, stepping, tracking, gating, and limping. *Biophys. J.*, 92:2986–2995, 2007.

[69] S. Uemura and S. Ishiwata. Loading direction regulates the affinity of ADP for kinesin. *Nat. Struct. Biol.*, 10:308–311, 2003.

[70] N. R. Guydosh and S. M. Block. Backsteps induced by nucleotide analogs suggest the front head of kinesin is gated by strain. *Proc. Natl. Acad. Sci. U. S. A.*, 103:8054–8059, 2006.

[71] H. B. Song and S. A. Endow. Decoupling of nucleotide- and microtubule-binding sites in a kinesin mutant. *Nature*, 396:587–590, 1998.

[72] R. D. Vale. The molecular motor toolbox for intracellular transport. *Cell*, 112:467–480, 2003.

[73] N. Hirokawa, Y. Noda, Y. Tanaka, and S. Niwa. Kinesin superfamily motor proteins and intracellular transport. *Nat. Rev. Mol. Cell Biol.*, 10:682–696, 2009.

[74] W. Hua, J. Chung, and J. Gelles. Distinguishing inchworm and hand-over-hand processive kinesin movement by neck rotation measurements. *Science*, 295:844–848, 2002.

[75] F. Kozielski, S. Sack, A. Marx, M. Thormahlen, E. Schonbrunn, V. Biou, A. Thompson, E. M. Mandelkow, and E. Mandelkow. The crystal structure of dimeric kinesin and implications for microtubule-dependent motility. *Cell*, 91:985–994, 1997.

[76] R. D. Vale and R. A. Milligan. The way things move: Looking under the hood of molecular motor proteins. *Science*, 288:88–95, 2000.

[77] J. A. Spudich and S. Sivaramakrishnan. Myosin VI: an innovative motor that challenged the swinging lever arm hypothesis. *Nat. Rev. Mol. Cell Biol.*, 11:128–137, 2010.

[78] A. Gennerich and R. D. Vale. Walking the walk: how kinesin and dynein coordinate their steps. *Curr. Opin. Cell Biol.*, 21(1):59–67, 2009.

[79] W. R. Schief and J. Howard. Conformational changes during kinesin motility. *Curr. Opin. Cell Biol.*, 13(1):19–28, 2001.

[80] N. J. Carter and R. A. Cross. Kinesin's moonwalk. *Curr. Opin. Cell Biol.*, 18(1):61–67, 2006.

[81] N. J. Carter and R. A. Cross. Mechanics of the kinesin step. *Nature*, 435:308–312, 2005.

[82] A. Yildiz, M. Tomishige, A. Gennerich, and R. D. Vale. Intramolecular strain coordinates kinesin stepping behavior along microtubules. *Cell*, 134:1030–1041, 2008.

[83] S. M. Block, C. L. Asbury, J. W. Shaevitz, and M. J. Lang. Probing the kinesin reaction cycle with a 2D optical force clamp. *Proc. Natl. Acad. Sci. U. S. A.*, 100:2351–2356, 2003.

[84] M. Tomishige and R. D. Vale. Controlling kinesin by reversible disulfide cross-linking: Identifying the motility-producing conformational change. *J. Cell Biol.*, 151:1081–1092, 2000.

[85] B. E. Clancy, W. M. Behnke-Parks, J. O. L. Andreasson, S. S. Rosenfeld, and S. M. Block. A universal pathway for kinesin stepping. *Nat. Struct. Mol. Biol.*, 18:1020–1027, 2011.

[86] D. D. Hackney. The tethered motor domain of a kinesin-microtubule complex catalyzes reversible synthesis of bound ATP. *Proc. Natl. Acad. Sci. USA*, 102:18338–18343, 2005.

[87] S. Rice, Y. Cui, C. Sindelar, N. Naber, M. Matuska, R. D. Vale, and R. Cooke. Thermodynamic properties of the kinesin neck-region docking to the catalytic core. *Biophys. J.*, 84:1844–1854, 2003.

[88] C. V. Sindelar and K. H. Downing. The beginning of kinesin's force-generating cycle visualized at 9-A resolution. *J. Cell Biol.*, 177:377–385, 2007.

[89] C. Hyeon and J. N. Onuchic. Mechanical control of the directional stepping dynamics of the kinesin motor. *Proc. Natl. Acad. Sci. U. S. A.*, 104(44):17382–17387, 2007.

[90] J. G. de la Torre, M. L. Huertas, and B. Carrasco. Calculation of hydrodynamic properties of globular proteins from their atomic-level structure. *Biophys. J.*, 78(2):719–730, 2000.

[91] R. Nitta, M. Kikkawa, Y. Okada, and N. Hirokawa. KIF1A alternately uses two loops to bind microtubules. *Science*, 305:678–683, 2004.

[92] R. Nitta, Y. Okada, and N. Hirokawa. Structural model for strain-dependent microtubule activation of Mg-ADP release from kinesin. *Nat. Struct. Mol. Biol.*, 15:1067–1075, 2008.

[93] S. Uchimura, Y. Oguchi, M. Katsuki, T. Usui, H. Osada, J. Nikawa, S. Ishiwata, and E. Muto. Identification of a strong binding site for kinesin on the microtubule using mutant analysis of tubulin. *Embo J.*, 25(24):5932–5941, 2006.

[94] R. Elber and A. West. Atomically detailed simulation of the recovery stroke in myosin by Milestoning. *Proc. Natl. Acad. Sci. U. S. A.*, 107:5001–5005, 2010.

[95] R. Elber. Simulations of allosteric transitions. *Curr. Opin. Struct. Biol.*, 21:167–172, 2011.

[96] M. Mickler, R. I. Dima, H. Dietz, C. Hyeon, D. Thirumalai, and M. Rief. Revealing the bifurcation in the unfolding pathways of GFP by using single-molecule experiments and simulations. *Proc. Natl. Acad. Sci. USA*, 104:20268–20273, 2007.

[97] C. Hyeon and D. Thirumalai. Mechanical unfolding of RNA: From hairpins to structures with internal multiloops. *Biophys. J.*, 92:731–743, 2007.

[98] C. Hyeon, G. H. Lorimer, and D. Thirumalai. Dynamics of allosteric transitions in GroEL. *Proc. Natl. Acad. Sci. USA*, 103:18939–18944, 2006.

[99] R. Tehver and D. Thirumalai. Rigor to Post-Rigor Transition in Myosin V: Link between the Dynamics and the Supporting Architecture. *Structure*, 18:471–481, 2010.

[100] R. I. Dima and H. Joshi. Probing the origin of tubulin rigidity with molecular simulations. *Proc. Natl. Acad. Sci. U. S. A.*, 105:15743–15748, 2008.

[101] H. Joshi, F. Momin, K. E. Haines, and R. I. Dima. Exploring the contribution of collective motions to the dynamics of forced-unfolding in tubulin. *Biophys. J.*, 98:657–666, 2010.

[102] C. Hyeon and J. N. Onuchic. Internal strain regulates the nucleotide binding site of the kinesin leading head. *Proc. Natl. Acad. Sci. U. S. A.*, 104(7):2175–2180, 2007.

[103] T. Veitshans, D. Klimov, and D. Thirumalai. Protein folding kinetics: Timescales, pathways and energy landscapes in terms of sequence-dependent properties. *Fold. Des.*, 2:1–22, 1997.

[104] Y. Taniguchi, M. Nishiyama, Y. Ishii, and T. Yanagida. Entropy rectifies the Brownian steps of kinesin. *Nat. Chem. Biol.*, 1:342–347, 2005.

[105] G. Woehlke, A. K. Ruby, C. L. Hart, B. Ly, N. HomBooher, and R. D. Vale. Microtubule interaction site of the kinesin motor. *Cell*, 90(2):207–216, 1997.

[106] S. P. Gilbert, M. R. Webb, M. Brune, and K. A. Johnson. Pathway of processive ATP hydrolysis by kinesin. *Nature*, 373:671–676, 1995.

[107] M. J. Schnitzer and S. M. Block. Kinesin hydrolyses one ATP per 8-nm step. *Nature*, 388:386–390, 1997.

[108] A. Gennerich, A. P. Carter, S. L. Reck-Peterson, and R. D. Vale. Force-induced bidirectional stepping of cytoplasmic dynein. *Cell*, 131:952–965, 2007.

[109] S. L. Reck-Peterson, A. Yildiz, A. P. Carter, A. Gennerich, N. Zhang, and R. D. Vale. Single-molecule analysis of dynein processivity and stepping behavior. *Cell*, 126:335–348, 2006.

[110] V. Hariharan and W. O. Hancock. Insights into the Mechanical Properties of the Kinesin Neck Linker Domain from Sequence Analysis and Molecular Dynamics Simulations. *Cell. Mol. Bioeng.*, 2:177–189, 2009.

[111] B. J. Grant, D. M. Gheorghe, W. Zheng, M. Alonso, G. Huber, M. Dlugosz, J. A. McCammon, and R. A. Cross. Electrostatically Biased Binding of Kinesin to Microtubules. *PLoS. Biol.*, 9, 2011.

[112] S. Uemura, K. Kawaguchi, J. Yajima, M. Edamatsu, Y. Y. Toyoshima, and S. Ishiwata. Kinesin-microtubule binding depends on both nucleotide state and loading direction. *Proc. Natl. Acad. Sci. USA*, 99:5977–5981, 2002.

[113] T. J. Purcell, C. Morris, J. A. Spudich, and H. L. Sweeney. Role of the lever arm in the processive stepping of myosin V. *Proc. Natl. Acad. Sci. U. S. A.*, 99:14159–14164, 2002.

[114] C. Hyeon and D. Thirumalai. Capturing the essence of folding and functions of biomolecules using coarse-grained models. *Nat. Comm.*, 2:487, 2011.

[115] C. Hyeon, R. I. Dima, and D. Thirumalai. Pathways and kinetic barriers in mechanical unfolding and refolding of RNA and proteins. *Structure*, 14:1633–1645, 2006.

[116] J. Chen, R. I. Dima, and D. Thirumalai. Allosteric communication in dihydrofolate reductase: Signaling network and pathways for closed to occluded transition and back. *J. Mol. Boil.*, 374:250–266, 2007.

[117] A. M. Mastro, M. A. Babich, W. D. Taylor, and A. D. Keith. Diffusion of a small molecule in the cytoplasm of mammalian-cells. *Proc. Natl. Acad. Sci. U. S. A.*, 81(11):3414–3418, 1984.

[118] T. Mori, R. D. Vale, and M. Tomishige. How kinesin waits between steps. *Nature*, 450:750–U15, 2007.

[119] A. B. Asenjo and H. Sosa. A mobile kinesin-head intermediate during the ATP-waiting state. *Proc. Natl. Acad. Sci. U. S. A.*, 106:5657–5662, 2009.

[120] D. D. Hackney, M. F. Stock, J. Moore, and R. A. Patterson. Modulation of kinesin half-site ADP release and kinetic processivity by a spacer between the head groups. *Biochemistry*, 42:12011–12018, 2003.

[121] W. Hua, E. C. Young, M. L. Fleming, and J. Gelles. Coupling of kinesin steps to ATP hydrolysis. *Nature*, 388:390–393, 1997.

[122] C. V. Sindelar and K. H. Downing. An atomic-level mechanism for activation of the kinesin molecular motors. *Proc. Natl. Acad. Sci. USA*, 107:4111–4116, 2010.

[123] J. L. Bos, H. Rehmann, and A. Wittinghofer. GEFs and GAPs: Critical elements in the control of small G proteins. *Cell*, 129:865–877, 2007.

[124] H. L. Sweeney and A. Houdusse. Myosin VI rewrites the rules for myosin motors. *Cell*, 141:573–582, 2010.

[125] J. P. Grason, J. S. Gresham, and G. H. Lorime. Setting the chaperonin timer: A two-stroke, two-speed, protein machine. *Proc. Natl. Acad. Sci. U. S. A.*, 105:17339–17344, 2008.

[126] N. Naber, T. J. Minehardt, S. Rice, X. R. Chen, J. Grammer, M. Matuska, R. D. Vale, P. A. Kollman, R. Car, R. G. Yount, R. Cooke, and E. Pate. Closing of the nucleotide pocket of kinesin-family motors upon binding to microtubules. *Science*, 300:798–801, 2003.

[127] M. Y. Yun, X. H. Zhang, C. G. Park, H. W. Park, and S. A. Endow. A structural pathway for activation of the kinesin motor ATPase. *Embo J.*, 20(11):2611–2618, JUN 1 2001.

[128] D. E. Shaw, M. M. Deneroff, R. O. Dror, J. S. Kuskin, R. H. Larson, J. K. Salmon, C. Young, B. Batson, K. J. Bowers, J. C. Chao, M. P. Eastwood, J. Gagliardo, J. P. Grossman, C. R. Ho, D. J. Ierardi, I. Kolossvary, J. L. Klepeis, T. Layman, C. Mcleavey, M. A. Moraes, R. Mueller, E. C. Priest, Y. Shan, J. Spengler, M. Theobald, B. Towles, and S. C. Wang. Anton, a special-purpose machine for molecular dynamics simulation. *Commun. ACM*, 51:91–97, 2008.

[129] Y. Shan, M. P. Eastwood, X. Zhang, E. T. Kim, A. Arkhipov, R. O. Dror, J. Jumper, J. Kuriyan, and D. E. Shaw. Oncogenic Mutations Counteract Intrinsic Disorder in the EGFR Kinase and Promote Receptor Dimerization. *Cell*, 149:860–870, 2012.

[130] A. C. Kruse, J. Hu, A. C. Pan, D. H. Arlow, D. M. Rosenbaum, E. Rosemond, H. F. Green, T. Liu, P. S. Chae, R. O. Dror, D. E. Shaw, W. I. Weis, J. Wess, and B. K. Kobilka. Structure and dynamics of the M3 muscarinic acetylcholine receptor. *Nature*, 482:552–556, 2012.

[131] M. O. Jensen, V. Jogini, D. W. Borhani, A. E. Leffler, R. O. Dror, and D. E. Shaw. Mechanism of Voltage Gating in Potassium Channels. *Science*, 336:229–233, 2012.

[132] S. Sack, J. Muller, A. Marx, M. Thormahlen, E. M. Mandelkow, S. T. Brady, and E. Mandelkow. X-ray structure of motor and neck domains from rat brain kinesin. *Biochemistry*, 36:16155–16165, 1997.

[133] A. P. Carter, C. Cho, L. Jin, and R. D. Vale. Crystal Structure of the Dynein Motor Domain. *Science*, 331:1159–1165, 2011.

[134] T. Kon, K. Sutoh, and G. Kurisu. X-ray structure of a functional full-length dynein motor domain. *Nat. Struct. Mol. Biol.*, 18:638–U26, 2011.

[135] A. Feklistov and S. A. Darst. Structural Basis for Promoter-10 Element Recognition by the Bacterial RNA Polymerase sigma Subunit. *Cell*, 147:1257–1269, 2011.

[136] J. Chen, S. A. Darst, and D. Thirumalai. Promoter melting triggered by bacterial RNA polymerase occurs in three steps. *Proc. Natl. Acad. Sci. U. S. A.*, 107:12523–12528, 2010.

[137] A. Gennerich and R. D. Vale. Walking the walk: how kinesin and dynein coordinate their steps. *Curr. Opin. Cell Biol.*, 21:59–67, 2009.

[138] H. L. Li, D. J. DeRosier, W. V. Nicholson, E. Nogales, and K. H. Downing. Microtubule structure at 8 angstrom Resolution. *Structure*, 10:1317–1328, 2002.

[139] Y. Miyazono, M. Hayashi, P. Karagiannis, Y. Harada, and H. Tadakuma. Strain through the neck linker ensures processive runs: a DNA-kinesin hybrid nanomachine study. *EMBO J.*, 29:93–106, 2010.

[140] P. Burkhard, R. A. Kammerer, M. O. Steinmetz, G. P. Bourenkov, and U. Aebi. The coiled-coil trigger site of the rod domain of cortexillin I unveils a distinct network of interhelical and intrahelical salt bridges. *Structure*, 8:223–230, 2000.

[141] T. H. Creighton. Proteins: structures and molecular properties. *W. H. Freeman, San Francisco, CA, 1993*.

[142] B. Gutierrez-Medina, A. N. Fehr, and S. M. Block. Direct measurements of kinesin torsional properties reveal flexible domains and occasional stalk reversals during stepping. *Proc. Natl. Acad. Sci. USA*, 106:17007–17012, 2009.

[143] D. L. Ermark and J. A. McCammon. Brownian dynamics with hydrodynamic interactions. *J. Chem. Phys.*, 69:1352–1360, 1978.

[144] J. Rotne and S. Prager. Variational treatment of hydrodynamic interaction in polymers. *J. Chem. Phys.*, 50:4831–&, 1969.

[145] H. Yamakawa. Transport properties of polymer chains in dilute solution: hydrodynamic interaction. *J. Chem. Phys.*, 53:436–&, 1970.

[146] T. Frembgen-Kesner and A. H. Elcock. Striking Effects of Hydrodynamic Interactions on the Simulated Diffusion and Folding of Proteins. *J. Chem. Theory Comput.*, 5:242–256, 2009.

[147] B. R. Brooks, R. E. Bruccoler, B. D. Olafson, D. J. States, S. Swaminathan, and M. Karplus. CHARMM - A program for macromolecular energy, minimization, and dynamics calculations. *J. Comput. Chem.*, 4:187–217, 1983.

[148] B. R. Brooks, C. L. Brooks, III, A. D. Mackerell, Jr., L. Nilsson, R. J. Petrella, B. Roux, Y. Won, G. Archontis, C. Bartels, S. Boresch, A. Caflisch, L. Caves, Q. Cui, A. R. Dinner, M. Feig, S. Fischer, J. Gao, M. Hodoscek, W. Im, K. Kuczera, T. Lazaridis, J. Ma, V. Ovchinnikov, E. Paci, R. W. Pastor, C. B. Post, J. Z. Pu, M. Schaefer, B. Tidor, R. M. Venable, H. L. Woodcock,

X. Wu, W. Yang, D. M. York, and M. Karplus. CHARMM: The biomolecular simulation program. *J. Comput. Chem.*, 30:1545–1614, 2009.

[149] J. C. Phillips, R. Braun, W. Wang, J. Gumbart, E. Tajkhorshid, E. Villa, C. Chipot, R. D. Skeel, L. Kale, and K. Schulten. Scalable molecular dynamics with NAMD. *J. Comput. Chem.*, 26:1781–1802, 2005.